

***IN VIVO* HUMAN RIGHT VENTRICLE SHAPE
AND KINEMATIC ANALYSIS WITH AND
WITHOUT PULMONARY HYPERTENSION**

by

Jia Wu

BS in Materials Science and Engineering, Harbin Institute of
Technology, China, 2007

MS in Materials Science and Engineering, Harbin Institute of
Technology, China, 2009

Submitted to the Graduate Faculty of
the Swanson School of Engineering in partial fulfillment
of the requirements for the degree of
Doctor of Philosophy

University of Pittsburgh

2013

UNIVERSITY OF PITTSBURGH
SWANSON SCHOOL OF ENGINEERING

This dissertation was presented

by

Jia Wu

It was defended on

May 24th, 2013

and approved by

John C. Brigham, PhD, Assistant Professor, Department of Civil and Environmental
Engineering and Bioengineering

Jeen-Shang Lin, ScD, Associate Professor, Department of Civil and Environmental
Engineering

Vikas Khanna, PhD, Assistant Professor, Department of Civil and Environmental
Engineering

Marc A. Simon, MD, Assistant Professor, School of Medicine and Bioengineering

Yongjie (Jessica) Zhang, PhD, Associate Professor, Department of Mechanical Engineering
and Biomedical Engineering, Carnegie Mellon University

Dissertation Director: John C. Brigham, PhD, Assistant Professor, Department of Civil
and Environmental Engineering and Bioengineering

Copyright © by Jia Wu
2013

***IN VIVO* HUMAN RIGHT VENTRICLE SHAPE AND KINEMATIC ANALYSIS WITH AND WITHOUT PULMONARY HYPERTENSION**

Jia Wu, PhD

University of Pittsburgh, 2013

Pulmonary hypertension (PH) is a severe cardio-pulmonary illness which has been commonly observed to induce substantial and ultimately deleterious changes to the human right ventricle (RV) shape and function. As such, the functional state of the RV is thought to be a major determinant of symptoms and survival rates for PH. However, there has been little success to-date to identify clinically obtainable metrics of RV shape and deformation as a means to detect the onset and progression of PH. This difficulty is largely the result of the absence of a proven approach that is generally applicable for consistent and reliable quantitative analysis of anatomical shapes, particularly the RV, between patients and over time. Therefore, a computational framework which can quantitatively analyze RV shape and deformation could be a key to assist in clinically detecting the onset and progression of PH.

Statistical shape analysis techniques were developed, implemented, and assessed to analyze variations in human RV endocardial surface (RVES) shapes and kinematics from non-invasive clinical medical imaging data with respect to a spectrum of hemodynamic states. A computational framework for the quantitative analysis and statistical decomposition of sets of 3D genus-0 shapes that combines a modified harmonic mapping approach directly with proper orthogonal decomposition (DM-POD) is presented. The DM-POD approach is shown to be a robust technique for recovering inherent shape-related features through the analysis of sets of artificially generated shapes. The DM-POD approach is then applied to obtain kinematic features of the human RV based on the relative change in shape of the endocardial surface using cardiac computed tomography images. In addition, the kinematic features of

the RVES obtained by the DM-POD approach are shown to be consistent and associated with intrinsically physiological components of the heart, and thus may potentially provide a more accurate means for classifying the progressive change in RV function caused by PH, in comparison to traditional clinical hemodynamic and volume-based metrics. Statistical shape analysis for the human RV is further evaluated through analysis of alternate components of the DM-POD approach, as well as through comparison of the DM-POD workflow with an alternate spherical harmonic function-based workflow (SPHARM), with respect to the aspects of surface representation, alignment, and decomposition. Additionally, different ways of utilizing the available imaging data with respect to the classification potential are investigated by considering analysis results when applying both the various DM-POD and SPHARM approaches with several different combinations of the phases captured throughout a single cardiac cycle for the patient set. Lastly, a novel statistical decomposition technique known as independent component analysis (ICA) was incorporated into the statistical shape analysis framework (i.e., DM-POD) to produce an alternative workflow (DM-ICA). Both the DM-POD and DM-ICA approaches are applied to analyze sets of artificially generated data and the human RVES datasets, and the respective results are compared. The DM-POD and DM-ICA workflows are shown to produce consistent, but substantially different results due to the various principles and views of each of the two statistical decomposition algorithms (i.e., POD and ICA). Most importantly, the results from the DM-POD and DM-ICA workflows appear to relate to RV function in unique ways, with respect to both traditional clinical metrics and each other, and have the potential to provide new metrics for better understanding of the human RV and its relationship to PH.

TABLE OF CONTENTS

PREFACE	xix
1.0 A NEW COMPUTATIONAL FRAMEWORK FOR ANATOMICALLY CONSISTENT 3D STATISTICAL SHAPE ANALYSIS WITH CLIN- ICAL IMAGING APPLICATIONS	1
1.1 Abstract	1
1.2 Introduction	1
1.3 Methods	4
1.3.1 Surface Parameterization	4
1.3.1.1 Initial Parameterization	6
1.3.1.2 Secondary Parameterization	7
1.3.2 Shape Mode Decomposition	10
1.4 Examples and Discussion	12
1.4.1 Human Right Ventricle Endocardial Surface	12
1.4.1.1 Mesh Sensitivity/Convergence:	13
1.4.1.2 Sensitivity to Anatomical References:	19
1.4.1.3 Sensitivity to Reference Point Perturbations:	21
1.4.2 Artificially Generated Shapes	22
1.4.2.1 Results and Discussion:	28
1.5 Conclusions	31
2.0 A NEW APPROACH TO KINEMATIC FEATURE EXTRACTION FROM THE HUMAN RIGHT VENTRICLE FOR CLASSIFICATION OF HYPERTENSION: A FEASIBILITY STUDY	33

2.1	Abstract	33
2.2	Introduction	34
2.3	Human Cardiac Image Dataset	36
2.4	Methods	38
	2.4.1 Segmentation and Mesh Generation	38
	2.4.2 Surface Parameterization	40
	2.4.3 Pseudo-Displacement Functions	44
	2.4.4 Pseudo-Displacement Decomposition	45
2.5	Results and Discussion	46
	2.5.1 Feature Convergence	49
	2.5.2 Relationship to Pulmonary Hypertension/Classification Potential	54
	2.5.3 Preprocessing Expense	59
2.6	Conclusions	61
3.0	A COMPARATIVE ANALYSIS OF GLOBAL SHAPE ANALYSIS	
	METHODS FOR THE ASSESSMENT OF RIGHT VENTRICULAR	
	FUNCTION	62
3.1	Abstract	62
3.2	Introduction	63
	3.2.1 Clinical Motivation	63
	3.2.2 Technical Background	63
	3.2.3 Aim of Study	67
3.3	Methods	68
	3.3.1 Image Acquisition and Surface Extraction	70
	3.3.2 Surface Parameterization	71
	3.3.2.1 DM-POD Approach:	71
	3.3.2.2 SPHARM Approach:	72
	3.3.3 Surface Alignment	73
	3.3.3.1 Pseudo-Displacement:	74
	3.3.3.2 Iterative Closest Point:	74
	3.3.3.3 First-Order Ellipsoid:	75

3.3.3.4 Registration of SPHARM Parameterization:	76
3.3.4 Statistical Decomposition	77
3.4 Results and Discussion	78
3.4.1 Human Cardiac Image Dataset and Clinical Classification	78
3.4.2 Mapping and Alignment	81
3.4.3 Statistical Decomposition	85
3.4.4 Clustering	88
3.5 Conclusions	94
4.0 AN IMPLEMENTATION OF INDEPENDENT COMPONENT ANALYSIS FOR 3D STATISTICAL SHAPE ANALYSIS	96
4.1 Abstract	96
4.2 Introduction	97
4.3 ICA Methods	99
4.3.1 ICA Algorithm	100
4.3.1.1 Centering and Whitening:	101
4.3.1.2 Maximization of Non-Gaussianity:	102
4.4 Results and Discussion	104
4.4.1 Decomposition of Artificially Generated Surfaces	105
4.4.2 Decomposition of Human Right Ventricle Endocardial Surfaces	109
4.4.2.1 Statistical Shape Analysis Framework:	109
4.4.2.2 Clinical Cardiac Dataset:	111
4.4.2.3 Right Ventricle Endocardial Surface Decomposition Results:	112
4.5 Conclusions	119
5.0 CURRENT CAPABILITIES AND FUTURE DIRECTIONS	120
APPENDIX A. INDEPENDENT COMPONENT ANALYSIS - DERIVATION OF NON-GAUSSIANITY MAXIMIZATION	122
APPENDIX B. INDEPENDENT COMPONENT ANALYSIS - CALCULATION OF JACOBIAN MATRIX	123
APPENDIX C. PROPER ORTHOGONAL DECOMPOSITION FOR VECTOR-VALUED FUNCTIONS	124

C.1 Objective	124
C.2 Methods	124
C.3 Method of Snapshots	126
BIBLIOGRAPHY	128

LIST OF TABLES

1.1	Mean (μ) and standard deviation (σ) of the relative mode energy percentage for training set sizes of 10, 20, and 30 shapes obtained from PCA of the spherical harmonic coefficients (Control) and obtained from POD with the proposed framework (Proposed).	30
1.2	Mean (μ) and standard deviation (σ) of the rate of classification percentage for the training and testing sets for the spherical harmonic coefficients (Control) and the modal coefficients from POD with the proposed framework (Proposed) for training set sizes of 10, 20, and 30 shapes.	32

LIST OF FIGURES

1.1	Example of (a) a 3D genus-0 shape, (b) the results of the initial parameterization, and (c) the results of the secondary parameterization.	8
1.2	Example of a RVES shape at end diastole with the free wall (FW), septal wall (SW), pulmonic valve (PV), tricuspid valve (TV), (a) Options 1 and 2, and (b) Option 3 for the potential date line segments labeled.	14
1.3	Three different mesh sizes used to test mesh size sensitivity for a representative human right ventricle at end diastole.	16
1.4	Modal decomposition and reconstruction of the RVES pseudo-displacement field over the cardiac cycle (contours represent displacement magnitude). . .	17
1.5	Relative amplitude of the modal coefficients for the first three POD modes over the cardiac cycle (from end diastole (ED) to end systole (ES) and then back to ED).	18
1.6	First three POD modes and corresponding mode energy for the RVES pseudo-displacement for the three options for the referential data.	20
1.7	(a)-(f) six representative examples of the artificially generated symmetric spherical harmonic shapes and (g)-(l) six representative examples of the artificially generated asymmetric spherical harmonic shapes.	24
1.8	Representative examples of (a) a symmetric and (b) an asymmetric shape used for the artificially generated shape test cases with the harmonic topological mapping poles and date lines labeled.	25

1.9	Schematic of the analysis procedure to assess the pattern recognition capabilities of the proposed approach. The PCA modes from the Control Test were compared to the POD modes from the Proposed Framework and the rate of classification using the spherical harmonic coefficients from the Control Test was compared to the rate of classification using the POD modal coefficients from the Proposed Framework.	27
1.10	Example of (a) mode 1, (b) mode 2, and (c) mode 3 obtained from PCA of the spherical harmonic coefficients (i.e., control test), and (d) mode 1, (e) mode 2, and (f) mode 3 obtained from POD with the proposed framework for the symmetric shape test cases.	29
2.1	Schematic of the shape analysis framework, including (a) segmentation of the RVES from the CT images, (b) smoothing and interpolated 3D closed surface mesh generation, (c) parameterization of the RVES in terms of spherical coordinates through harmonic mapping (shown in 2D), (d) conversion of all surfaces to shape change functions, and (e) decomposition of the shape change functions into the fundamental shape change features (i.e., modes) using POD.	39
2.2	Example RVES at end diastole (a) with the free wall (FW), septal wall (SW), pulmonic valve (PV), tricuspid valve (TV), apex, and harmonic mapping reference line labeled, and (b) the latitude distribution and (c) the longitude distribution after the harmonic mapping.	42
2.3	(a) The first four shape change modes from decomposition of the 10 patient set plotted on the end diastole shape (color contours are magnitude of shape change) and (b) the corresponding relative modal coefficients over the cardiac cycle for N4.	47
2.4	Relative modal coefficients for the first shape change mode for the first two non-hypertensive (N1 and N2) and hypertensive (H1 and H2) patients over the cardiac cycle.	49
2.5	Relative volume enclosed by the right ventricle endocardial surface for the first two non-hypertensive (N1 and N2) and hypertensive (H1 and H2) patients over the cardiac cycle.	50

2.6	Mode 1 for N1, Mode 2 for H2, Mode 3 for H2, and Mode 4 for N1 from the decomposition of the respective individual, respective hemodynamic class (either all N or all H), and all 10 patients included in the decomposition process (color contours are magnitude of shape change).	52
2.7	Relative modal coefficients over the cardiac cycle for (a) the highest energy mode for N1 (Mode 1 from the full 10 patient group) and (b) the highest energy mode for H2 (Mode 2 from the full group) from the decomposition of the respective individual, respective hemodynamic class (either all N or all H), and all 10 patients included in the decomposition process.	53
2.8	Total modal energy for the first three modes for the six non-hypertensive (N) and four hypertensive (H) patients considered for this study, and the results from K-means clustering the dataset into two groups: C1 and C2.	56
2.9	Relative modal contribution (percentage) for each of the 10 individuals for the modes necessary to capture over 99% of the total modal energy for each individual (bars are numbered and color-coded according to the corresponding mode number/ranking from the complete 10 patient set).	57
2.10	Hemodynamic distribution of the six non-hypertensive (N) and four hypertensive (H) patients consider for this study in terms of the mean pulmonary arterial pressure (PAP) and right atrial pressure (RAP).	58
2.11	Ejection fraction of the six non-hypertensive (N) and four hypertensive (H) patients considered for this study.	60

3.1	Schematic of the statistical shape analysis workflows, including the approach that directly applies POD to harmonically mapped surfaces (DM-POD - solid red arrows) and the approach that projects the surfaces onto spherical harmonic functions after harmonic mapping (SPHARM - dotted blue arrows), showing the key steps of (a) segmentation of the right ventricle endocardial surface (RVES) from the medical images, (b) smoothing and interpolated 3D closed surface mesh generation, (c) parameterization of the RVES in terms of spherical coordinates (shown in 2D), (d) projection of the RVES onto a spherical harmonic function basis (SPHARM), (e) alignment of the surfaces based on the spherical harmonic function parameterization (SPHARM), (f) alignment of the surfaces either by conversion into shape change functions or by a rigid registration algorithm (DM-POD), and (g) decomposition of the shape sets into modes and application of pattern recognition techniques.	69
3.2	Hemodynamic distribution of the six non-hypertensive (marked as N1 - N6 with black cross), six hypertensive with decompensated right ventricle (RV) function (marked as D1 - D6 with green cross), and one hypertensive with compensated RV function (marked as C1 with blue cross) patients considered for this study in terms of the mean pulmonary arterial pressure (PAP) and right atrial pressure (RAP).	79
3.3	Ejection fraction of the six non-hypertensive (N1 - N6), six hypertensive with decompensated right ventricle (RV) function (D1 - D6), and one hypertensive with compensated RV function (C1) patients considered for this study.	80

3.4	Initial orientation of a representative set of six segmented and smoothed right ventricle endocardial surface (RVES) shapes at the end diastole (ED) phase of the cardiac cycle, including two non-hypertensive patients (N3 & N5), three hypertensive with decompensated right ventricle (RV) function patients (D1, D5, & D6), and one hypertensive with compensated RV function patient (C1), as well as the results of the mapping to spherical coordinates (color contours) and orientations of each RVES following the two step harmonic mapping and the iterative closest point (ICP) alignment of the DM-POD workflow, and the harmonic mapping followed by the control of area and length distortions (CALD) algorithm and the first order ellipsoid (FOE) or the SHREC alignment of the SPHARM workflow. Additionally, for the SPHARM workflow the two updated alignment trials are shown (labeled with “Updated”), where the orientation of the RVES were manually adjusted according to the anatomical references and then the two SPHARM alignment algorithms in combination with the parameterization algorithm were applied again.	82
3.5	A representative set of six segmented and smoothed right ventricle endocardial surface (RVES) shapes at the end diastole (ED) phase of the cardiac cycle, including two non-hypertensive patients (N3 & N5), three hypertensive with decompensated right ventricle (RV) function patients (D1, D5, & D6), and one hypertensive with compensated RV function patient (C1), manually rotated to be anatomically consistent, and the expansion of each RVES onto a collection of spherical harmonic functions after parameterization (as used within the SPHARM workflow), for spherical harmonic function bases of degree 1 (4 basis functions), degree 5 (36 basis functions), and degree 15 (256 basis functions) (with orientation maintained consistently).	84

3.6	The mean shape and plus or minus one and two standard deviations ($\pm\sigma_i$ and $\pm 2\sigma_i$) of each of the first three modal coefficient values multiplied with the corresponding mode shape and added to the mean shape for analysis of the dataset of 13 patient’s right ventricle endocardial surface shapes at the end diastole phase in the cardiac cycle with (a) the DM-POD workflow with ICP alignment and (b) the SPHARM workflow with the “Updated” SHREC alignment.	87
3.7	The cumulative modal energy for the POD and ICA modes obtained for the 13-patient dataset from analysis of (a) the end diastole (ED) and end systole (ES) phases in the cardiac cycle alone with the DM-POD workflow with ICP alignment and the SPHARM workflow with the “Updated” SHREC alignment, (b) the ED and ES phases combined with the DM-POD workflow with the pseudo-displacement (PD) alignment (subtracting the ED phase from the ES phase), the DM-POD workflow with ICP alignment, and the SPHARM workflow with the “Updated” SHREC alignment, and (c) all available phases with the DM-POD workflow with the PD alignment (subtracting the ED phase from all other phases), the DM-POD workflow with ICP alignment, and the SPHARM workflow with the “Updated” SHREC alignment.	89
3.8	Percentage (i.e., Clustering Rate) of patients from the 13-patient dataset that were grouped by K-means clustering (assuming two classes) with the majority of patients in the same classification (hypertensive or non-hypertensive) based on the feature vector of the individual relative modal energy percentages from the DM-POD workflow analysis with ICP alignment of all available phases in the cardiac cycle, the end diastole (ED) phase alone, the end systole (ES) phase alone, and the ED and ES phases combined, the DM-POD workflow analysis with the pseudo-displacement (PD) alignment (subtracting the ED phase from all other phases) of all available phases and the ED and ES phases combined, and SPHARM workflow analysis with the “Updated” SHREC alignment of all available phases, the ED phase alone, the ES phase alone, and the ED and ES phases combined.	91

3.9	Hierarchical clustering results (relative distance between feature vectors in the set) of the 13-patient dataset, including the 6 non-hypertensive individuals (N1 - N6), the 6 hypertensive with decompensated right ventricle (RV) function individuals (D1 - D6), and the 1 hypertensive with compensated RV function individual (C1), for the (a) clinical normalized pressure-volume feature vector, (b) individual relative modal energy percentage feature vector from the results of the DM-POD workflow with ICP alignment analysis of all available cardiac phases, and (c) individual relative modal energy percentage feature vector from the results of the SPHARM workflow with the “Updated” SHREC alignment analysis of only the end diastole cardiac phase.	93
4.1	(a) - (c) The three basis functions selected to artificially generate shapes, (d) - (f) three representative examples of one component of the artificially generated shapes, (g) - (i) the first component of the three modes produced by applying proper orthogonal decomposition, and (j) - (l) the first component of the three modes produced by independent component analysis for the first example of artificially generated shapes with dataset size $n = 3$ and ICA function $g = x^3$	107
4.2	(a) - (c) The three basis functions selected to artificially generate shapes, (d) - (f) three representative examples of one component of the artificially generated shapes, (g) - (i) the first component of the three modes produced by applying proper orthogonal decomposition, and (j) - (l) the first component of the three modes produced by independent component analysis for the second example of artificially generated shapes with dataset size $n = 3$ and ICA function $g = x^3$	108
4.3	Schematic of the statistical shape analysis framework, including (a) segmentation of the image stacks, (b) smoothing and mesh generation, (c) topological mapping, (d) registration, and (e) statistical decomposition.	110
4.4	The cumulative mode/component energy for the results of the right ventricle endocardial surface analyses with proper orthogonal decomposition (POD) and independent component analysis (ICA), where $g1$ refers to $g(x) = x^3$, $g2$ refers to $g(x) = \tanh(x)$, and $g3$ refers to $g(x) = x \exp(-\frac{x^2}{2})$ as applies to the ICA algorithm presented.	112

4.5	The mean shape for the right ventricle endocardial surface dataset and plus or minus two standard deviations of each of the first five modal/component coefficients multiplied with the corresponding mode/component shape and added to the mean shape ($+2\sigma$ and -2σ , respectively) for both the proper orthogonal decomposition (POD) and independent component analysis (ICA) results with $g(x) = x^3$ (the color contours represent the relative magnitude of the modal/component coefficients multiplied with the corresponding mode/component shape).	114
4.6	The distributions of the components of the modal/component energy feature vector (\vec{q}) defined in Eqn. 4.33 and the two groupings (circled) of the 13 patient set obtained from applying K-means clustering for the results of the right ventricle endocardial surface analyses with (a) independent component analysis (ICA) with $g(x) = x^3$ and (b) proper orthogonal decomposition (POD).	116
4.7	Relative individual modal/component contribution (energy percentage) for the first five highest energy modes/components over the cardiac cycle for each of the 13 patients from the results of the right ventricle endocardial surface analyses with (a) independent component analysis (ICA) and (b) proper orthogonal decomposition (POD).	118

PREFACE

I would like to first express my deepest gratitude to my advisor and chair of my graduate committee Professor John C. Brigham. Without his unending faith in my potential and his wonderful and tireless guidance none of my success could have been possible.

My thanks to Doctor Marc A. Simon, not only for serving on my graduate committee, but also for his significant contribution to my education and his generous support during times of need.

I would like to thank Professor Jeen-Shang Lin, Professor Vikas Khanna, and Professor Yongjie (Jessica) Zhang for serving on my graduate committee and for their support throughout my studies.

I also would like to thank my colleagues in Professor John C. Brigham's group for their help and encouragement during my PhD study.

Last, but certainly not least, I would like to thank my family for their love and support, without which I could not have accomplished anything. In particular, I am eternally grateful for my fathers' humble brilliance, my mothers' never ending strength, all of which will always be a source of inspiration.

1.0 A NEW COMPUTATIONAL FRAMEWORK FOR ANATOMICALLY CONSISTENT 3D STATISTICAL SHAPE ANALYSIS WITH CLINICAL IMAGING APPLICATIONS

1.1 ABSTRACT

A computational approach is presented for the quantitative comparison and statistical decomposition of sets of three-dimensional closed genus-0 surfaces obtained from untagged medical images. The core of the analysis procedure consists of a two-step surface parameterization technique followed by the proper orthogonal decomposition method. The capabilities of the proposed approach are demonstrated through analysis and sensitivity tests considering a human right ventricle endocardial surface captured at several time frames over the cardiac cycle, as well as decomposition and classification tests considering several sets of artificially generated three dimensional surfaces.

1.2 INTRODUCTION

There are a multitude of pathologies that significantly and adversely affect human health, which are also known to induce noticeable changes in the shape and/or mechanical behavior of certain organs or other biological structures. Some examples include Alzheimer's disease and Schizophrenia which have been seen to cause hippocampus and brain ventricle shape changes [89, 35, 102] and pulmonary hypertension (PH) which very noticeably alters the shape and mechanical function of the right ventricle [15, 80, 81], among others. Medical imaging methods (such as computed tomography, magnetic resonance imaging, etc.) and

associated developments in image processing have gone a long way to aid physicians in both observing the nature of such shape changes and identifying diagnostic relationships between the shape change and the particular pathology. However, there are situations where although a shape change is known to occur and the nature of this change is suspected to be linked with pathology, clinical scientists have been so far unable to find measurable quantitative features that discriminate various states in the pathology and/or treatment outcomes. For example, while PH is observed to dramatically change the components of the size and shape of the right ventricle [74, 80], features of this shape change have yet to be identified to accurately predict the likelihood of right ventricle failure (often leading to death), in large part due to the complex three-dimensional (3D) geometry.

Some recent work has taken a generalized approach to analyzing and contrasting the shape of a collection of biological structures from medical imaging data [41, 21, 55]. What is particularly significant about these works is that they attempt to develop a point-wise mathematical description (i.e., parameterization) of the anatomical surface defined with respect to a unified reference state or otherwise made mathematically comparable across the population. Once parameterized such that each shape is uniquely comparable to one another, pattern recognition approaches can be applied to optimally decompose, cluster, and build classifiers from a collection of shapes, with no *a priori* selection of the nature or location of the most significant discerning features.

There are a variety of methods that have been implemented for the quantitative comparison of 3D shapes with different benefits and shortcomings, particularly for application in medical imaging analysis [67, 57, 70, 69, 101, 23]. In particular, there have been considerable recent work developing approaches based on harmonic mapping to parameterize 3D closed surfaces for statistical shape analysis [34, 7, 41]. The harmonic mapping approach has been shown to produce unique one-to-one mappings, but a key constraint of these approaches is that the shapes of interest must be closed genus-0 topologies. However, the genus-0 description can be a suitable approximation for the aforementioned organs as well as many other biological structures. If the shapes are suitable, some variation of harmonic mapping can be applied to map each shape to the surface of a unit sphere (i.e., transform the Cartesian coordinates to the spherical latitude and longitude) from which they can be

quantitatively compared to one another. These techniques have been shown to be applicable to a wide variety of shapes and have been coupled with several decomposition and pattern recognition techniques. However, while there are several implementation variations, the current approaches have so far been mesh dependent to a degree in their implementations, and they have often included steps to optimize the mesh distribution after mapping to the unit sphere which can add an element of nonuniqueness in the mapping process. Moreover, the techniques developed thus far have an additional required step following the application of mapping, but before applying pattern recognition techniques, to project the mapped surfaces onto a predefined basis (e.g., spherical harmonic functions [43]) and/or use some form of downsampling (typically caused by the datasets being required to be in discrete vector form).

This work presents a novel approach to the process of statistical shape analysis of 3D closed genus-0 surfaces for applications in medical imaging. The approach includes a modified implementation of the harmonic mapping procedure that allows for shapes to be uniquely and consistently converted into comparable surface representations with a minimal amount of required referential information. The mapping can be applied in an anatomically consistent manner, potentially bypassing the need for aligning the images with a registration step, and allows the surfaces to be analyzed quantitatively as continuous functions for general applicability regardless of population and processing variation. The approach is then able to utilize the method of proper orthogonal decomposition (i.e., principal component analysis or Karhunen-Loeve transform, depending on the context) [6, 12, 5] applied directly to the set of surface representations following the mapping (i.e., without any further conversion to a different basis such as spherical harmonic functions or downsampling) to identify shape features that describe the set of biological shapes in some optimal sense. Lastly, the shape features can be used to cluster (e.g., k-means clustering) and build classifiers (e.g., linear discriminant analysis) [26] to use shape to predict the classification of biological structures (e.g., diagnose pathology).

In Section II, the details of the methods are outlined, including the harmonic mapping method for defining a unique mathematical representation of a given 3D closed surface and the proper orthogonal decomposition strategy to derive the defining shape features

from a given collection of surfaces. Section III presents a set of example analyses showing the capabilities of the proposed approach. Specifically, the mapping and decomposition techniques are thoroughly analyzed with respect to the chosen referential points and the initial segmented surface parameterization (i.e., surface mesh) with the analysis of a single human right ventricle endocardial surface over the cardiac cycle obtained clinically from computed tomography imaging. Then, the capabilities of the approach to recover and classify known patterns in shape datasets is shown through the analysis of sets of artificially generated 3D shapes created with linear combinations of spherical harmonic basis functions, which is followed by the concluding remarks in Section IV.

1.3 METHODS

The present work assumes that a collection of continuous, 3D, non-overlapping, closed genus-0 surfaces has already been obtained, with the k^{th} surface domain labeled as $\Omega_k \subset \mathbb{R}^3$, and all surfaces are defined in some consistent global coordinate system \vec{x} . A typical structure for each surface could be a collection of surface points that have been segmented from a stack of medical images and their corresponding interpolation that uniquely connects each point to form a continuous surface (e.g., a mesh of linearly interpolated elements). The approach presented is only directly applicable to genus-0 shapes, which can feasibly lead to several applications in biological structures including the right ventricle example that will be shown. However, the surface parameterization approach could certainly be extended or replaced by an existing approach to accommodate open surfaces or high genus objects with the remaining framework still being applicable.

1.3.1 Surface Parameterization

In order to quantitatively compare multiple surfaces in a general way, each surface must first be defined mathematically (i.e., mapped) with respect to a common reference state (e.g., defined as a function over some fixed reference geometry, rather than a collection of

points with respect to an arbitrary origin). While this parameterization is an inherently nonunique problem and there are many ways to perform such a mapping, of critical importance is that the mapping consistently provides unique and one-to-one representations of each surface (see [30] for an overview of several approaches to parameterize surfaces, such as conformal mapping, isometric mapping, equiareal mapping, etc.). An additional issue for clinical applications in medical imaging is that the parameterization should ideally require minimal user input (e.g., anatomically defined reference points). This constraint is due to current limitations on image tagging and implanting markers in a clinical setting leading to few possible fiducial points in many biological structures.

A harmonic mapping to the unit sphere is one such mapping that satisfies the desired constraints for medical imaging applications, and has already been shown in several cases to provide consistently unique, one-to-one, and non-overlapping surface representations for a wide variety of genus-0 shapes (see [11] for an in-depth overview of the theory and potential applications of harmonic mappings). By definition, a harmonic mapping (i.e., change in coordinates) is simply a parameterization that satisfies Laplace’s equation for each new parameter. As such, choosing the new parameters to be the spherical coordinates, ϕ (longitude) and θ (latitude), the spherical coordinates for each point on the given surface (i.e., location on the surface of the unit sphere) can be determined from the solution of the following differential equations

$$\nabla^2\theta(\vec{x}) = 0 \quad \text{in } \Omega_k, \quad \nabla^2\phi(\vec{x}) = 0 \quad \text{in } \Omega_k. \quad (1.1)$$

Defining sufficient boundary conditions on ϕ and θ is then all that is necessary to uniquely determine a value of latitude and longitude on the unit sphere for every point on the original surface Ω_k . One perceived downside to directly applying the harmonic mapping is that the surface may be distorted in the mapped domain as a majority of the surface may have ϕ and/or θ values within a relatively small range, which may degrade the subsequent analysis. Therefore, a common practice is to add an additional relaxation step in the mapping process [37]. In the cases that define the original surface as a mesh, this relaxation typically seeks to optimize the mapping so that the elements in the mapped domain are as regularly distributed as possible (e.g., so that element internal angles and area are nearly constant in the range

of ϕ and θ). However, such relaxation methods imply that the original surfaces should have consistently uniformly distributed and well-behaved meshes themselves [11, 1], as a locally refined or otherwise distorted starting mesh may become inconsistently distributed when forced to be evenly distributed in the mapped domain. Remeshing can be applied to the original surfaces in some instances to obtain the desired initial uniform meshes, but the process may be time consuming and potentially result in feature loss. The present work employs a variant on the typical two-step process, in which the harmonic mapping is applied initially and then a secondary mapping is applied to improve the distribution of the surface in the mapped domain. This modified approach is completely deterministic and requires minimal user defined referential data, providing a means to analyze a set of medical images in a uniquely anatomically consistent manner, and has no dependence upon the uniformity of the original surface meshes.

1.3.1.1 Initial Parameterization To implement the harmonic mapping procedure and solve Equation (3.1), it is first necessary to provide suitable boundary conditions for the spherical coordinates ϕ and θ . This work incorporates a combination of the techniques that have been shown thus far in the literature [11, 103, 71] to produce a unique method of defining and implementing the boundary conditions that requires a minimal amount of referential data and is not significantly dependent upon the surface mesh dimensions. For this approach each surface must have at minimum two reference points and a reference line: a point defined as the north pole (Γ_n), a point defined as the south pole (Γ_s), and a continuous non-overlapping line defined as the date line (Γ_d) that connects the two poles. In practice, the references should be related to some identifiable component of the anatomy for consistent comparisons between surfaces. It should be noted that the date line has a nonunique mapped value as it represents where the longitude passes 360° . As such, the surface is cut along the date line to create two overlapping, but independent boundaries: an east date line (Γ_d) and west date line (Γ_d^o). Thus, the values of the spherical coordinates along the references will be assigned as

$$\begin{aligned} \theta &= 0 \quad \text{on } \Gamma_n, & \theta &= \pi \quad \text{on } \Gamma_s, \\ \phi &= 0 \quad \text{on } \Gamma_d, & \phi &= 2\pi \quad \text{on } \Gamma_d^o. \end{aligned} \tag{1.2}$$

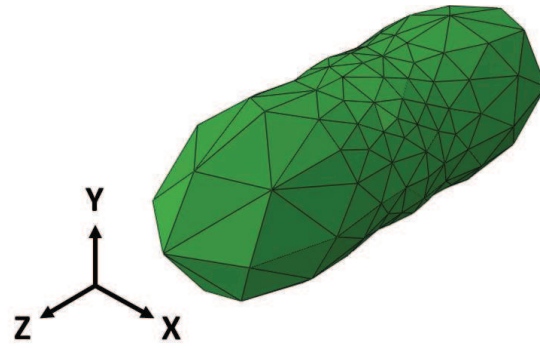
The reference choices are entirely at the discretion of the user and additional anatomical information can be easily added beyond the minimal data requirement through intermediate data lines or other similar boundary conditions. In addition, since the poles of a sphere have no value for longitude, to solve for the longitudinal mapping, a region around each pole must be removed in the domain for the boundary value problem of ϕ in Equation (3.1). This can typically be done by removing all elements connected to the poles when solving for ϕ .

The resulting boundary value problems described by Equation (3.1) and Equation (2.2) can be solved through any preferred approach (e.g., finite element or boundary element method) for the spherical coordinates of each surface point, with the finite element method having been employed for the results herein. Lastly, the region removed for the longitudinal mapping is replaced in the mapped domain by connecting all of the northmost and southmost points to the pole and adding a vertex with the latitude value of the corresponding pole and longitude value of the connecting points, as shown in Fig. 1.1b. Once mapped, any given surface (defined by all $\vec{x} \in \Omega_k$) can be described continuously with respect to a common domain as

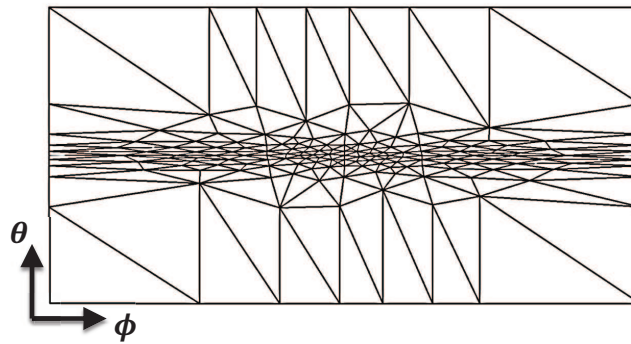
$$\vec{x} = \vec{x}(\theta, \phi) \quad \text{in } \theta \in [0, \pi], \phi \in [0, 2\pi]. \quad (1.3)$$

Therefore, the mapped shapes can be quantitatively compared continuously over the entire surfaces in terms of the spherical coordinates to assess variations, identify patterns, etc. However, the results from this initial parameterization may not be ideal for further numerical analysis. As shown in Fig. 1.1b, the vertices (i.e., nodes) of the original surface mesh are relatively uniformly distributed over the original surface, but after mapping most of the vertices are concentrated in the middle third of the latitude domain. While not necessarily an issue in all circumstances, depending on the subsequent statistical analysis used, details may be lost due to the concentration of the surface information over a relatively small portion of the referential domain. As discussed previously, to compensate for these potential difficulties (if necessary) a secondary mapping is performed to more uniformly distribute the mapped vertices over the domain of the spherical coordinates.

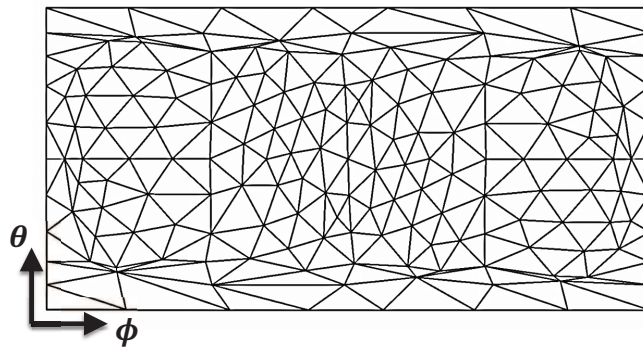
1.3.1.2 Secondary Parameterization Contrary to the approaches currently found in the literature, the present work uses a completely deterministic mapping process, so an



(a)



(b)



(c)

Figure 1.1: Example of (a) a 3D genus-0 shape, (b) the results of the initial parameterization, and (c) the results of the secondary parameterization.

optimization step was therefore not considered applicable (note, the mapping is inherently nonunique and the nonlinear optimization strategies to improve the mesh distribution would likely lead to results that depend strongly on optimization parameters). Alternatively, this work recognizes that the harmonic parameterization of a sphere defines the relationship between a uniformly distributed mesh over the unit sphere domain (the same domain as the mapped domain) and the distortion caused by the mapping. As such, the key assumption used here is that the inverse of the harmonic mapping of the sphere will bring any distorted mapped mesh closer to a uniformly distributed mesh over the unit sphere domain. To apply this concept the initial parameterization procedure is performed for a unit sphere as the surface (Ω) to produce the mapping

$$\vec{X}(\theta_u, \phi_u) = \vec{x}(\theta, \phi), \quad (1.4)$$

where

$$\vec{X} = [\sin(\theta_u)\cos(\phi_u), \sin(\theta_u)\sin(\phi_u), \cos(\theta_u)]^T, \quad (1.5)$$

and θ_u and ϕ_u are the latitude and longitude of the unit sphere without mapping, respectively. Equation (2.3) and Equation (2.4) can then be rearranged to produce the relationship between distorted and undistorted spherical coordinates as

$$\theta_u = \theta_u(\theta, \phi), \quad \phi_u = \phi_u(\theta, \phi). \quad (1.6)$$

To apply this secondary parameterization to a given surface, it is then only necessary to substitute the results from the initial parameterization Equation (3.1) into Equation (2.5) to obtain the parameterization of the given surface in terms of θ_u and ϕ_u . Fig. 1.1 shows an example of a parameterized surface before and after the secondary parameterization, with the final mesh being clearly more uniformly distributed than the mesh after only the initial parameterization.

Of particular significance is that since both the initial and secondary mappings are unique and one-to-one, the final mapping between the original surface and the unit sphere ($\vec{x}(\theta_u, \phi_u)$ for Ω_k) will also be unique and one-to-one. Moreover, the subsequent analysis will not project the mapping onto another pre-chosen basis (such as spherical harmonic functions)

and will avoid downsampling requirements by maintaining and analyzing the mapped surface descriptions as continuous functions. Therefore, provided with sufficiently refined numerical integration, no secondary parameterization at all should theoretically be necessary to ensure that all salient features are captured through the analysis. The benefit to a secondary parameterization for this case is thus to reduce the computational expense of the numerical integration, but it is not a necessary step to the process.

1.3.2 Shape Mode Decomposition

Once a set of n surfaces is converted to a set of shape functions over the referential unit sphere domain, the application of a decomposition strategy to determine and rank the fundamental shape components that exist within the set is relatively straightforward. This work applies the method of proper orthogonal decomposition (POD), which is often interchangeably referred to as principal component analysis or Karhunen-Loeve transform, but is differentiated here as POD since it will be formulated in the space of continuous functions. POD has been used successfully in a variety of pattern recognition and reduced-order modeling applications [6, 12, 5], and it is particularly beneficial to this work as it is well known to be tolerant to noise, and the continuous function formulation allows for a set of shape functions to be analyzed without further processing regardless of mesh conformity (e.g., varying mesh density and/or node distribution throughout the set).

The main objective of POD is to identify the m basis functions (i.e., modes or features) $\{\vec{v}_i(\theta, \phi)\}_{i=1}^m$ that are optimal in the average sense for representing the given set of n surfaces (i.e., set of snapshots) $\{\vec{x}_k(\theta, \phi)\}_{k=1}^n$. For a linear form of this approach, each surface is approximated as a combination of the global shape modes as

$$\vec{x}_k(\theta, \phi) \approx \vec{\bar{x}}(\theta, \phi) + \sum_{i=1}^m a_{ki} \vec{v}_i(\theta, \phi), \quad (1.7)$$

where a_{ki} is the coefficient that best approximates the k^{th} shape with the i^{th} mode, and $\vec{\bar{x}}(\theta, \phi)$ accounts for a translation in the dataset (note that $\vec{\bar{x}}(\theta, \phi)$ is often taken as the mean of the dataset, but is not required to be so, and in fact, two different definitions were applied in the present work). Then, the optimal basis is defined as that which minimizes the average

of the L_2 -norm of the difference between each snapshot and the best approximation of the snapshot leading to the following optimization problem

$$\min_{\{\vec{v}_i(\theta, \phi)\}_{i=1}^m} \langle \|\vec{x}_k(\theta, \phi) - \vec{x}_k^*(\theta, \phi)\|_{L_2}^2 \rangle, \quad (1.8)$$

where $\vec{x}_k^*(\theta, \phi)$ is the best approximation to $\vec{x}_k(\theta, \phi)$ through Equation (3.11), which can be obtained using the projection operator. Lastly, through several manipulations including applying the method of snapshots, the optimal modes can be solved deterministically through the following eigenvalue problem (see[5] and the references therein for details)

$$\frac{1}{n} \sum_{k=1}^n A_{jk} C_k^{(i)} = \lambda^{(i)} C_j^{(i)}, \quad (1.9)$$

where

$$A_{jk} = \int_0^{2\pi} \int_0^\pi (\vec{x}_j - \vec{x}) \cdot (\vec{x}_k - \vec{x}) \sin(\theta) d\theta d\phi, \quad (1.10)$$

and

$$C_k^{(i)} = \int_0^{2\pi} \int_0^\pi (\vec{x}_k - \vec{x}) \cdot \vec{v}_i \sin(\theta) d\theta d\phi. \quad (1.11)$$

The n -dimensional eigenvalue problem can be solved to obtain at most n modes as

$$\vec{v}_i(\theta, \phi) = \frac{1}{\lambda^{(i)} n} \sum_{k=1}^n (\vec{x}_k(\theta, \phi) - \vec{x}(\theta, \phi)) C_k^{(i)}. \quad (1.12)$$

Depending on the objective of the analysis, the translation function $\vec{x}(\theta, \phi)$ can be taken as the null shape (i.e., zero), the mean shape (i.e., the average of the dataset), or some reference shape so that the analysis corresponds to change in shape (i.e., pseudo-deformation), which will all lead to different results and different physical interpretations.

Note that the corresponding eigenvalues ($\lambda^{(i)}$) relate to the relative importance of each mode, with the larger eigenvalues corresponding to modes that are more significantly representative of the dataset. As an added benefit, the lowest eigenvalues (i.e., lowest energy modes) are typically associated with noise, allowing for spurious components to be identified and ultimately removed. In practice, the modes themselves could provide a physical understanding of the fundamental aspects of shape and kinematics of a given biological structure. For classification purposes the highest energy modes are chosen (a typical rule of thumb is to choose enough modes to capture 99% of the total eigenvalue sum of the set), and the coefficients of these modes for each surface in the set, which are obtained by projecting the surface onto each mode, are used to define the surfaces and build classifiers.

1.4 EXAMPLES AND DISCUSSION

Two sets of example analyses are presented to display the capabilities of the proposed approach. First, the analysis of a set of human right ventricle endocardial surfaces (RVES) sampled at several points in time during one full cardiac cycle is shown. The primary objective of the RVES analysis was to display the implementation process and the nature of the results obtained in a clinical context, and more importantly, to assess the sensitivity of various parameters of the images themselves (e.g., surface mesh description) and the processing steps (e.g., data line selection) with respect to the resulting mapping and fundamental shape features that can be obtained. While a potential benefit of the proposed approach is that the continuous form of the analysis leads to applicability across patient sets and for differing imaging modalities, for simplicity, the present work only considered the single patient with a single imaging modality. However, for example, the analysis presented in [94] displays how the approach can be consistently applied to a population of patients. In contrast, the second example set shows the analysis of collections of shapes that were artificially created through randomly generated combinations of spherical harmonic basis functions. This second set was intended to assess, and specifically verify the capabilities of the proposed approach to identify discriminating features that will then be able to appropriately classify sets of shapes for cases in which patterns are known to exist, which would not be possible (in an absolute sense) to show with clinical data.

1.4.1 Human Right Ventricle Endocardial Surface

The human right ventricle is a particularly well suited application for the proposed methods as it is well known to show significant shape changes due to pathology [80], the shape can be represented as a closed surface, and sufficient anatomical reference points can be consistently identified. For this example, a set of clinically obtained cardiac computed tomography images was obtained for a single patient with normal hemodynamics and with nine evenly spaced time frames during one complete cycle (end diastole to end diastole). The RVES at each of the nine time frames was manually segmented and smoothed using a standard recursive and

discrete Gaussian filter within the commercial medical image processing software Simpleware¹ to remove the high-frequency surface oscillations that occur from the segmentation of stacked images. The endocardial surface was chosen due to the improved imaging contrast between the wall tissue and blood, which allows for a far more accurate segmentation of the endocardial surface in comparison to the epicardial surface.

As would be expected, there are no implanted markers, and therefore, only anatomical locations can be used for the mapping references. This work considered three options for selecting the mapping reference points (as described in Section 1.3.1.1) to compare and contrast the features that could be obtained from different anatomical references. The three choices included: (1) the anterior border between the free wall and septum (date line) with endpoints at the intersection with the pulmonary valve and apex (poles), (2) the posterior border between the free wall and septum with endpoints at the pulmonary valve and the tricuspid valve, and (3) the closed loop including the border between the free wall and septum from the pulmonary valve to the apex to the tricuspid valve and back to the pulmonary valve. Fig. 1.2 shows an example of the RVES shape at end diastole along with the three anatomical options discussed for the mapping reference points.

In all cases tested, each segmented surface was topologically mapped and then the difference between each shape and the end diastole shape was calculated to produce a pseudo-displacement field (i.e., change in shape) of the RVES at each time frame of the cardiac cycle. In other words, the translation shape ($\vec{x}(\theta, \phi)$ in Equation (3.11)) was taken to be the end diastole shape. Of particular importance is that by using the pseudo-displacement field the analysis is able to bypass the costly and potentially uncertain step of registering the shapes to one another since the pseudo-displacement fields are naturally comparable to one another with respect to the chosen base shape (end diastole herein). Lastly, the collection of pseudo-displacement fields was decomposed in each test case using POD to obtain the fundamental modes and their relative mode energy of the pseudo-displacement of the RVES.

1.4.1.1 Mesh Sensitivity/Convergence: As is common, the segmented surfaces were described by a mesh of triangular surface elements with linear interpolation. However, an

¹www.simpleware.com

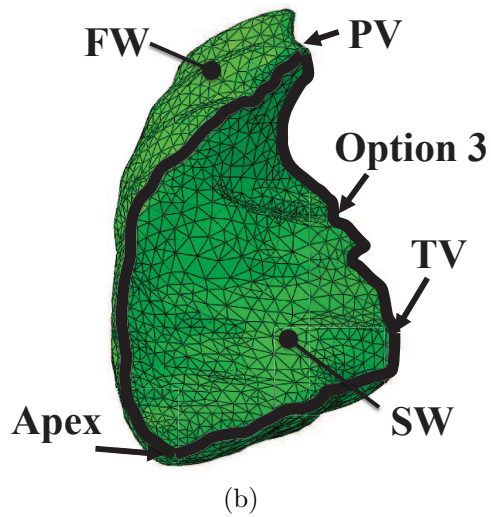
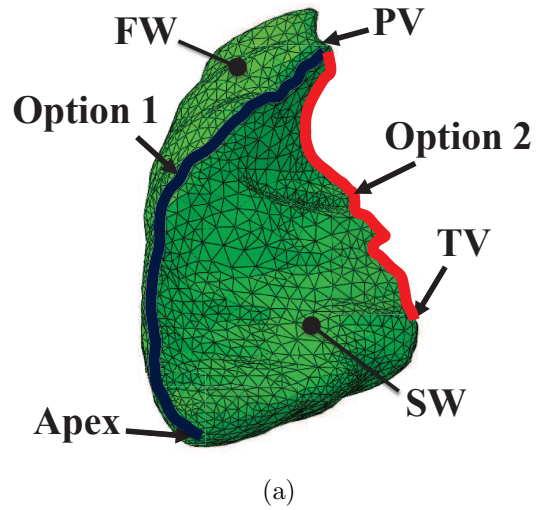


Figure 1.2: Example of a RVES shape at end diastole with the free wall (FW), septal wall (SW), pulmonic valve (PV), tricuspid valve (TV), (a) Options 1 and 2, and (b) Option 3 for the potential date line segments labeled.

important point is that both the accuracy of the surface representations (i.e., ability to capture the shape) and the solutions to Eqn. 3.1 will be dependent to some extent upon the relative size of the elements in the surface mesh. Therefore, an important first step to assess the proposed methods (particularly the mapping) is to analyze the sensitivity to mesh variations and confirm the ability to verify the numerical process through mesh convergence (i.e., refinement of the mesh until the solution stabilizes). As such, to test the effect of mesh size on the RVES analysis and ensure that the mesh was sufficiently refined for the following test cases three different mesh densities were tested, as shown in Fig. 1.3: 3586 total elements (i.e., coarse mesh), 10810 total elements (i.e., fine mesh), and 43382 total elements (i.e., very fine mesh). As a representative example, the relative (with respect to the less refined mesh) L_2 -norm of the difference in the initial mapping results for the three mesh cases using Option 1 for the date line (i.e., pulmonary valve to the apex) was: 0.92% for coarse-fine, 1.44% for coarse-very fine, and 0.35% for fine-very fine. A less than 1.5% change in the initial mapping results for more than an order of magnitude increase in the number of elements (from coarsest to finest) can certainly be considered a sufficient level to imply mesh convergence of the initial mapping results (and this was representative of the other RVES time frames and test cases). Furthermore, since all subsequent analyses maintain the representation of the surfaces as continuous functions, mesh convergence of the initial parameterization should be sufficient to imply mesh convergence for the entire mapping and decomposition process. As such, all subsequent analyses utilized the coarse mesh description for reduced computational expense.

The mapping process was then completed for all 9 RVES time frames with date line Option 1, the pseudo-displacement fields were calculated, and POD was applied to obtain the pseudo-displacement modes. For this case, the first three modes contained more than 99% of the total energy. Fig. 1.4 shows the first three modes of the decomposition in the top row and the reconstructed pseudo-displacement fields in the matrix below progressing through the cardiac cycle from top to bottom. The first three columns are the displacement reconstructed with the first mode, the first two modes, and the first three modes, from left to right to show how each mode contributes to the total reconstruction, and the final column is the full displacement field after mapping and using POD to remove the low energy modes

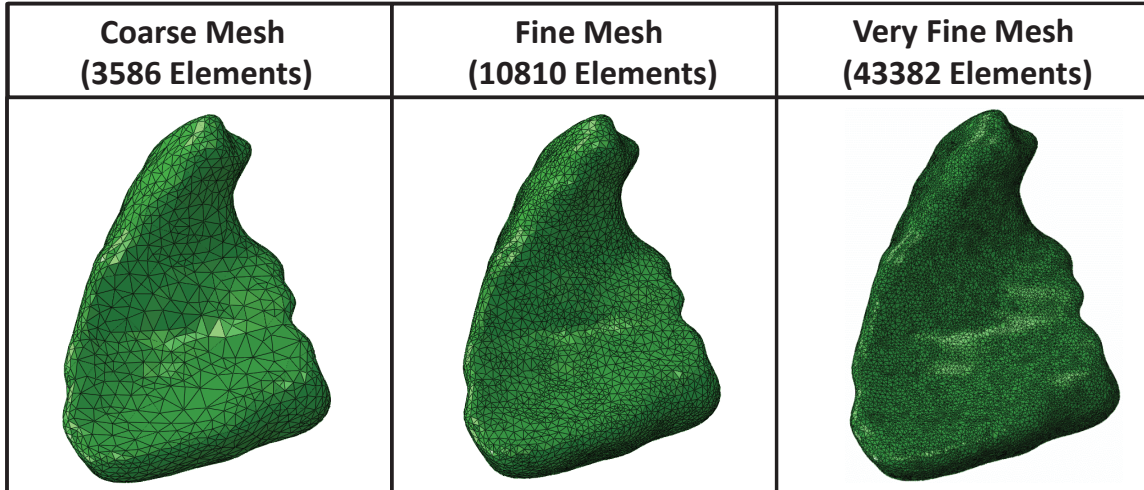


Figure 1.3: Three different mesh sizes used to test mesh size sensitivity for a representative human right ventricle at end diastole.

(likely noise). Fig. 1.5 shows the relative amplitude (relative to the maximum of the three coefficients over the cardiac cycle) of the first three modes of the decomposition over the cardiac cycle.

While the resulting modes and their coefficients are entirely relative to the choices of anatomical references, there can still be some physical interpretation derived from the resulting decomposition, particularly in terms of localizing variations. For example, in this individual Mode 1 appears to represent contraction or dilation of the free wall, with a higher concentration in the main body of the RV (i.e., away from the outflow track), with the apex and pulmonary valve displacing little. By contrast, Mode 2 appears to contain deformation that is concentrated in the outflow track and in the region of the free wall nearer to the tricuspid valve. Mode 3 is the least significant/influential of the modes shown here, and includes various local deformations concentrated around the pulmonary valve and in the free wall below the tricuspid valve. Furthermore, it can be clearly seen in Fig. 1.5 that during systole mode 2 acts first to contract the outflow track followed by a strong increase in mode 1 to contract the main RV body. During diastole both modes 1 and 2 act simultaneously to

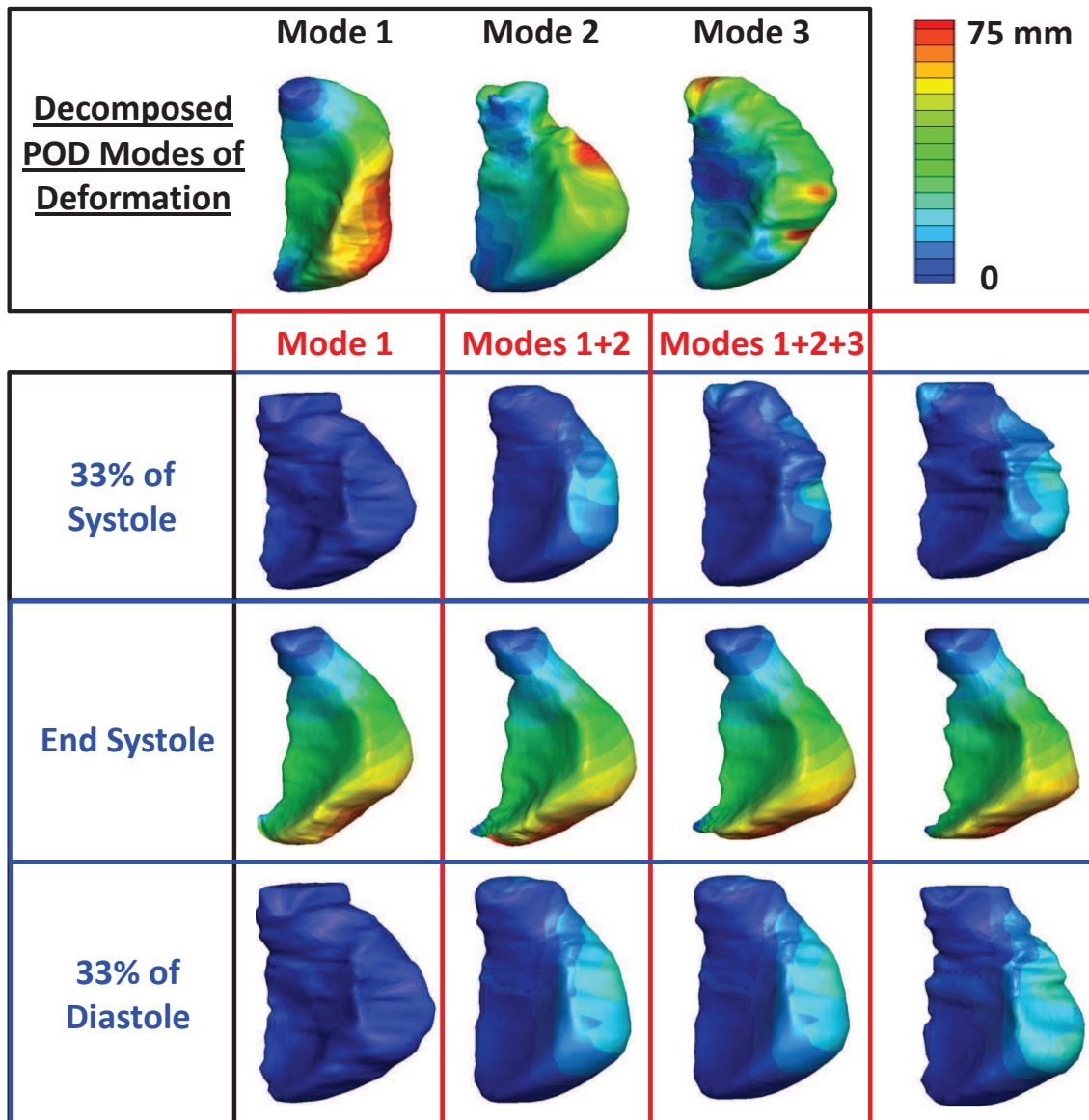


Figure 1.4: Modal decomposition and reconstruction of the RVES pseudo-displacement field over the cardiac cycle (contours represent displacement magnitude).

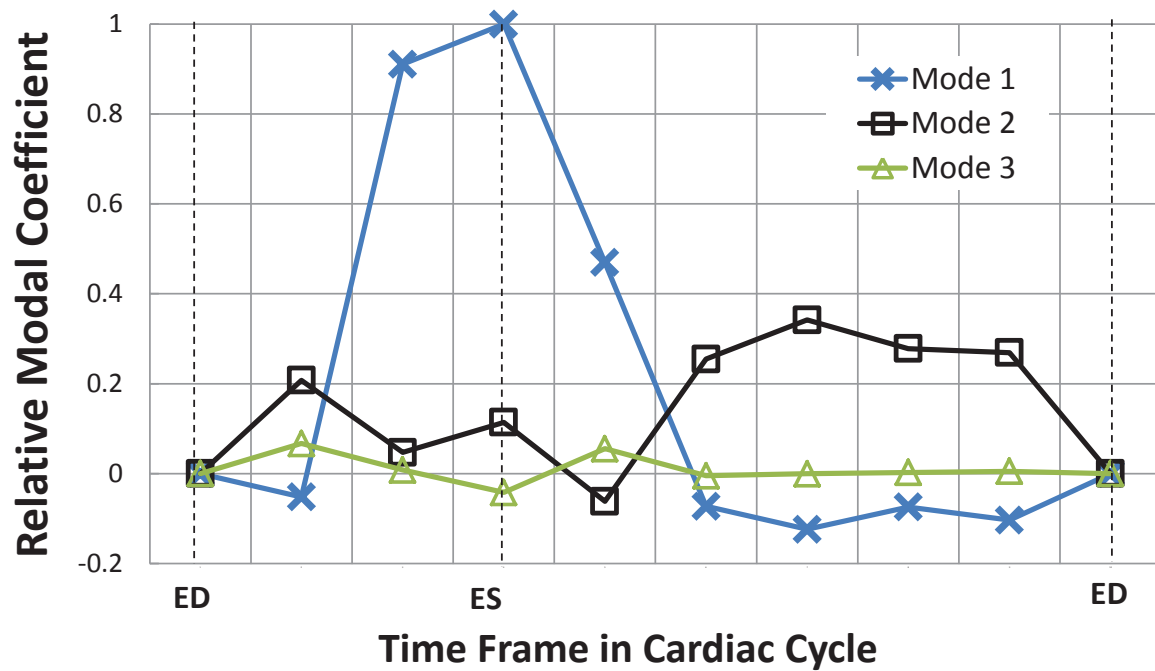


Figure 1.5: Relative amplitude of the modal coefficients for the first three POD modes over the cardiac cycle (from end diastole (ED) to end systole (ES) and then back to ED).

present the relatively high speed overall expansion of the ventricle followed by more expansion through the main body of the RV (Mode 1) and elongation in the outflow track (Mode 2).

1.4.1.2 Sensitivity to Anatomical References: The mapping and decomposition process was repeated for all three of the chosen options for the referential data: the pulmonary valve to the apex (Option 1), the pulmonary valve to the tricuspid valve (Option 2), and the complete loop of the pulmonary valve to the apex to the tricuspid valve and back to the pulmonary valve (Option 3), as shown in Fig. 1.2b. In particular, Option 3 is fundamentally different than the first two in that it is a closed loop over the surface. In order to perform the mapping with Option 3 two points still need to be defined as the poles, and therefore the two separate segments between the poles represent two different date lines with unique values for the longitude. For this example, Option 3 used the pulmonary valve and apex as the poles, the date line segment that coincides with Option 1 had the original values of longitude of 0 and 2π applied, and the remaining date line segment had a longitude value of π applied.

As would be expected, all three options for the referential data produce substantially different initial mapping results, whereas the mode shapes (as shown in Fig. 1.6), and similarly the modal coefficients in time (not shown here for the sake of brevity), of the pseudo-displacement are nearly identical for Options 1 and 3, but different for Option 2. These results highlight the importance of maintaining consistency with the selection of the anatomical features that will be used for the referential data in the mapping process for each shape in a given dataset, as the shape features obtained will depend significantly on this choice. Furthermore, the reference choices of the poles appear to be particularly significant (in comparison to the date line) based on the relative similarity in the results for Option 1 and 3 that share the same poles, while the additional date line information of Option 3 has a relatively small effect on the resulting modes. This may of course limit the potential applicability of this approach to instances similar to this RVES example in which at least two clear and consistently identifiable anatomical reference points can be determined. However, this may be seen as a relatively modest cost for an anatomically consistent comparison of


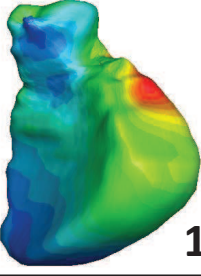
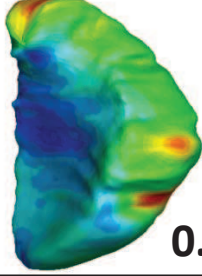

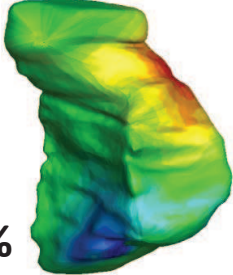
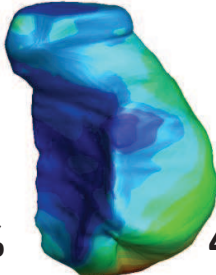


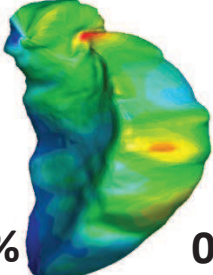
Dateline	Mode 1	Mode 2	Mode 3
Option 1	 83.1%	 15.6%	 0.7%
Option 2	 84.9%	 9.0%	 4.2%
Option 3	 84.0%	 14.5%	 0.9%

Figure 1.6: First three POD modes and corresponding mode energy for the RVES pseudo-displacement for the three options for the referential data.

sets of biological shapes. Based on the similarity of Options 1 and 3 and the relative ease in consistently identifying the pulmonary valve and the apex, for the remaining tests only Option 1 was used for the mapping reference data.

1.4.1.3 Sensitivity to Reference Point Perturbations: While there is clear sensitivity to variations in the anatomical choices for the mapping reference data, it is also important to understand the potential changes in the mapping and decomposition results that could be caused by errors (i.e., inconsistency) in segmentation and/or improperly identifying the anatomy. Therefore, for the final test of the RVES example the poles and date line were perturbed for the end diastole shape, and the mapping and decomposition processes were repeated and compared. End diastole was chosen as the representative example because it was found to have a slightly stronger effect on the decomposition results than the other time frames, which is likely due to the fact that end diastole is taken as the translation shape (see Eqn. 3.11) and thus simultaneously affects each snapshot in the decomposition process. The test cases included perturbing the location of the PV pole by approximately $6mm$, the apex pole by approximately $9mm$, and perturbing both poles simultaneously (approximately $15mm$ total change); and then shifting the date line eastward, shifting the date line westward, and shifting half of the date line eastward and half westward (i.e., s-shaped perturbation) by approximately $2 - 3mm$ at each point along the date line. For reference, the total original date line length (from PV to apex) was approximately $126mm$ for the end diastole shape. Based on the nature of the RVES surfaces considered here, these perturbation values were deemed reasonable representations of errors that could occur in selecting the reference data. In all cases the mapping and decomposition results were found to be tolerant to reasonable errors in the selection of the mapping reference poles and date lines. The most significant changes occurred due to modification of the poles, with the largest change in the relative (with respect to the original poles and date line Option 1) L_2 -norm of the difference in the initial mapping results of 1.55% when the PV and apex poles were both moved, while perturbations in the date line caused differences that were all less than 0.5%. Furthermore, such minor changes in the initial parameterization expectedly lead to relatively minor changes to the modes of the pseudo-deformation.

1.4.2 Artificially Generated Shapes

To show the pattern recognition capabilities of the proposed methodology shape sets were artificially generated through linear combinations of spherical harmonic functions, first using only symmetric functions, and then including asymmetric functions. These simulated examples were intended to explore the robustness and effectiveness of the techniques presented to recover patterns and classify data in comparison to the basis used to generate the data (i.e., the built-in pattern). Spherical harmonic functions were chosen to create the datasets because they are capable of easily creating genus-0 3D closed surfaces and have been implemented extensively in other works to represent biological structures such as the hippocampus [39] and the heart [43] (to be clear, note that the harmonic topological mapping that is applied in the proposed framework is an unrelated concept to spherical harmonic functions).

Six spherical harmonic functions were chosen to define the radial component in spherical coordinates of the artificial surfaces and create the test sets of 3D closed surfaces (i.e., the set of surface domains Ω_k): the symmetric functions derived from degree 0 order 0, degree 2 order 0, and degree 4 order 0, and the asymmetric functions derived from the real portion of degree 1 order 1, degree 2 order 1, and degree 1 order 2 of the spherical harmonic functions. In addition, to show the robustness of the techniques and improve the realism of the tests, artificial noise was included in each shape. It is expected that in practice the surfaces segmented from medical images to be analyzed would be smoothed to remove any high frequency variations that are expected when segmenting stacked images (as was done in the previous example). Therefore, pointwise white noise was not considered realistic. Alternatively, piecewise smooth noise was generated by dividing the surface into patches and assuming the noise varies harmonically with independent amplitudes over each patch. As such, for the following tests the spherical coordinates were divided into 32 regions by $\frac{1}{4}\pi$ with respect to the spherical coordinates and the noise was defined as

$$\begin{aligned} N(\theta, \phi; i) &= A_i(\sigma_N) \sin(4\theta) \sin(4\phi), \\ &\text{for } i = 1, 2, \dots, 32, \end{aligned} \tag{1.13}$$

and

$$A_i(\sigma_N) \sim \mathcal{N}(0, \sigma_N^2). \quad (1.14)$$

i is the index for the subregions and σ_N is the standard deviation of the randomly generated noise amplitude. For the examples presented herein the standard deviation was defined based on a signal to noise ratio of $30dB$, which was considered suitable with respect to the potential segmented medical image applications. Thus, each shape in the datasets was generated as

$$\Omega_k = \left\{ \vec{x} : \vec{x}(\theta, \phi) = R(\theta, \phi) \begin{bmatrix} \sin(\theta) \cos(\phi) \\ \sin(\theta) \sin(\phi) \\ \cos(\theta) \end{bmatrix}, \right. \quad (1.15)$$

$$\left. \theta \in [0, \pi], \phi \in [0, 2\pi] \right\},$$

with

$$R(\theta, \phi) = \sum_{j=1}^m \alpha_j Y_j(\theta, \phi) + N(\theta, \phi), \quad (1.16)$$

and with the spherical harmonic functions Y_j . m was taken as 3 to produce symmetric shapes (six representative shapes are shown in Fig. 1.7a-f). and 6 for asymmetric shapes (six representative shapes are shown in Fig. 1.7g-l). The coefficients (α_j) were randomly generated from normal distributions with independent means and variances for each coefficient group (corresponding to each basis function). For the symmetric shapes the means and variances were randomly chosen from uniform distributions between 0 to 1 and 0.5 to 1, respectively. In addition, the following constraint was placed on the symmetric shape coefficient sets

$$\alpha_1 > 1.43(\alpha_2 + \alpha_3). \quad (1.17)$$

For the asymmetric shapes the first coefficients were generated with $\alpha_1 \sim \mathcal{N}(5, 100)$ and the remaining α_j with independent means and variances randomly chosen from uniform distributions between 0 to 1 and 0.5 to 1, respectively. These distributions of coefficients ensured that the shapes were all genus-0.

To perform the mapping of the artificially generated shapes, the poles and date lines were chosen to correspond with those from a sphere. In other words, according to Equation (1.15) the north pole corresponded to $\theta = 0$, the south pole corresponded to $\theta = \pi$ and

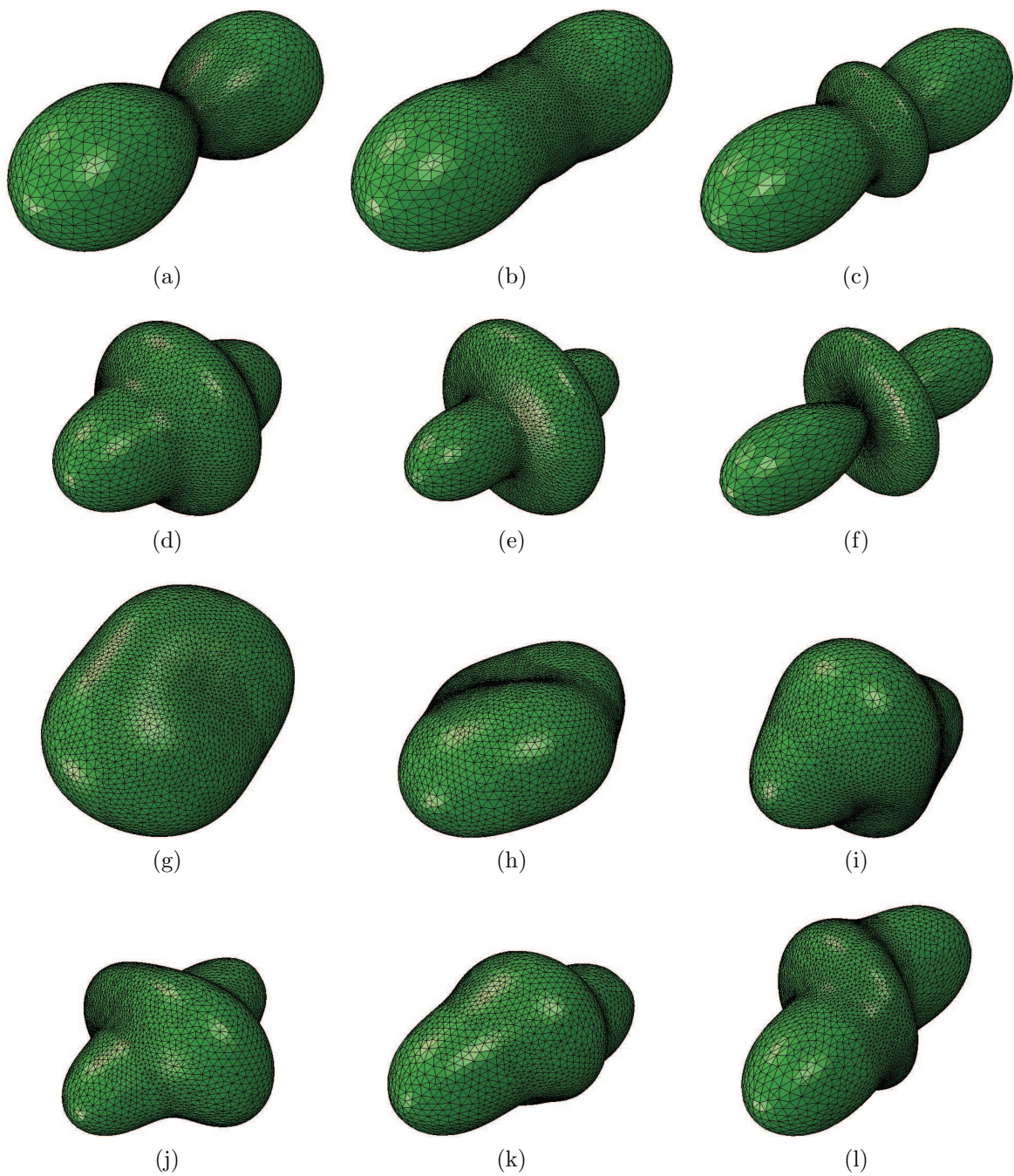
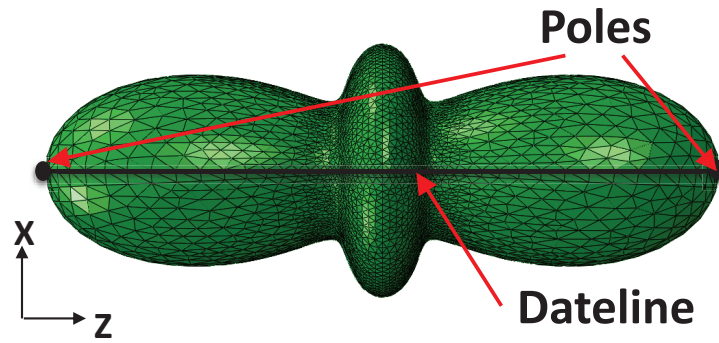
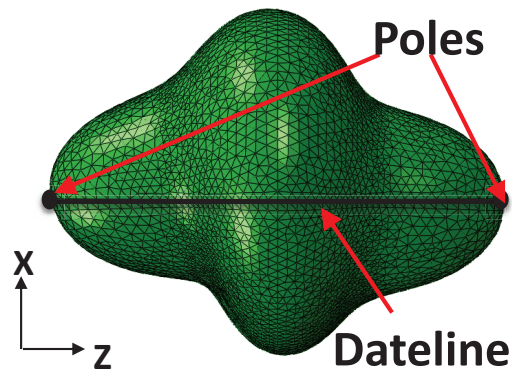


Figure 1.7: (a)-(f) six representative examples of the artificially generated symmetric spherical harmonic shapes and (g)-(l) six representative examples of the artificially generated asymmetric spherical harmonic shapes.



(a)



(b)

Figure 1.8: Representative examples of (a) a symmetric and (b) an asymmetric shape used for the artificially generated shape test cases with the harmonic topological mapping poles and date lines labeled.

the date line corresponded to $\phi = 0$. Fig. 1.8 shows two representative examples of the artificially generated shapes with the poles and date lines indicated.

To analyze the capabilities of the proposed techniques, sets of shapes were randomly generated, parameterized using the two-step harmonic mapping (Section 2.4.2), and then decomposed to identify the fundamental shape modes using POD (Section 2.4.4). For these tests the translation function (i.e., $\vec{x}(\theta, \phi)$ in Equation (3.11)) was taken as the mean of the dataset, which is a common assumption particularly when translation has minimal physical meaning for the datasets. In addition, as a control test for comparison purposes principal component analysis (PCA) was applied to the sets of vectors of spherical harmonic coefficients (α_j) that were used to generate the shapes. Again, note that the monikers POD and PCA can be used interchangeably in many cases. However, for clarity here POD will be used to refer to the decomposition of the shape sets in terms of the continuous function representation obtained from the harmonic mapping (Equation (3.2)), while PCA will be used to refer to the decomposition of the shape sets in terms of the coefficients of the spherical harmonic functions used to generate them (i.e., discrete vectors of coefficients). In some sense the PCA analysis is related to the best possible results that could be obtained by an existing class of shape analysis method such as SPHARM [34] (if the shapes were able to be considered without noise and with no required mapping step).

Initially, the mode shapes, and in particular, the eigenvalue (i.e., energy) spectrum obtained from both the proposed framework and the control test were compared to examine the nature of the patterns within the datasets. For both symmetric and asymmetric cases, three trials were performed with 10, 20, and 30 shapes in turn, and each trial was repeated five times to show the consistency. Lastly, the ability to use the POD modes from the proposed framework to classify the datasets was tested in comparison to the spherical harmonic coefficient vectors used to generate them (the control test for this comparison case). K-means clustering [26] was used to group the shape sets into two groups, and then the sets were divided into a training and a testing set. Fisher’s Linear Discriminant Analysis (FLDA) [26] was used to build classifiers with the training sets, and the rate of classification was calculated for both the testing and training sets. Note that the rate of classification of the training set can be considered a measure of separability. 10 testing shapes were used in all

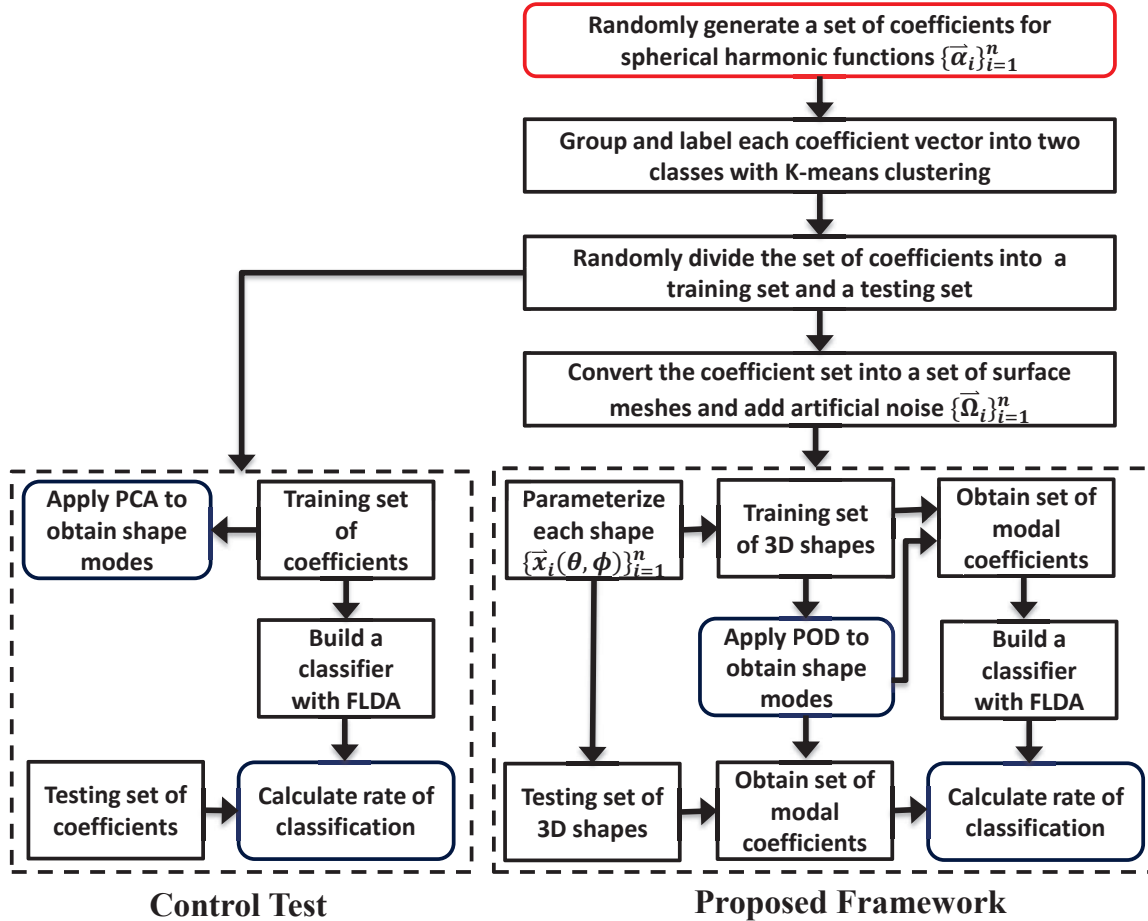


Figure 1.9: Schematic of the analysis procedure to assess the pattern recognition capabilities of the proposed approach. The PCA modes from the Control Test were compared to the POD modes from the Proposed Framework and the rate of classification using the spherical harmonic coefficients from the Control Test was compared to the rate of classification using the POD modal coefficients from the Proposed Framework.

cases, and three trials were performed with 10, 20, and 30 training sets in turn, with 2-fold, 3-fold, and 4-fold cross-validation, respectively. Again, to test consistency each trial was repeated three times, and the shapes were randomly selected each time from the datasets for the cross-validation procedure. Note that since the PCA and the spherical harmonic classification were applied directly to the coefficients used to generate the data, they are actually noise free in comparison to the proposed techniques which were applied to the shapes with additive noise. Therefore, the comparisons presented also display the tolerance of the proposed techniques to noise. Fig. 1.9 shows a schematic of the comparative analysis procedure for the artificially generated shape sets.

1.4.2.1 Results and Discussion: Fig. 1.10 shows representative examples of the modes (only from the symmetric cases for brevity) and Table 1.1 shows the mean and standard deviation of the relative mode energy (i.e., corresponding eigenvalue divided by the sum of all eigenvalues in the set) for the first three modes for the symmetric test cases and the first five modes for the asymmetric test cases obtained from both the proposed approach with POD and the control test with PCA applied to the spherical harmonic coefficients directly.

For both the control and the proposed framework, the first three modes for the symmetric tests and the first five modes for the asymmetric tests captured over 99% of the total energy in the systems in all cases. This is significant in that the approach presented for mapping and decomposing the shapes (without any referential information between shapes other than the poles and date line) was capable of recovering a pattern of the same order as that which was built into the datasets with the spherical harmonic coefficients. Moreover, the distribution of energy across the three modes was nearly identical for the results of the proposed approach compared to the control tests, which further confirms that the proposed techniques recovered an appropriate set of fundamental features. The modes themselves are similar between the two approaches, but also clearly different (similarly for the asymmetric cases). This is not unexpected, particularly since the spherical harmonic basis functions are orthogonal to one another in the spherical coordinates, and therefore any linear combination of these functions could be a suitable basis. The fact that the order and distribution of the pattern is consistent between the two approaches is considered to be a far more significant result.

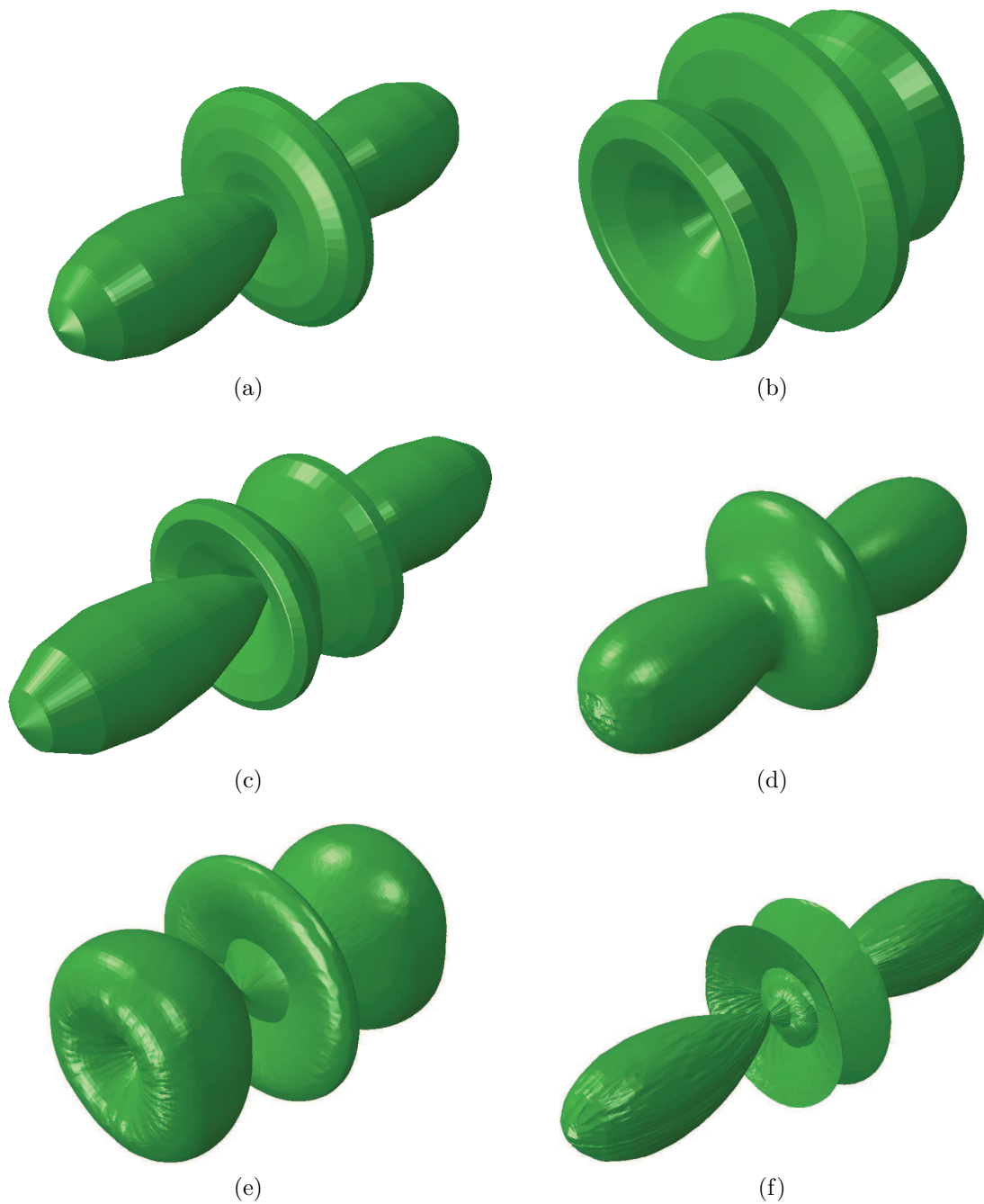


Figure 1.10: Example of (a) mode 1, (b) mode 2, and (c) mode 3 obtained from PCA of the spherical harmonic coefficients (i.e., control test), and (d) mode 1, (e) mode 2, and (f) mode 3 obtained from POD with the proposed framework for the symmetric shape test cases.

Table 1.1: Mean (μ) and standard deviation (σ) of the relative mode energy percentage for training set sizes of 10, 20, and 30 shapes obtained from PCA of the spherical harmonic coefficients (Control) and obtained from POD with the proposed framework (Proposed).

		10		20		30	
Mode #		Control	Proposed	Control	Proposed	Control	Proposed
Symmetric							
1	μ	64.3	68.8	55.8	63.3	59.4	65.9
	σ	0.04	0.05	0.05	0.05	0.08	0.04
2	μ	30.7	26.5	34.9	29.5	32.2	28.1
	σ	0.04	0.05	0.06	0.05	0.07	0.03
3	μ	5.1	3.4	9.3	5.6	8.4	4.5
	σ	0.03	0.01	0.02	0.01	0.02	0.01
Asymmetric							
1	μ	87.9	84.6	88.4	84.4	91.4	87.1
	σ	0.07	0.07	0.04	0.05	0.01	0.02
2	μ	5.1	7.0	3.9	5.0	2.7	5.2
	σ	0.03	0.03	0.01	0.02	0	0.01
3	μ	3.0	3.7	3.1	3.9	2.0	2.6
	σ	0.02	0.02	0.01	0.01	0	0
4	μ	2.1	2.5	2.2	2.8	1.7	1.9
	σ	0.01	0.01	0.01	0.01	0	0
5	μ	1.2	1.3	1.4	2.0	1.3	1.4
	σ	0.01	0.01	0.01	0.01	0	0

Lastly, Table 1.2 shows the classification results from FLDA with the spherical harmonic coefficients compared to the first three (for the symmetric trials) or first five (for the asymmetric trials) POD modal coefficients from the proposed framework. Note that the POD coefficients are obtained by mapping the shapes and then projecting each mapped shape onto the corresponding POD mode. In general all test cases maintained a high rate of classification, and most importantly the classification rates were in good agreement between the two approaches. As such, the methods presented for mapping and decomposing a set of 3-D closed surfaces were capable of obtaining sets of fundamental features representing the pattern inherent in the shape sets that could be used to build accurate classifiers and classify new datasets on par with the original basis used to generate the datasets. Furthermore, these methods were shown to be tolerant to both noise and the size of the datasets analyzed.

1.5 CONCLUSIONS

An approach for the quantitative analysis and statistical decomposition of sets of 3D genus-0 shapes that combines a modified harmonic mapping approach directly with proper orthogonal decomposition was presented. The approach was shown to have a straightforward implementation, and to be particularly well suited for applications in medical image analysis in which at least one clearly identifiable anatomical reference line can be determined, and thus the approach can be uniquely anatomically consistent with minimal methodological uncertainty. Through an example of the analysis of a human right ventricle endocardial surface, the methods were shown to provide unique features of shape change of an anatomical shape dependent upon the chosen anatomical reference features, the methods were tolerant to variations in the surface description and verifiable through standard convergence processes, and the methods were tolerant to reasonable errors in segmentation and feature selection. Then, through the analysis of artificially generated shape sets the approach was shown to be capable of recovering shape features for classifying shape clusters on par with the inherent (i.e., built-in) patterns with no *a priori* assumption of the shape structure beyond a single reference line on each surface and in the presence of additive noise.

Table 1.2: Mean (μ) and standard deviation (σ) of the rate of classification percentage for the training and testing sets for the spherical harmonic coefficients (Control) and the modal coefficients from POD with the proposed framework (Proposed) for training set sizes of 10, 20, and 30 shapes.

		10		20		30	
		Control	Proposed	Control	Proposed	Control	Proposed
Symmetric							
Train	μ	93.3	86.7	94.4	95.6	93.3	86.7
	σ	14.9	12.5	15.7	4.4	14.9	12.5
Test	μ	96.7	91.7	94.4	93.3	96.7	91.7
	σ	7.5	6.9	15.7	12.5	7.5	6.9
Asymmetric							
Train	μ	100	100	99.4	99.4	98.3	98.9
	σ	0	0	1.6	1.6	2.6	1.6
Test	μ	95.0	93.3	92.2	94.4	98.3	99.2
	σ	7.6	7.5	10.3	6.9	3.7	2.8

2.0 A NEW APPROACH TO KINEMATIC FEATURE EXTRACTION FROM THE HUMAN RIGHT VENTRICLE FOR CLASSIFICATION OF HYPERTENSION: A FEASIBILITY STUDY

2.1 ABSTRACT

This work presents a novel approach to analyze the function of the human right ventricle by deriving kinematic features of the relative change in shape throughout the cardiac cycle. The approach is anatomically consistent, allows direct comparison across populations of individuals, and potentially provides new metrics to improve the diagnosis and understanding of cardiovascular diseases such as pulmonary hypertension. The details of the approach are presented, which includes a variation of harmonic topological mapping and proper orthogonal decomposition techniques, with particular focus on their applicability with respect to untagged cardiac imaging data. Results are shown for the decomposition of a collection of clinically obtained human right ventricle endocardial surfaces segmented from cardiac computed tomography imaging into the fundamental shape change features for individuals both with and without pulmonary hypertension. The features are shown to be consistent and converging towards intrinsically physiological components for the heart, and may potentially represent a new set of features for classifying the progressive change in right ventricle function caused by pulmonary hypertension, particularly in comparison to traditional clinical metrics.

2.2 INTRODUCTION

Pulmonary hypertension (PH) is a cardio-pulmonary illness affecting all ages and racial populations that is clinically characterized by a hemodynamic state of elevated mean pulmonary arterial pressure [45, 73, 81]. Untreated PH is a devastating disease with poor long-term prognosis, regardless of etiology. Estimated median survival following the onset of symptoms was reported in 1991 to be 2.8 years [22]. With early detection treatments have been found to be successful in vastly improving prognosis, but diagnosis is often delayed because the early symptoms of PH are nonspecific [45].

One particular unifying observation about PH is that the adaptation of the right ventricle (RV) under the sustained pressure overload is a major determinant of patient symptoms and, more importantly, survival [15, 92]. Previous studies have noted extensive myocardial hypertrophy, an overall increase in RV wall thickness, shape, and volume, and progressive contractile dysfunction. Furthermore, the RV with PH dilates significantly over time, becomes more concentric, and the septum flattens. Without treatment the RV will further dilate over time and eventually fail. Yet, while a connection between RV shape/function and PH clearly exists, there is still no clear understanding of why certain patients with severe PH maintain near normal cardiac outputs for long periods of time, and others experience a more rapid deterioration leading to RV failure. As such, there is a great need for noninvasive techniques to monitor and analyze the RV function throughout the course of PH.

The inherent geometric and functional complexity of the right heart has limited the number of analytical studies to-date regarding modeling and analysis of shape and deformation of the RV that go beyond the typical bulk (i.e. organ-level) hemodynamic and volumetric measures or select regional simplifications. Moreover, the standard indicators of left ventricle (LV) shape and contractile function are not applicable to examine the crescent-like shape of the RV. One early study used implanted markers and calculated the *in vivo* bulk RV volume as well as the subvolume of the outflow, midventricular, and inflow regions at several instances in the cardiac cycle of canines [76]. Evaluation revealed that the RV ejects its volume in a nonuniform spatial pattern. Subsequently, this approach was extended to analyze the regional contractile function of the RV free wall by calculating the principal shortening

or elongation of the subregions [17]. Alternatively, [74] used ECG-gated magnetic resonance imaging (MRI) and approximated the RV free wall geometry with biquadratic surface patches to then calculate the metric tensor, curvature tensor, and major and minor curvatures as a means to define/characterize the shape of the RV free wall. More recent efforts have combined computational mechanics with tagged MRI to obtain approximate deformation and strains throughout the entire RV wall during contraction [40] and even began establishing a framework for patient-specific LV and RV combined fluid-structure modeling of the cardiac cycle [98, 88]. In general, many of the approaches implemented to-date rely on invasive measurement techniques, thereby eliminating the possibility of human studies. Moreover, the methods developed thus far to analyze and contrast RV function require selection of specific (typically non-dimensional) features, such as relative volume change, mean regional curvature, etc., prior to any quantitative analysis. There is typically no direct pathological basis for the selection of these features, which may be a primary reason for the relative lack of success in quantitative analysis and prognosis of PH pathology.

In contrast to the more traditional techniques, statistical shape analysis approaches based around concepts in pattern recognition have been developed in recent years, and have thus far been most commonly applied in the medical imaging field to analyze brain or cardiac structures and pathologies [53, 100, 7, 63, 86]. Typically, these shape analysis approaches contain at least three steps: building correspondence (e.g., diffeomorphism [63] or harmonic mapping [11]), registration, and decomposition (e.g., PCA [7]). Such statistical shape analysis methods have shown the capability to automatically identify discriminating features from a set of medical images of a given population, and then be implemented for several uses, including clustering and classifying significant subgroupings within the population ([100, 7, 60]) or aiding with future image processing techniques related to segmentation [41]. One important note is that most current approaches include a step to lower the dimensionality of the shape information prior to applying pattern recognition techniques. Examples of methods that have been applied to reduce the dimensionality within a statistical shape analysis framework include projecting the 3D shapes onto an *a priori* selected set of basis functions (e.g., spherical harmonic functions [86] or spherical wavelets [100]) or converting the shapes to some type of medial representation [84].

This work presents a novel statistical shape analysis approach to decompose the relative kinematics of a collection of right ventricle endocardial surfaces from clinically obtainable cardiac images (a single patient during the cardiac cycle and/or multiple different patients) into a set of fundamental features that uniquely describe right ventricle function using topological mapping and statistical decomposition techniques. The methods maximize anatomical consistency of the analysis and preserve geometric features particularly by avoiding the use of standard registration steps and by deriving and utilizing the fundamental features directly from the data rather than requiring projection onto a predefined basis. The approach was applied to a unique clinically obtained set of cardiac computed tomography images to obtain and examine the features of shape change that can be obtained. The features obtained from this approach are shown to potentially provide a unique biometric based on the human heart. In addition, the features are shown to be consistent with respect to analysis with various groupings of individuals, implying that the features are in some sense converging as the dataset size increases to produce physiologically intrinsic features and not just artifacts of the data. Moreover, the distributions of the obtained features show promising variations that appear to be correlated to changes in hemodynamics in the least, and potentially changes in the physical and functional adaptation of the right ventricle as shown through analysis of the patient group in terms of the clinical diagnosis as pulmonary hypertensive or non-hypertensive. Section 2.3 outlines the details of the imaging data considered for this work and Section 2.4 presents the analysis methods applied. Section 4.4 presents and discusses the decomposition results, which is followed by the concluding remarks in Section 4.5.

2.3 HUMAN CARDIAC IMAGE DATASET

The present work utilized a unique clinically obtained set of ECG-gated multislice cardiac computed tomography (CT) images from a study on regional RV structural and functional adaptation to PH as previously reported in [80]. Patients were scanned within 2 days of invasive hemodynamic measurements on either a GE Lightspeed 16-slice scanner or a GE

VCT 64-slice scanner ¹. Briefly, scan parameters were as follows: kV 120; mA approximately 400 without ECG-dose modulation; rotation time $350msec$; pitch dependent on heart rate; $1.25mm$ slice thickness (for 16 detector scanner); kV 120, mA approximately 500 with ECG-dose modulation adjusted to peak at 65-80% R-R interval; rotation time $350msec$; pitch dependent on heart rate; $0.625mm$ slice thickness (for 64 detector scanner). A set of 10 patients was selected from the study, and each patient within this set of CT scans was initially classified based on mean pulmonary arterial pressure (PAP) and right atrial pressure (RAP), with six patients grouped as “non-hypertensive” based on $PAP \leq 25mm\ HG$ (labeled as N1-6) and four patients grouped as “hypertensive” with decompensated RV function based on $PAP > 25mm\ HG$ and $RAP > 10mm\ HG$ (labeled as H1-4) In all cases, patients with $RAP > 10mm\ HG$ also had a cardiac index $< 2.0L/min/m^2$. Each of the 10 patients included in the study had 10 time frames acquired over one entire cardiac cycle equally spaced temporally from end diastole to end diastole based on helical, retrospective ECG-gating during a single breath hold. An important note is that all patients within the study (even those classified as “non-hypertensive”) are symptomatic, and therefore, not an average healthy individual. The classification of “non-hypertensive” solely refers to normal resting hemodynamics. Note that the kinematic analysis for this 10 patient set was not expected or intended to provide conclusive statistical results that are now useable for diagnostic purposes. Rather, this feasibility study was intended to show the potential capability of the analysis approach to produce intrinsic kinematic features that could be used to classify pathology provided with a statistically sufficient number and composition of patients in the dataset. Furthermore, this work is subject to the limitations of clinical data acquisition, and to the authors’ knowledge there has been no other study considering a set human right ventricle reconstructions of the size, detail, and nature of the set used herein.

¹(General Electric Healthcare; Milwaukee, WI, USA)

2.4 METHODS

The analysis approach applied herein to obtain a set of kinematic features from a given set of patient images such as those described above proceeded as follows (shown graphically in Fig. 4.3) :

- Step (a) - Segment the image stacks to obtain 3D closed surfaces describing each patient's right ventricle endocardial surface (RVES) throughout a complete cardiac cycle.
- Step (b) - Smooth the 3D closed surfaces and convert the surfaces to 3D meshes suitable for numerical analysis.
- Step (c) - Topologically map each RVES to a unified (i.e., comparable) reference state using harmonic mapping.
- Step (d) - Convert the sets of shape functions into sets of relative shape change functions (i.e., pseudo-displacement functions) for each patient over a complete cardiac cycle and normalize (i.e., scale) the sets.
- Step (e) - Apply the decomposition method (i.e., proper orthogonal decomposition) to the complete set of normalized pseudo-displacement functions to determine and rank a set of kinematic features (i.e., modes and corresponding transient coefficients from decomposition).

2.4.1 Segmentation and Mesh Generation

The first and most laborious part of the process was to obtain closed, three dimensional (3D), mesh-based (i.e., a set of linearly interpolated point clouds) surface descriptions of the RV shape for each of the nine unique time frames (the last frame is the return to end diastole and was excluded to avoid redundancy) for each of the 10 individuals (90 total surfaces). For this work, the surfaces were obtained by manually segmenting the RVES from each image in the CT stacks, interpolating the slices, and then smoothing the interpolated surfaces using a standard recursive and discrete Gaussian filter within the commercial medical image processing software Simpleware². Manual segmentation was used to ensure that the

²(www.simpleware.com)

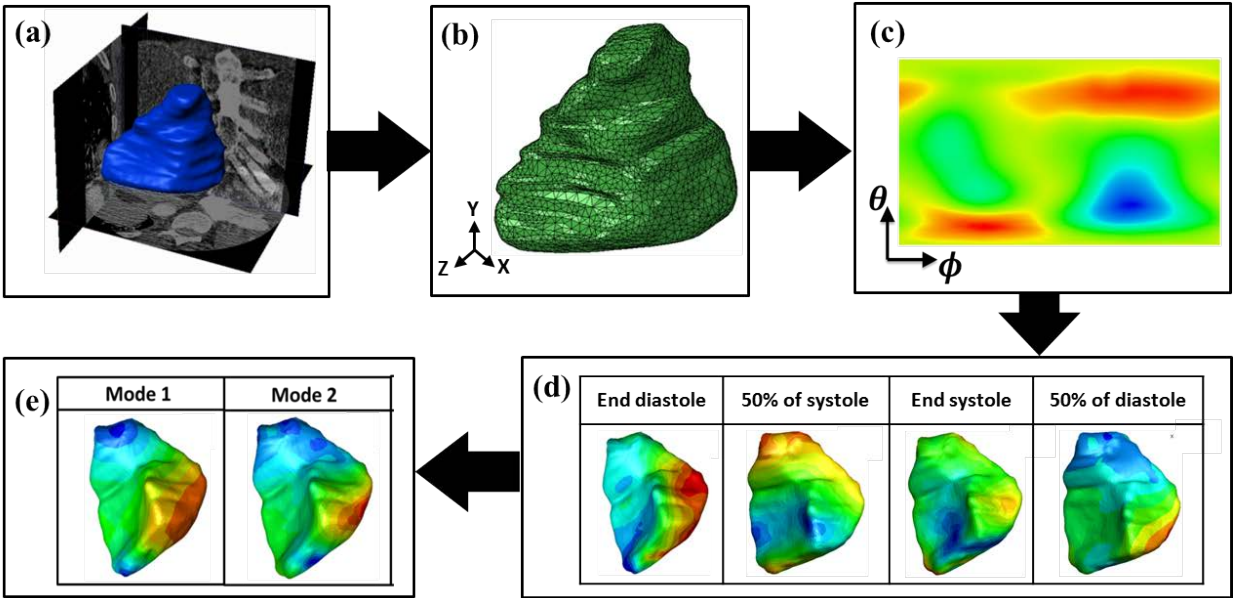


Figure 2.1: Schematic of the shape analysis framework, including (a) segmentation of the RVES from the CT images, (b) smoothing and interpolated 3D closed surface mesh generation, (c) parameterization of the RVES in terms of spherical coordinates through harmonic mapping (shown in 2D), (d) conversion of all surfaces to shape change functions, and (e) decomposition of the shape change functions into the fundamental shape change features (i.e., modes) using POD.

most anatomically accurate representations of the ventricle shape were segmented within the constraints of the CT image quality, and similarly the endocardial surface was chosen specifically due to the improved imaging contrast between the wall tissue and blood, which allows for a far more accurate segmentation of the endocardial surface in comparison to the epicardial surface. The segmentation was overseen and all segmentations were verified by a trained cardiologist (M.A. Simon), who has over 10 years of experience in advanced heart failure, pulmonary hypertension, and in particular, experience in the imaging of the RV.

2.4.2 Surface Parameterization

Each surface mesh was parameterized using a two step variation of harmonic topological mapping so that they could be quantitatively compared to one another and further analyzed. A harmonic mapping to the unit sphere is a surface parameterization method that allows for sets of arbitrary shapes to be pointwise quantitatively compared, satisfies the desired constraints for medical imaging applications, and has already been shown in several cases to provide consistently unique, one-to-one, and non-overlapping surface representations for a wide variety of genus-0 shapes (see [30, 11] for an in-depth overview of the theory and potential applications of harmonic mappings).

In brief, a harmonic mapping (i.e., change in coordinates) is simply a parameterization that satisfies Laplace’s equation for each new parameter. As such, choosing the new parameters to be the spherical coordinates, ϕ (longitude) and θ (latitude), the spherical coordinates for each point on the given surface (i.e., location on the surface of the unit sphere) can be determined from the solution of the following differential equations

$$\nabla^2\theta(\vec{x}) = 0 \text{ in } \Omega_k, \quad \nabla^2\phi(\vec{x}) = 0 \text{ in } \Omega_k, \quad (2.1)$$

where $\Omega_k \subset \mathfrak{R}^3$ is the k^{th} continuous, 3D, non-overlapping, closed surface domain (from the given set of segmented surfaces) and \vec{x} are the cartesian coordinates with respect to the origin for the given surface. Eqn.3.1 can be solved using any preferred method for the solution of partial differential equations (the standard Galerkin finite element method was used for this work [72]), but first requires suitable boundary conditions for the spherical coordinates ϕ

and θ . The approach used for the present work requires each surface to have at minimum two reference points and a reference line: a point defined as the north pole (Γ_n), a point defined as the south pole (Γ_s), and a continuous non-overlapping line defined as the date line (Γ_d) that connects the two poles. The date line has a nonunique mapped value as it represents where the longitude passes 360° . As such, the surface is cut along the date line to create two overlapping, but independent boundaries: an east date line (Γ_d) and west date line (Γ_d^o). Thus, the values of the spherical coordinates along the references will be assigned as

$$\theta = 0 \text{ on } \Gamma_n, \theta = \pi \text{ on } \Gamma_s, \phi = 0 \text{ on } \Gamma_d, \phi = 2\pi \text{ on } \Gamma_d^o. \quad (2.2)$$

An important point is that the references should correspond to anatomical features that are reliably identifiable if the results are to be anatomically consistent in any way. However, tests were performed (not shown here for brevity) in which changes to the parameterization were analyzed with respect to perturbations to the mapping references, and the parameterization process outlined herein was found to be insensitive to changes on the order of reasonably expected errors. For the RVES shapes considered here the reference data was chosen as the anterior border between the free wall and septum (i.e., date line) with endpoints at the intersection with the pulmonary valve and apex (i.e., poles), as shown in Fig. 2.2a. These anatomical reference features could be identified with relatively high consistency throughout the patient sets. Example initial parameterization results from the harmonic mapping are shown in Fig. 2.2b and Fig. 2.2c as the color contours distributed over a 3D RVES.

One additional step to the mapping process (i.e., secondary parameterization) was used here due to the fact that applying the harmonic mapping directly may lead to the surface being nonuniformly distributed in the mapped domain with a majority of the surface having ϕ and/or θ values within a relatively small range, which may cause numerical difficulties (particularly related to numerical integration) that could degrade the subsequent analysis (note, this step is not required, particularly since no downsampling or projection onto a predefined basis was used, but the step was found to provide a modest reduction in computational cost for accurate numerical integration in subsequent analysis steps). This second step relies on the observation that the harmonic parameterization of a sphere defines the relationship between a uniformly distributed spherical mesh over the unit sphere domain

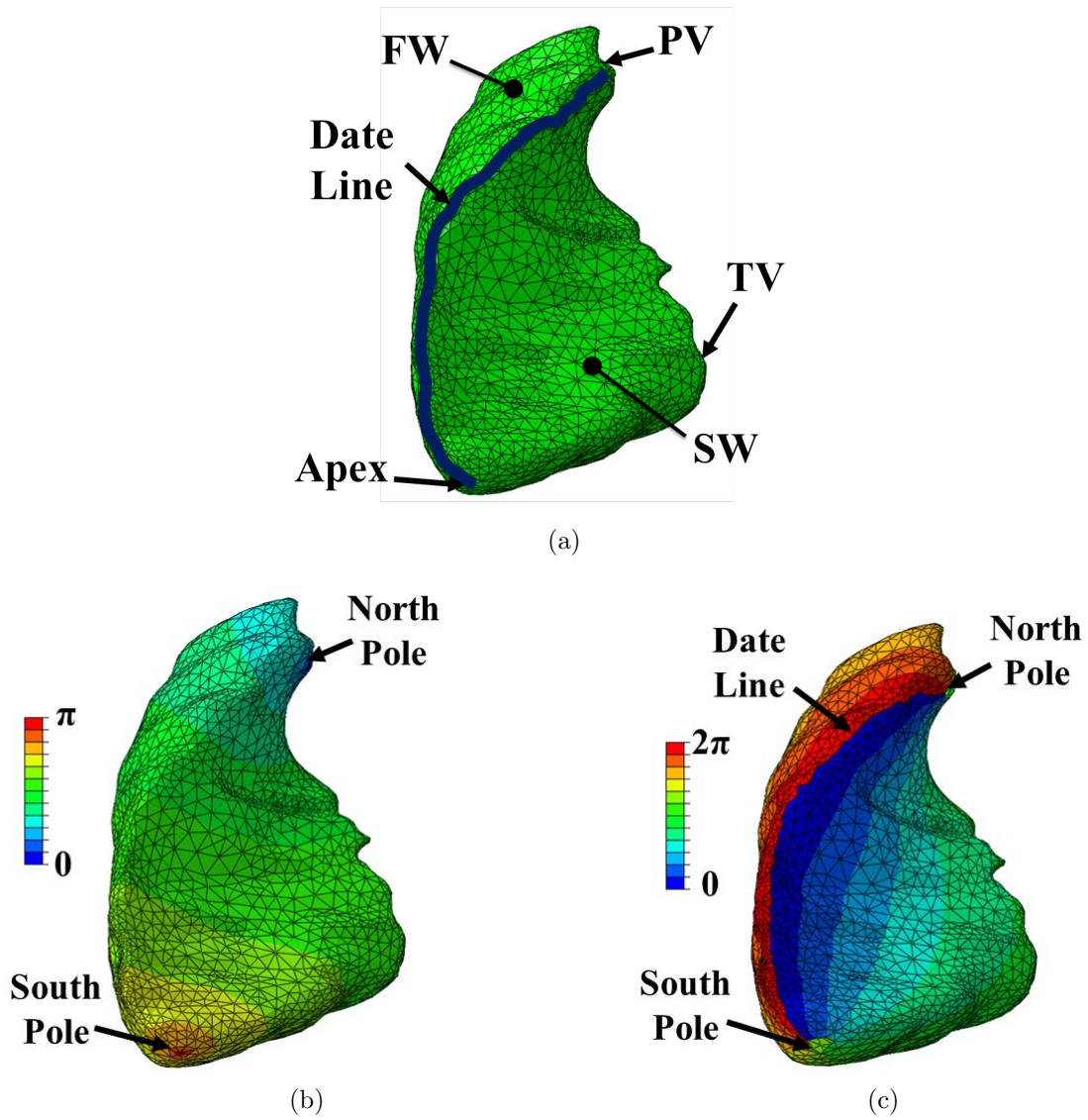


Figure 2.2: Example RVES at end diastole (a) with the free wall (FW), septal wall (SW), pulmonic valve (PV), tricuspid valve (TV), apex, and harmonic mapping reference line labeled, and (b) the latitude distribution and (c) the longitude distribution after the harmonic mapping.

(the same domain as the mapped domain) and the nonuniform distribution caused by the mapping (i.e., the solution to the partial differential equations in Eqn. 3.1), and therefore the inverse of this mapping will “undo” some amount of the distortion caused by the initial mapping process. To apply this concept the initial parameterization procedure is performed for a unit sphere as the surface (Ω) to produce the mapping

$$\vec{X}(\theta_u, \phi_u) = \vec{x}(\theta, \phi), \quad (2.3)$$

where

$$\vec{X} = [\sin(\theta_u)\cos(\phi_u), \sin(\theta_u)\sin(\phi_u), \cos(\theta_u)]^T, \quad (2.4)$$

and θ_u and ϕ_u are the latitude and longitude of the unit sphere without mapping, respectively. Eqn. 2.3 and Eqn. 2.4 can then be rearranged to produce the relationship between distorted and undistorted spherical coordinates as

$$\theta_u = \theta_u(\theta, \phi), \quad \phi_u = \phi_u(\theta, \phi). \quad (2.5)$$

Then, it is only necessary to substitute the results from the initial parameterization Eqn. 3.1 into Eqn. 2.5 to obtain the parameterization of the given surface in terms of θ_u and ϕ_u . Finally, any given surface (defined by all $\vec{x} \in \Omega_k$) can be described continuously with respect to a common domain as

$$\vec{x} = \vec{x}(\theta_u, \phi_u) \quad \text{in } \theta_u \in [0, \pi], \phi_u \in [0, 2\pi]. \quad (2.6)$$

Of particular significance is that since both the initial and secondary mappings are unique and one-to-one, the final mapping between the original surface and the unit sphere will also be unique and one-to-one. This modified approach is completely deterministic and requires minimal user-defined referential data, providing a means to analyze a set of medical images in a uniquely anatomically consistent manner. Thus, the mapped shapes can be quantitatively compared continuously over the entire surfaces in terms of the spherical coordinates to assess variations, identify patterns, etc.

2.4.3 Pseudo-Displacement Functions

A subtle but significant next step is that the set of parameterized surfaces for each patient was converted into a set of normalized relative shape change functions (i.e., pseudo-displacement functions) so that the shapes would be comparable across the entire 10-patient population. For the present work, the pseudo-displacement functions were calculated by subtracting each individual’s mapped end diastole surface from every other mapped surface of the same individual over the cardiac cycle as

$$\vec{d}_k^i(\theta, \phi) = \vec{x}_k^i(\theta, \phi) - \vec{x}_{ed}^i(\theta, \phi), \quad \text{and} \quad k \neq ed, \quad (2.7)$$

where \vec{d}_k^i is the pseudo-displacement function for the i^{th} patient at the k^{th} timeframe in the cardiac cycle and ed is the end diastole timeframe index for the corresponding patient. Then, each shape change function was normalized (i.e., scaled) with respect to the maximum change in the cardiac cycle for the corresponding individual as

$$\vec{p}_k^i(\theta, \phi) = \frac{\vec{d}_k^i(\theta, \phi)}{\max_j \|\vec{d}_j^i(\theta, \phi)\|_{L_2}}, \quad (2.8)$$

with the norm defined for a function over the surface of the unit sphere as

$$\|\vec{d}(\theta, \phi)\|_{L_2}^2 = \int_0^{2\pi} \int_0^\pi \vec{d}(\theta, \phi) \cdot \vec{d}(\theta, \phi) \sin(\theta) d\theta d\phi. \quad (2.9)$$

Therefore, each patient was reduced to being described by eight normalized pseudo displacement functions over the cardiac cycle (i.e., one shape per patient was lost from the dataset in order to make all patients comparable).

Provided with a consistently identifiable timeframe, which was the case for the end diastole timeframe used here, converting the shapes to normalized shape change is sufficient to make the datasets consistently comparable across the population of individuals. Most importantly, this approach circumvents the need for costly and nonunique traditional registration methods beyond the normalization (i.e., scaling). It should also be emphasized that the pseudo-displacement functions are kinematic functions relative to the mapping parameters (i.e., dateline and poles), since tagging or dense feature tracking to obtain an approximate “true” displacement field are not practically employable for clinical data of the nature used

herein (note that cardiac CT is the current standard of care for the evaluation of patients with known or suspected PH due to its superior imaging of the lung parenchyma in addition to the vasculature). Furthermore, it is assumed that throughout the image acquisition process that any displacement induced by respiration or body movement is negligible in comparison to the motion caused by the beating of the heart.

2.4.4 Pseudo-Displacement Decomposition

Lastly, the method of POD [6, 12, 5] (in some instances interchangeably referred to as principal component analysis or Karhunen-Loeve transform) was applied to obtain and rank the fundamental features of shape change from the compiled set of normalized pseudo-displacement functions (80 total functions). In general, the main objective of the linear form of POD is to identify the m basis functions (i.e., modes or features) $\{\vec{v}_i(\theta, \phi)\}_{i=1}^m$ that are optimal in the average sense for representing the given set of n pseudodisplacement functions (i.e., set of snapshots) $\{\vec{p}_k(\theta, \phi)\}_{k=1}^n$, which can be written as

$$\vec{p}_k(\theta, \phi) = \sum_{i=1}^m a_{ki} \vec{v}_i(\theta, \phi), \quad (2.10)$$

where a_{ki} is the coefficient that best approximates the k^{th} pseudodisplacement function with the i^{th} mode.

Defining the optimal basis as that which minimizes the average of the L_2 -norm of the difference between each snapshot and the best approximation of the snapshot, and through several manipulations including applying the method of snapshots, the optimal modes can be solved deterministically through the following eigenvalue problem (see[5] and the references therein for additional details)

$$\frac{1}{n} \sum_{k=1}^n A_{jk} C_k^{(i)} = \lambda^{(i)} C_j^{(i)}, \quad (2.11)$$

where

$$A_{jk} = \int_0^{2\pi} \int_0^\pi \vec{p}_j(\theta, \phi) \cdot \vec{p}_k(\theta, \phi) \sin(\theta) d\theta d\phi, \quad (2.12)$$

and

$$C_k^{(i)} = \int_0^{2\pi} \int_0^\pi \vec{p}_k(\theta, \phi) \cdot \vec{v}_i \sin(\theta) d\theta d\phi. \quad (2.13)$$

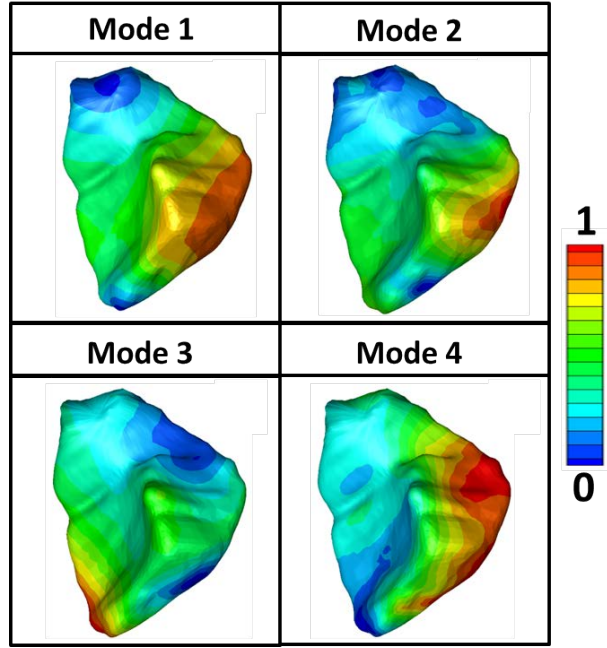
The n -dimensional eigenvalue problem can then be solved to obtain at most n modes as

$$\vec{v}_i(\theta, \phi) = \frac{1}{\lambda^{(i)}_n} \sum_{k=1}^n \vec{p}_k(\theta, \phi) C_k^{(i)}. \quad (2.14)$$

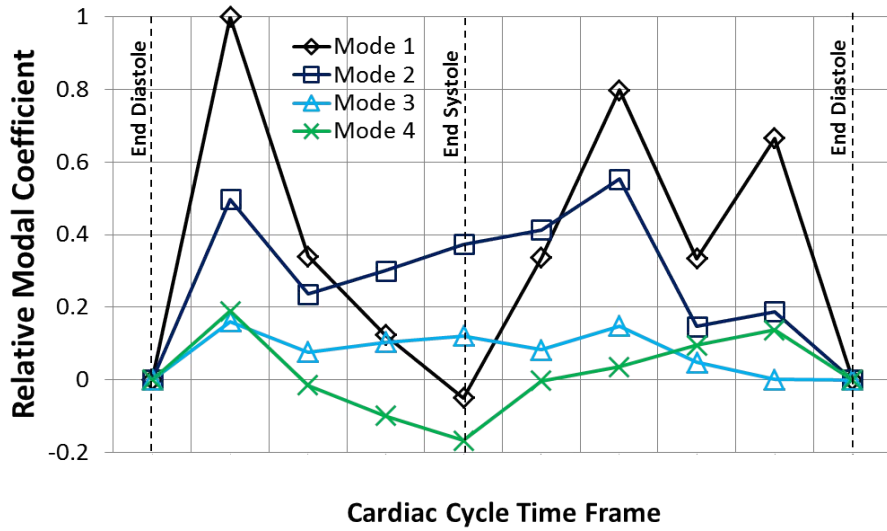
Note that the corresponding eigenvalues determined for each feature relate to the relative importance of each mode (i.e., modal energy [6]), with the larger eigenvalues corresponding to modes that are more significantly representative of the dataset. As an added benefit, the lowest eigenvalues (i.e., lowest energy modes) are typically associated with noise, allowing for spurious components to be identified and ultimately removed. For the present work, noise could be physically represented by relatively high-frequency spatial oscillations on the segmented surfaces caused by imaging/segmentation errors. For classification purposes the highest energy modes are chosen and the coefficients of these modes for each surface in the set, which are obtained by projecting the surface onto each mode, are used to define the surfaces.

2.5 RESULTS AND DISCUSSION

Fig. 2.3a shows the first four pseudo-displacement modes (i.e., $\vec{v}_1(\theta, \phi)$, $\vec{v}_2(\theta, \phi)$, $\vec{v}_3(\theta, \phi)$, and $\vec{v}_4(\theta, \phi)$) from the decomposition of the 10 patient set (80 total shape change functions), ranked from highest energy (i.e., largest corresponding relative eigenvalue) to lowest, with the magnitude of the shape change plotted on the end diastole surface for a representative patient from the dataset (N4). These first four modes captured approximately 91% of the total modal energy (i.e., sum of the first four corresponding eigenvalues relative to the total eigenvalue sum of the set). Additionally, Fig. 2.3b shows the relative values of the modal coefficients (i.e., each mode projected onto the corresponding shape change function normalized by the maximum coefficient value) of the first four shape change modes throughout the cardiac cycle for the patient. Of initial interest is that the modes and modal coefficients can provide some physical interpretations relating to the localization and sequencing of the most prevalent shape changes throughout the population and over the cardiac cycle. For example, Mode 1 appears to represent a relatively broad dilation or contraction of the free wall with the



(a)



(b)

Figure 2.3: (a) The first four shape change modes from decomposition of the 10 patient set plotted on the end diastole shape (color contours are magnitude of shape change) and (b) the corresponding relative modal coefficients over the cardiac cycle for N4.

pulmonary valve and apex moving less, while Mode 2 shows a more localized change in the free wall, and Mode 3 shows very little motion in the free wall and a more significant change in the apex region. Although, as was discussed in Section 2.4.2, the resulting mappings and therefore decompositions will depend upon the choice of the mapping references (date line and poles shown in Fig. 2.2), and the interpretation of the modal behaviors must be acknowledged to be relative to the reference point selections as well as the specific restrictions of POD (e.g., the modes must be orthogonal). In other words, the results display the most significant orthogonal features of shape change relative to the anterior border between the septal and free walls from the pulmonary valve to the apex. However, while relative in the sense of the kinematic interpretation, since the chosen anatomical reference data can be selected with confidence for the images obtained, the approach has the substantial benefit of being reliably anatomically consistent (i.e., uniquely anatomically meaningful). Moreover, the anatomical consistency is further reinforced by analyzing the change in shape (rather than just shape), and thereby avoiding additional uncertainty that could be caused by registration processes.

An additional observation is that the modal coefficients over the cardiac cycle generally followed a significantly different pattern for each individual patient regardless of the pathological state, as shown for the first mode with respect to a representative collection of patients in Fig. 2.4. This point is highlighted further when considering Fig. 2.5, which shows the relative volume change over the cardiac cycle (as calculated from the segmentations and normalized by the maximum volume for each individual) for the same set of patients. In contrast to the modal coefficients, the volume change follows an easily observed and consistent pattern over the cardiac cycle, albeit with some clear variations in rate and total volume change between the patients. There was also no apparent correlation between the volume change and any single mode's contribution over the cardiac cycle, implying a considerable difference in content relating to RV function contained within these new metrics than could be derived from a standard volume measure. Moreover, the vast difference in modal behavior over the cardiac cycle across the population would seem to imply that the response of the kinematic features obtained from the proposed approach may have the potential to provide a new and unique biometric. While this observation is intriguing, there is some concern

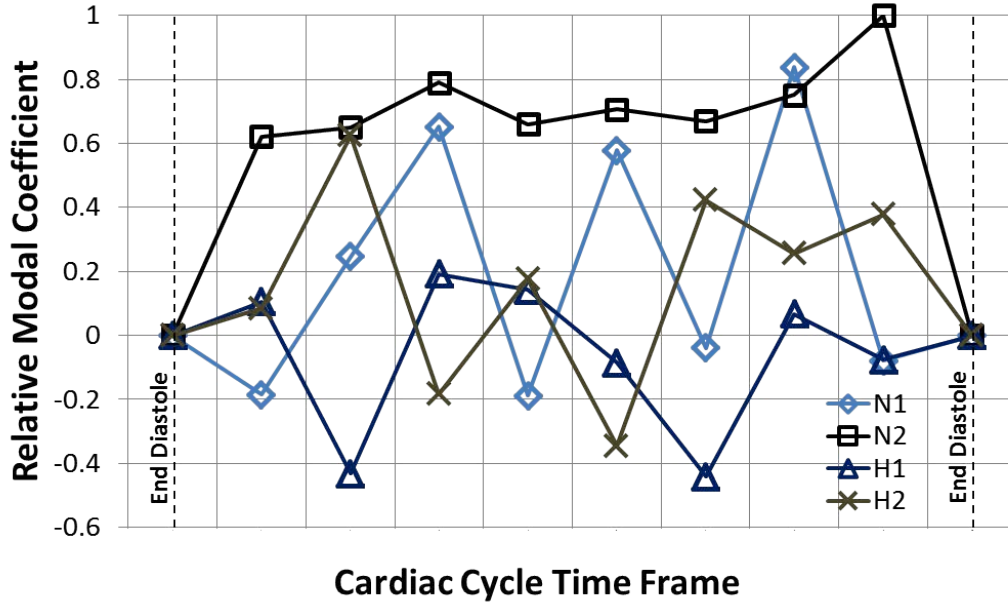


Figure 2.4: Relative modal coefficients for the first shape change mode for the first two non-hypertensive (N1 and N2) and hypertensive (H1 and H2) patients over the cardiac cycle.

that if the response of the kinematic features obtained is unique to the individual then there will be minimum potential to be used as a diagnostic device. Yet, the hope is that these modal responses are analogous to ECG signals, another measure of heart function that has been shown to be a biometric and also have diagnostic use [99], and the potential for this is encouraged strongly by the results presented in the following Section 2.5.2.

2.5.1 Feature Convergence

An important question regarding the utility of the modal analysis presented above, but prior to considering the classification potential, is whether the decomposition results, and more importantly, the approach to obtain the decomposition results are showing potential to produce features that are intrinsic to the physiology or are simply a function of the dataset analyzed (i.e., are the modes representative of the human heart, or only representative of the specific 10 hearts analyzed as a group). Furthermore, while clinically and in terms of

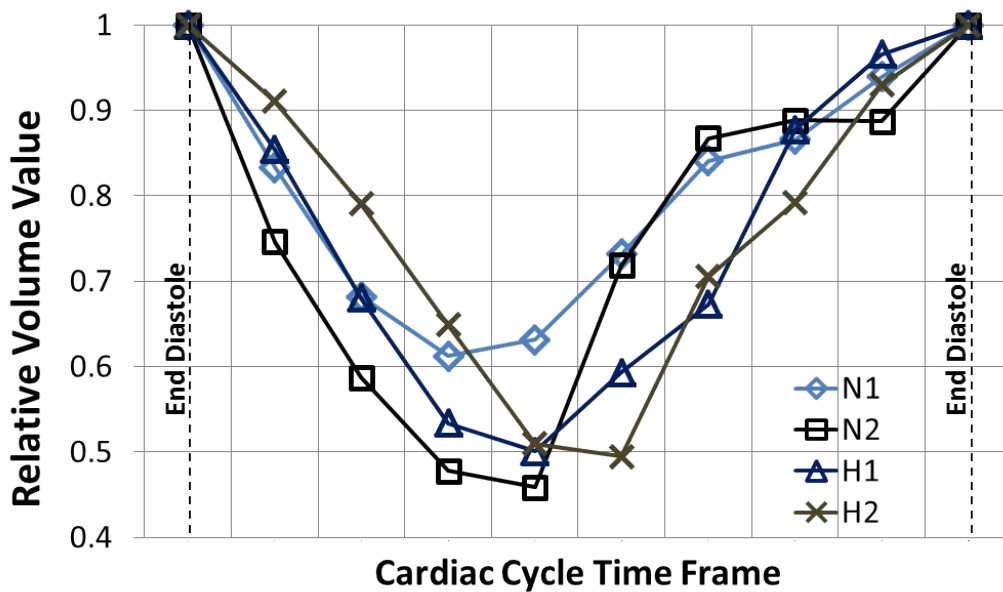


Figure 2.5: Relative volume enclosed by the right ventricle endocardial surface for the first two non-hypertensive (N1 and N2) and hypertensive (H1 and H2) patients over the cardiac cycle.

the image processing expense the 10 patient set used herein is substantial and sufficient for this initial proof of concept, statistically 10 patients is unlikely sufficient to draw concrete generalizations relating to the physiological potential. However, an aspect of the potential to use the proposed analysis method to obtain a stable physiologically intrinsic set of features was examined by studying the change in modal results with respect to the number of patients included (i.e., grouped) in the mapping and decomposition analysis. Several analyses were conducted with different combinations of the patients within the set, with the smallest analysis group being a single patient individually over the cardiac cycle, to see if the decomposition results are showing signs of convergence with an increasing number of patients.

Representative examples are shown here of the analysis of a single non-hypertensive individual (8 total shape change functions), a single hypertensive individual, all four hypertensive individuals (32 total shape change functions), and all six non-hypertensive individuals (48 total shape change functions), in comparison to the results from the analysis of the complete set (80 total shape change functions). Note that other combinations were tested, but those presented agree with the overall pattern observed. In general, the highest energy modes showed a high level of consistency. As shown with the modal distributions in Fig. 2.6 and even more clearly in the modal coefficients over the cardiac cycle in Fig. 2.7, the highest energy mode for the whole set (Mode 1) was remarkably consistent. There is little change in the appearance of Mode 1, even going from the decomposition of the single patient N1 all the way to the complete set of 10 patients (Fig. 2.6), and the differences in the coefficient distributions are negligible (Fig. 2.7a). Mode 2 showed less consistency than Mode 1, but still appeared to be converging and was highly consistent for many of the patients, particularly the hypertensive patients which generally had higher Mode 2 contributions, as can be most readily seen through the coefficient distributions (Fig. 2.7b). This pattern continued with Mode 3 and Mode 4 (Fig. 2.6), which showed some tendency towards convergence, but required larger patient groupings before any convergence were seen. Not surprisingly, the lower energy modes, especially those likely related to noise, never appeared to converge within the set of 10 patients. Moreover, the hypertensive patients overall showed a lower degree of consistency than the non-hypertensive patients, which is justified by the observa-

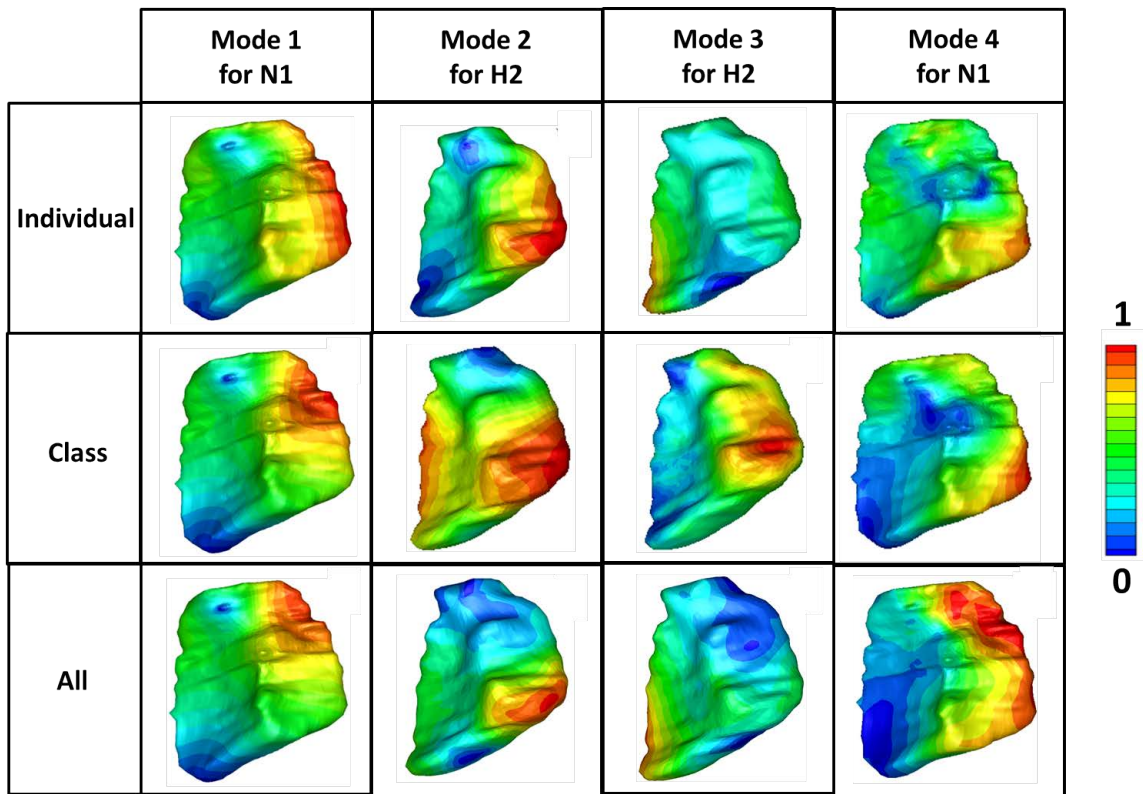
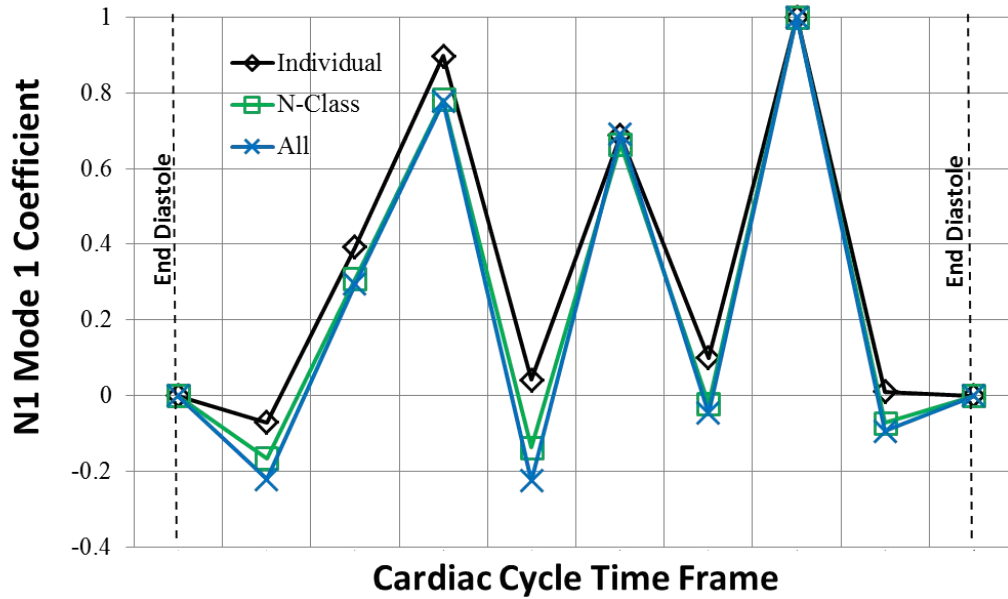
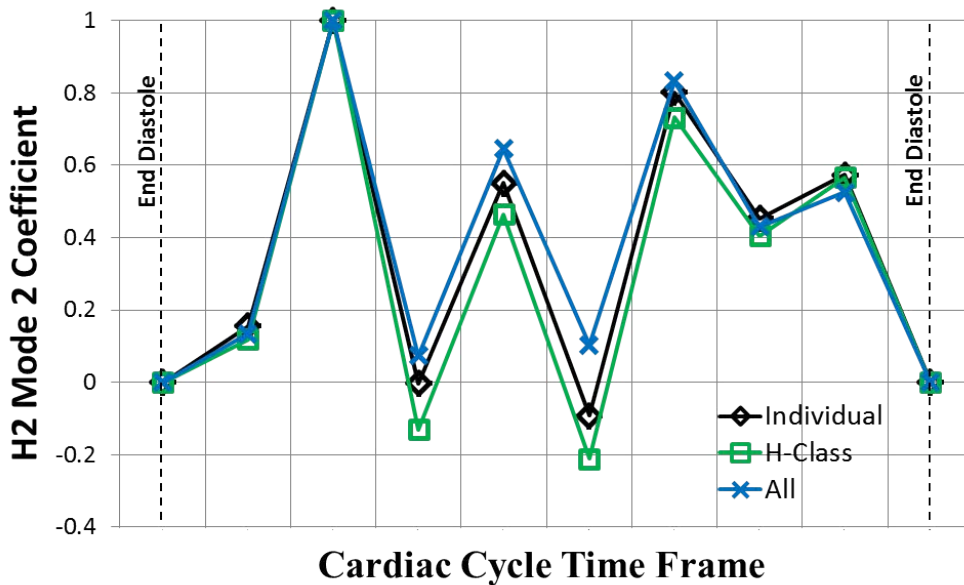


Figure 2.6: Mode 1 for N1, Mode 2 for H2, Mode 3 for H2, and Mode 4 for N1 from the decomposition of the respective individual, respective hemodynamic class (either all N or all H), and all 10 patients included in the decomposition process (color contours are magnitude of shape change).



(a)



(b)

Figure 2.7: Relative modal coefficients over the cardiac cycle for (a) the highest energy mode for N1 (Mode 1 from the full 10 patient group) and (b) the highest energy mode for H2 (Mode 2 from the full group) from the decomposition of the respective individual, respective hemodynamic class (either all N or all H), and all 10 patients included in the decomposition process.

tion that the overall pattern in the shape change for the hypertensive individuals was more complicated (i.e., of a higher order) than that occurring in the non-hypertensive patients (discussed in more detail in Section 2.5.2). However, even though there was variation when considering small groups of patients, as the patient number was increased the hypertensive patients also appeared to be converging to unique and stable features for the high energy modes.

2.5.2 Relationship to Pulmonary Hypertension/Classification Potential

As discussed previously, the size of the dataset is not large enough to build and test classifiers using the features obtained from the decomposition in relation to pulmonary hypertension. However, the following analysis was intended to show the potential for identifying a relationship between the kinematic features and the state of hypertension, and thus the feasibility of the proposed approach to lead toward a diagnostic classifier.

Two approaches were considered to analyze and group the patients based on the pseudo-displacement modal responses of the individuals and were compared to the classification based on the standard hemodynamic measures. In both cases, the total energy (i.e., coefficient summation) of the modes over the cardiac cycle was analyzed, rather than the time sequencing of the modal coefficients which was observed above to be unique for each patient and potentially a biometric. For the first approach the first three modes (i.e., the three modes with the largest contribution to the shape change functions on average over the entire patient set) were chosen, which contained 84% of the total modal energy in the 10 patient set, and each patient was defined by the vector (\vec{q}) of each of the three modes' coefficients over the cardiac cycle for that patient (i.e., all eight coefficients for the corresponding mode) squared and summed as

$$\vec{q} = [(\sum_{k=1}^8 a_{k1}^2)^{\frac{1}{2}}, (\sum_{k=1}^8 a_{k2}^2)^{\frac{1}{2}}, (\sum_{k=1}^8 a_{k3}^2)^{\frac{1}{2}}]^T, \quad (2.15)$$

where a_{kj} is the modal coefficient (i.e., projection of the mode onto the shape change function) for the k^{th} time frame with the j^{th} mode for the given individual. Then, K-means unsupervised clustering was applied to the patient set in terms of \vec{q} assuming two classes to

observe the potential patient grouping. Fig. 2.8 shows the distribution of each patient in terms of \vec{q} and the groupings determined by K-means clustering. For the second analysis, the individual modal energy percentage for the i^{th} mode for each patient was calculated independently as

$$\frac{\sum_{k=1}^8 a_{ki}^2}{\sum_{j=1}^m \sum_{k=1}^8 a_{kj}^2} \times 100\%, \quad (2.16)$$

where m is the total number of modes obtained from the decomposition process of the set of 10 individuals. Fig. 2.9 shows the relative modal energy for the features needed to capture at least 99% of the total energy for each patient over their respective cardiac cycle. Note that the mode ranking/numbering (numbered starting from highest energy/eigenvalue to lowest) is based on the energy for all patients combined (80 total shape change functions). For the hemodynamic comparison, Fig. 2.10 shows the distributions of PAP and RAP for the 10 patients within the set (recall, the classification is either non-hypertensive or hypertensive with decompensated RV function). For an additional point of comparison Fig. 3.3 shows the RV ejection fraction (E_f) for each patient in the set. E_f is a standard metric that is widely used to help identify and understand functional changes in the heart, and is defined for the RV as the fraction of blood pumped out of the RV to the pulmonary circulation as

$$E_f = \frac{(V_{ED} - V_{ES})}{V_{ED}} \times 100\%, \quad (2.17)$$

where V_{ED} is the RVES volume at end diastole and V_{ES} is the volume at end systole. For reference, a range for normal human RV E_f [58] is also shown in Fig. 3.3, although it should be noted that the normal range for the RV can vary significantly and much more so than for the LV. Additionally, the normal RV E_f is generally reported as somewhat lower than that of the LV. The variability in RV E_f is notable even within patients with normal resting hemodynamics in this small sampling, as is the lack of power of this variable to discriminate between patients with normal and abnormal resting hemodynamics.

While the two approaches to analyze the modal behaviors were slightly different, the overall observations relating to the ability to use this new method to create metrics of RV function that are sensitive to the state of pulmonary hypertension were consistent. The

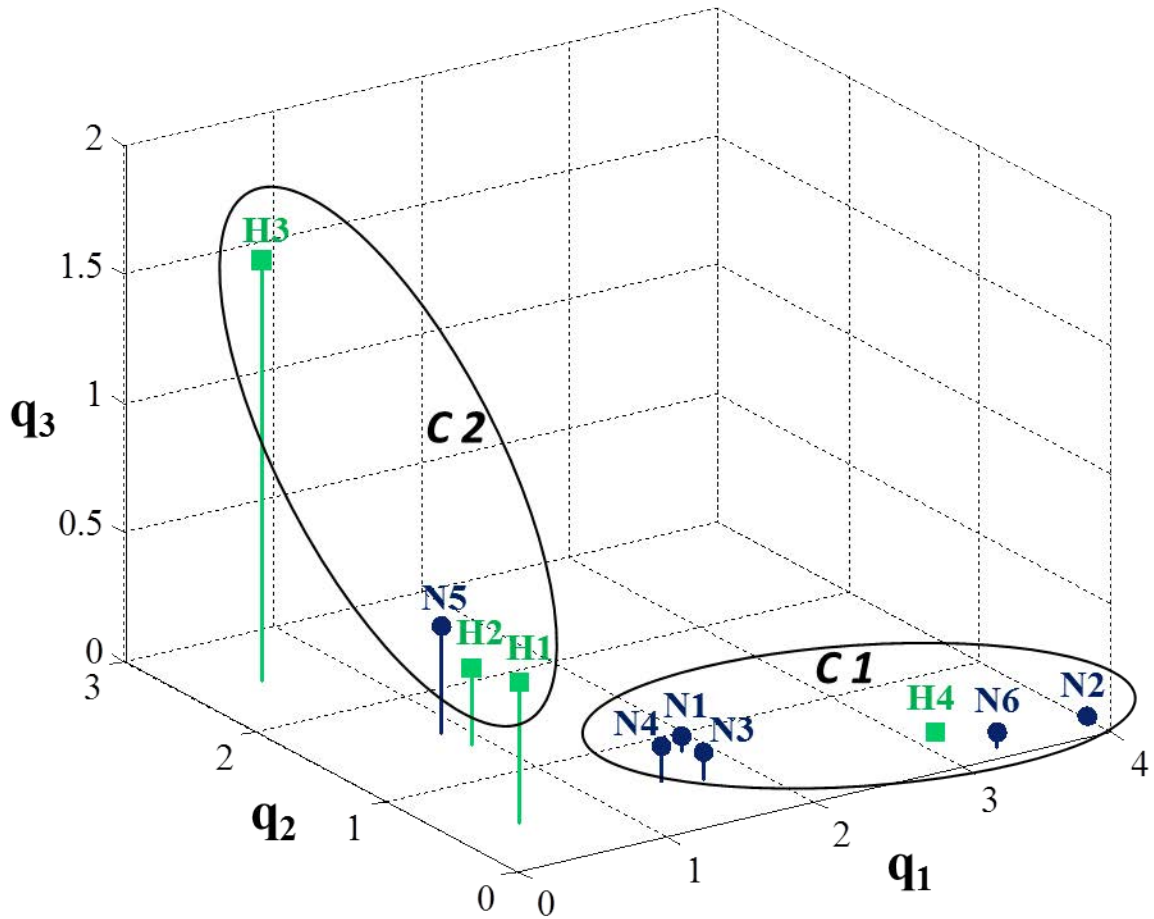


Figure 2.8: Total modal energy for the first three modes for the six non-hypertensive (N) and four hypertensive (H) patients considered for this study, and the results from K-means clustering the dataset into two groups: C1 and C2.

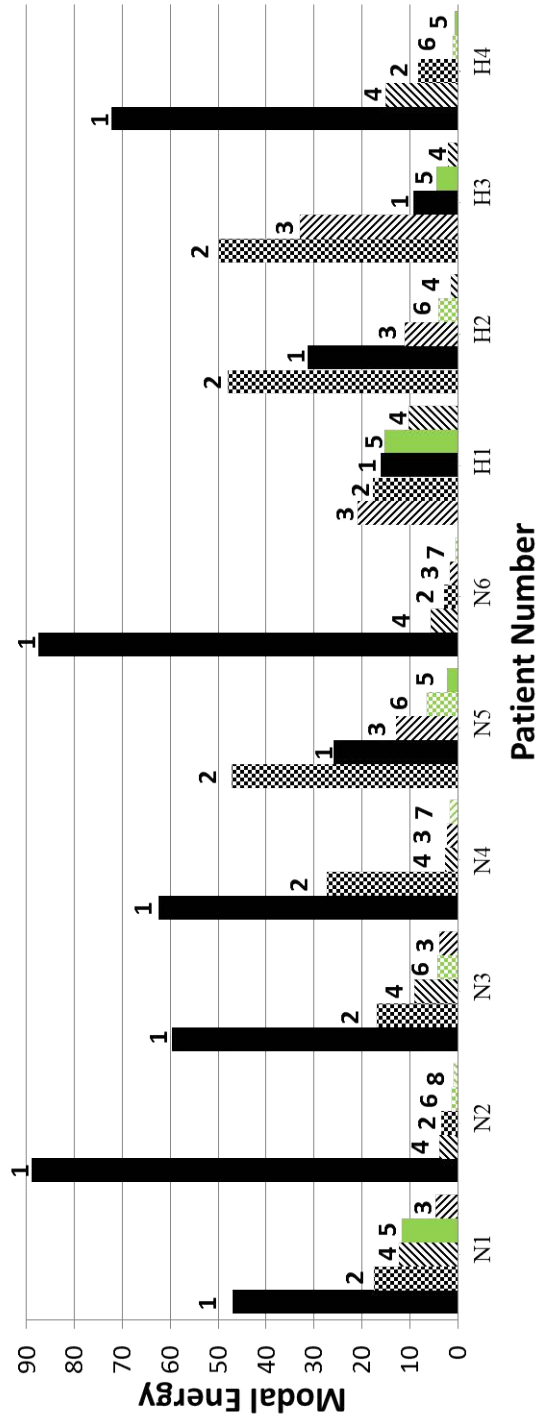


Figure 2.9: Relative modal contribution (percentage) for each of the 10 individuals for the modes necessary to capture over 99% of the total modal energy for each individual (bars are numbered and color-coded according to the corresponding mode number/ranking from the complete 10 patient set).

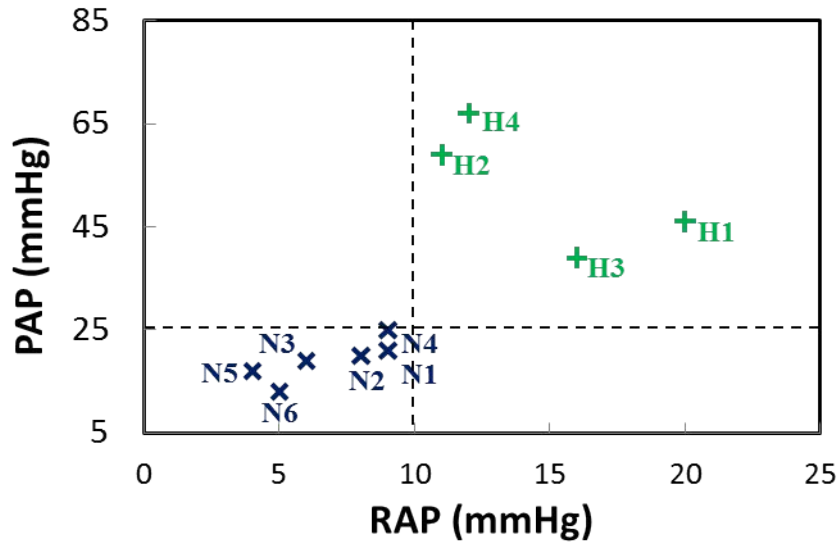


Figure 2.10: Hemodynamic distribution of the six non-hypertensive (N) and four hypertensive (H) patients consider for this study in terms of the mean pulmonary arterial pressure (PAP) and right atrial pressure (RAP).

K-means clustering (Fig. 2.8) grouped N1, N2, N3, N4, N6, and H4 in one cluster, and H1, H2, H3, and N5 in the other cluster, a grouping that appears to be reinforced by the energy distributions in Fig. 2.9 as well. Simply put, out of the 10 patients in the set one hypertensive patient (H4) was grouped with the majority of non-hypertensive patients and one non-hypertensive patient (N5) was grouped with the majority of the hypertensive patients. What is particularly interesting considering Figures 2.8, 2.9, 2.10, and 3.3 all together is that there is a distinguishable pattern forming in the modal energy distribution that differentiates the pathological states of the patient group. For instance, with the exception of the fifth non-hypertensive patient (N5), all of the non-hypertensive patients had responses that were dominated by the same global mode (Mode 1), and with the exception of the fourth hypertensive patient (H4), the hypertensive patients did not show the same Mode 1 dominance. In addition, the modal energy for the hypertensive patients was typically more evenly distributed over several modes than was the case for the non-hypertensive individuals.

There was also seemingly more variation in the modal energy distribution for the hypertensive group, but this variation is not necessarily unexpected, particularly since there is clearly a wider variation in the hemodynamics of the hypertensive group and there is quite possibly significant variations in the RV function that are not yet fully understood for these patients with severe pulmonary hypertension. Similarly, the apparent disagreement in H4 with the other hypertensive patients coincides with the fact that H4 had a considerably higher PAP and considerably lower E_f than any other patient in the group, and therefore is a clear outlier in terms of RV function. A more subtle observation is that the relative mode energy of the first and second global modes for N1, N3, and N4 is noticeably smaller than that for N2 and N6, which could potentially be related to the fact that N1, N3, and N4 have relatively high PAP and/or relatively low E_f . It is currently not possible to determine precisely what caused the difference between N5 and the rest of the non-hypertensive group, with the only observable deviation from the data presented here being that N5 had the lowest RAP in the patient group. It is certainly possible that the RV function of N5 was particularly altered by underfilling (dehydration) as compared to the others, which would correlate with the low RAP. However, an unexplained outlier here is certainly not unexpected due to the obvious lack of control with such clinical data as was used here.

2.5.3 Preprocessing Expense

One particular concern for the analysis process proposed is the preprocessing expense in terms of person-hours to segment the RV surfaces and to select the harmonic mapping features (i.e., poles and dateline) for the parameterizations. As stated, for the results presented herein all segmentation and selection of the mapping features was done manually under the guidance of a trained and experienced cardiologist specializing in advanced heart failure, pulmonary hypertension, and in particular, with experience in the imaging of the RV.

This manual segmentation required several person-hours per patient. While arguments can be made for the benefits and shortcoming of manual versus automated segmentation and/or feature tracking, based on the level of quality of the CT images used for the study, fully manual segmentation and feature selection were believed to provide the highest possible

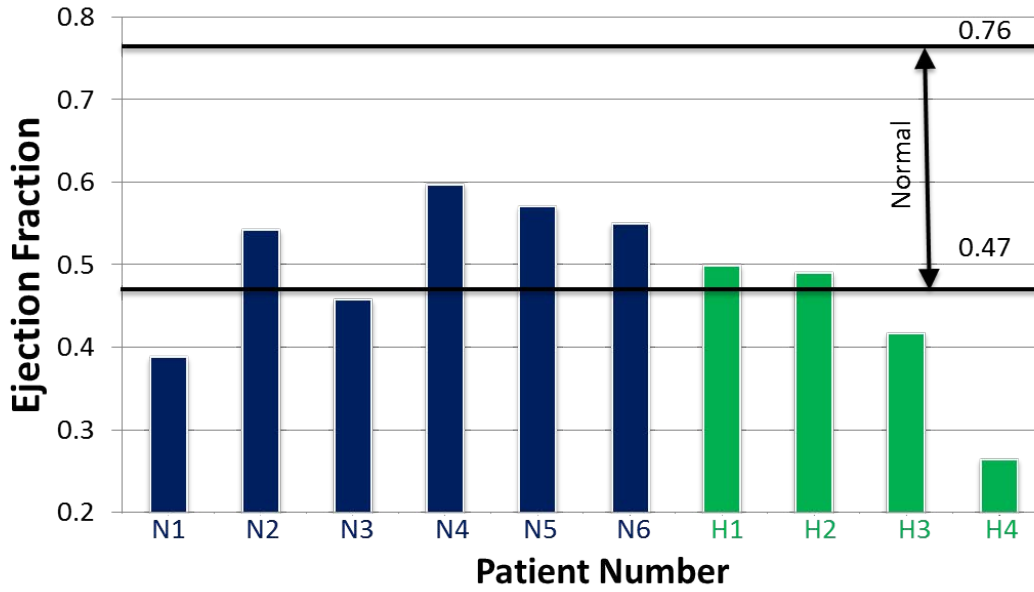


Figure 2.11: Ejection fraction of the six non-hypertensive (N) and four hypertensive (H) patients considered for this study.

level of anatomical accuracy and consistency. However, the preprocessing methods are not the focus of this work, and as long as a consistent method can be employed it is certainly possible to replace the manual segmentation with any number of the commercially available automatic or semi-automatic segmentation tools and/or to incorporate an automatic feature detection algorithm to select the mapping features regardless of imaging modality without impacting the main conclusions of this work. In fact, in the first stages of work following the completion of this current proof-of-concept, a primary effort has been to incorporate such automation to allow analysis of a much larger population of individuals in a timely fashion. Since all analyses following the preprocessing described are simply computer processing, which can be done with high computational efficiency with parallel computing no matter the population size, provided with consistent automatic or semi-automatic preprocessing the entire process can be completed automatically or semi-automatically, relatively quickly, and with no expected change to the nature of the final results.

2.6 CONCLUSIONS

An approach to obtain kinematic features of the human right ventricle based on the relative change in shape of the endocardial surface using untagged medical images, as well as a proof of concept in the use of these features in relating functional changes to pathology was presented. The approach was shown to be straightforward to implement for analysis of the right ventricle endocardial surface, and most importantly, circumvents the need for complicated registration steps and allows for anatomically consistent analysis of the functional behavior of the human heart. The features obtained showed promise to be intrinsic physiological components of the human heart, rather than just an artifact of the data, and potentially represent a new biometric derived from heart function. However, it was noted that the physical interpretations of the kinematic features are relative to the choice of anatomical reference points for the mapping process and restrictions enforced by the proper orthogonal decomposition method. In particular, the results for the patient set showed that the kinematic features of the relative shape change of the RVES over the cardiac cycle contains information that is related to the state of hypertension (i.e., pathological condition), but is not necessarily directly correlated solely to the standard hemodynamic measurements (e.g., blood pressure or ejection fraction), providing for optimism that this metric may lead to both a better understanding of RV function related to PH pathology and an improved means to diagnose the progression and potential treatment outcomes for this deadly disease.

3.0 A COMPARATIVE ANALYSIS OF GLOBAL SHAPE ANALYSIS METHODS FOR THE ASSESSMENT OF RIGHT VENTRICULAR FUNCTION

3.1 ABSTRACT

Two contemporary statistical shape analysis workflows are presented and compared with respect to analysis of human right ventricular function. The methods examined include an approach that directly applies proper orthogonal decomposition to harmonically mapped surfaces (DM-POD) and an approach that expands the harmonically mapped surfaces onto spherical harmonic functions prior to further analysis (SPHARM). The structure of both workflows is elaborated upon and compared, particularly regarding the details of several key sub-steps, including the shape parameterization, alignment, as well as statistical decomposition. The performance is evaluated for the components of each framework at the various analysis stages, as well as for the output of the complete workflows in terms of the potential to assess right ventricular function through application to a set of right ventricle endocardial surfaces captured from a clinically-obtained set of cardiac images for a group of patients with varying levels of pulmonary hypertension. Additionally, the DM-POD and SPHARM analysis approaches are examined with respect to different methods of utilizing the available imaging data by considering analysis results when incorporating several different combinations of the phases captured throughout a single cardiac cycle for the patient set.

3.2 INTRODUCTION

3.2.1 Clinical Motivation

Cardiac remodeling plays a crucial role in the progression of heart disease and the outcome of therapies, and therefore, both the static and functioning appearance of the human heart are thought to provide substantial diagnostic information relating to any number of cardiovascular diseases [19]. While a considerable amount of work over the years has focused on the function of the left ventricle (LV) and its relation to several diseases [65], recent focus has extended to the right ventricle (RV) as studies have shown a more significant dependence than previously thought of cardiac health on RV function for certain diseases, such as pulmonary hypertension (PH) [81] and Tetralogy of Fallot (TOF) [4]. For instance, the cardio-pulmonary disease PH has been commonly observed to substantially change the size and shape of the RV [81]. However, even though untreated PH is a devastating disease with poor long-term prognosis, diagnosis is often delayed because the early symptoms of PH are nonspecific [45], and there is limited understanding and available metrics that can utilize the observed RV shape and functional changes to predict the level of deterioration in heart function and/or the progression of treatments [81]. Additionally, the RV poses a particular challenge for identifying such metrics, as the RV anatomy is naturally complex, varies significantly both during the cardiac cycle and across patient populations, and often becomes even more complicated with disease. As such, creating sufficient analysis tools for developing a better clinical understanding of right heart function has generally remained a significant open challenge to-date [79].

3.2.2 Technical Background

Developments in medical imaging techniques and computer-aided diagnosis (CAD) have made significant contributions to aid physicians in both observing the nature of disease-related shape changes in biological structures and identifying diagnostic relationships between a shape change and a particular pathology [24]. Statistical shape analysis (in some instances interchangeably referred to as geometric morphometrics) is one particular CAD ap-

proach that has been shown to provide promising results for certain applications [83, 2, 82, 10]. Generally, statistical shape analysis obtains shape-based representations of a biological structure of interest from available medical images and then performs statistical analysis on a collection of these representations to study the geometrical or kinematic variations. Common aims of statistical shape analysis are to extract metrics from the given set of medical images for diagnostic purposes [53, 85, 60, 104, 95] or to obtain fundamental features to aid with future image processing [41]. In terms of applications to understanding and diagnosing pathology, statistical shape analysis methods to-date have been largely focused on components of the brain and heart and their associated afflictions. Such applications have included analyzing changes in the shape of the hippocampus and/or the ventricles of the brain with respect to Alzheimer’s disease [61, 89] and Schizophrenia [53, 85] and analyzing changes in the shape of the RV with respect to PH [95] and TOF [60, 104].

A typical statistical shape analysis framework includes several common steps, with the first being to preprocess the image sets. Preprocessing includes some combination (not necessarily in this order or including all steps) of segmentation, establishing base mathematical representations of the shapes, alignment/registration, and parameterization, which is the critical (and often most challenging) step in building the necessary correspondence between the collection of medical shapes [30]. Once a final correspondence is set, standard pattern recognition methods can be applied to derive the fundamental shape features that exist within the shape sets, commonly utilizing some variant of principle component analysis (PCA) [60, 95], and then generate metrics and classifiers associated with the function and/or pathology of the application of interest.

There have been a wide variety of specific techniques employed within statistical shape analysis frameworks depending on specific features, restrictions, and/or objectives of the particular applications that have been considered. With respect to the base representation of shape, one straightforward concept that has been used is to define the collection of surface points describing the shape in a standard Cartesian coordinate system, either in a discrete or continuous format. For discrete descriptions, a popular method has been to use anatomical features as landmarks or fiducial points to represent the geometric features among a population [83, 20]. However, due to limitations on the availability of landmarks in

many applications, other more mathematically based methods have been introduced to automatically generate dense collections of semi-landmarks (i.e., surface points not necessarily related to anatomical features) to represent the shape, with point distribution models being a popular method within this category [86]. For continuous descriptions, mesh-based techniques (e.g., point distributions interpolated with polynomials with compact support) are a common means for shape representation [28]. Alternatively, global basis functions (i.e., functions with non-compact support) have also been utilized for representation of shape, including basis functions such as spherical harmonic functions (SPHARM) [34] or wavelet functions [100]. Lastly, skeletonization approaches have been used in some applications for the shape representation, such as the medial shape description, which defines the shape in terms of a medial axis and the radial distance from this medial axis to the shapes surface [84]. Some of these approaches for quantitatively describing the shape are automatically comparable in a logical and anatomically consistent manner, such as the methods that simply rely on a set of anatomical features/landmarks. However, more generally, and particularly when anatomical landmarks are limited, further processing is required to build correspondence (i.e., a one-to-one relationship between each point describing each shape). One common technique has been to utilize some form of topological mapping to map every point on each shapes surface through some consistent mathematical technique (e.g., simple projection [30] or harmonic mapping [62]) to a common topologically equivalent structure, such as the surface of a plate or a sphere [30]. Finally, rigid registration is often applied to remove effects of size, orientation, and/or position, so that the subsequent statistical analysis can be focused on shape alone. The shapes can be aligned simply in some cases through manual manipulation or casting the statistical analysis in terms of the difference in shape from a reference position/shape [75]. Alternatively, some applications require more elaborate registration algorithms, such as methods that define a template shape and align each shape by minimizing the distance to the template through the iterative closest point algorithm [14] or the procrustes methodology [36], or the SPHARM approach, which actually utilizes a component of the base shape representation itself (e.g., the first-order ellipsoidal component) to align each shape [86]. Again, a critical point is that in some instances the specific statistical shape analysis implementation is chosen based on requirements/limitations of the specific applica-

tion and available resources, such as limited computational capability or insufficient available fiducial points. However, in many other cases there is not necessarily any restrictions forcing the use of a specific approach, and yet the nature of the application (i.e., the organ/structure and disease of interest) should dictate the use of one methodology over another.

Cardiac structures represent one area of significant interest for statistical shape analysis methods, as cardiac dysfunction is often thought to be measurable through distortion within the geometric features at a specific cardiac phase or by deterioration/changes in the kinematic patterns within the cardiac cycle [93, 79]. However, cardiac structures represent a particular challenge also, in comparison to many other clinical applications to-date. These challenges are largely due to the substantial shape variability that can be seen across a population and resulting from various pathological changes, as well as the dynamic variations in shape seen throughout the cardiac cycle. The concept of statistical shape analysis for cardiac structures was first introduced in [33], which used a landmark-based representation of the LVs and RVs at end-diastole (ED) and derived shape features from these with PCA. Since the work of Frangi et al., there have been a variety of other techniques applied to cardiac structures in a variety of ways (e.g., utilizing varying heart components, landmarks, and/or phases in the cardiac cycle). For instance, Huang et al. used SPHARM descriptors along with alignment techniques based on the spherical harmonic decomposition to examine the shape of the endocardial and epicardial surfaces of LVs throughout a cardiac cycle, and then heuristically derived features of these shapes and used hierarchical clustering methods to examine mechanical dyssynchrony of the heart [44]. Andreopoulos and Tsotsos presented a framework that also used landmark-based models for the endocardial and epicardial surfaces of LVs throughout a cardiac cycle, and combined PCA to produce active shape and appearance models to be used for automated segmentation purposes [3]. Similarly, Zhang et al. used landmark-based models within a combination active shape and appearance model using PCA for the endocardial and epicardial surfaces of LVs and RVs throughout a cardiac cycle to first aid with segmentation, and then to build quantitative shape, motion, and volumetric features for classification of TOF [104] Alternatively, Mansi et al. introduced currents and diffeomorphic registration algorithms to build correspondence for mesh-based continuous descriptions of RV endocardial surfaces at ED, then PCA was applied to reduce

the dimensionality as well as derive quantitative features to identify correlations with the clinical metrics and to better classify and understand TOF [60]. Recently, Wu et al. also used mesh-based continuous descriptions of RV endocardial surfaces throughout a cardiac cycle, applied a harmonic mapping method and converted the surfaces into relative shape change functions to build correspondences, and then applied proper orthogonal decomposition (POD) (i.e., a continuous form of PCA) to derive kinematic features and build metrics for potential classification of PH [95]. Overall, these recent research efforts in statistical shape analysis applied to the heart have shown promising results for both image processing and pathology classification. However, the recent efforts have also included a diverse set of components in the analysis process (e.g., different mathematical representations, different registration and decomposition techniques, etc.) with limited motivation for why one approach is utilized over another. As stated previously, after factoring out restrictions necessitated by the nature of the available imaging data, a natural assumption is that one computational approach, including both the analysis methods (e.g., representation, decomposition, etc.) and the cardiac information utilized (e.g., specific cardiac phase), will be best suited for a given structure and/or pathology. And yet, no study to-date has made a direct comparison to quantify the effectiveness of alternate shape analysis approaches for a given application.

3.2.3 Aim of Study

The present study aims to compare and contrast some approaches to statistical shape analysis that have been utilized to-date for various studies, applied herein to analyze right ventricle endocardial surfaces (RVES) for hearts with and without PH. The investigation focuses on two specific workflows for statistical shape analysis, a spherical harmonic function-based approach, as presented in [86], and a direct decomposition approach, as presented in [95], comparing the components of each framework at the various analysis stages (representation, alignment, decomposition) as well as the output of the complete workflows in terms of the potential to assess RV function. Additionally, different methods of utilizing the available imaging data are also investigated by considering analysis results when incorporating several

different combinations of the phases captured throughout a single cardiac cycle for the patient set. As such, the present study is intended to explore through comparison the efficiency and effectiveness of these specific shape preprocessing and feature extraction approaches applied to the human RV with respect to PH, and ideally provide guidance on techniques to use for further (larger) studies of the same or similar biological structure and pathology. In addition, more generally, this study is intended to provide an example structure of the tests that could, and in many cases should be performed toward determining the most suitable shape analysis strategy for a given pathology and/or biological structure of interest. Section 2 presents the steps of the selected two workflows surfaces. In Section 3 the computational performance of both workflows as well as the clustering results of both workflows in combination of different ways of utilizing cardiac information are shown and discussed, followed by a the concluding remarks in Section 4.

3.3 METHODS

Two different contemporary statistical shape analysis approaches were chosen to be applied to assess human RV function and compared for the present study: (1) an approach that directly applies POD to harmonically mapped surfaces, as shown in [95], and (2) an approach that also harmonically maps the surfaces, but then projects the surfaces onto spherical harmonic functions prior to further analysis, as shown in [78]. In addition, the analysis and assessment of each approach included two different alignment techniques for comparison purposes. In the remaining text the direct mapping to POD approach will be referred to as the DM-POD approach and the spherical harmonic function-based approach will be referred to simply as the SPHARM approach. An overview of the analysis approaches considered herein is shown in Fig. 3.1. In brief, both approaches begin with segmenting 3D surface representations of the RVES from the cardiac image sets and generating mesh-based representations of the surfaces. Then, the respective version of harmonic mapping is applied to parameterize the set of RVES with respect to a common domain. As shown with the solid red line in Fig. 3.1, the DM-POD approach goes directly from harmonic mapping to

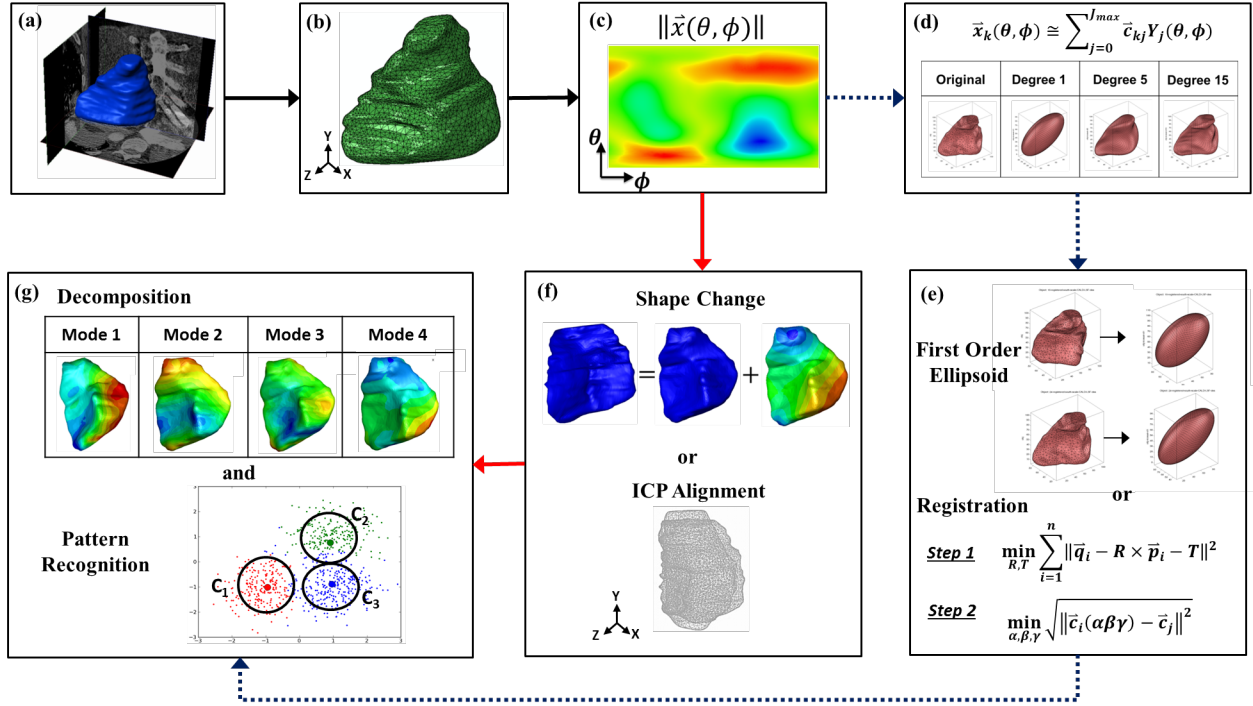


Figure 3.1: Schematic of the statistical shape analysis workflows, including the approach that directly applies POD to harmonically mapped surfaces (DM-POD - solid red arrows) and the approach that projects the surfaces onto spherical harmonic functions after harmonic mapping (SPHARM - dotted blue arrows), showing the key steps of (a) segmentation of the right ventricle endocardial surface (RVES) from the medical images, (b) smoothing and interpolated 3D closed surface mesh generation, (c) parameterization of the RVES in terms of spherical coordinates (shown in 2D), (d) projection of the RVES onto a spherical harmonic function basis (SPHARM), (e) alignment of the surfaces based on the spherical harmonic function parameterization (SPHARM), (f) alignment of the surfaces either by conversion into shape change functions or by a rigid registration algorithm (DM-POD), and (g) decomposition of the shape sets into modes and application of pattern recognition techniques.

alignment of the shapes by either converting the shapes into relative shape change functions over the cardiac cycle of each patient or registering the shapes to a preselected shape template. Once the set is aligned, the DM-POD approach applies POD to decompose the set of shapes or shape change functions into modes, and pattern recognition techniques are utilized to generate features from the modes, cluster the population, and/or build classifiers. Alternatively, as shown with the dotted blue line in Fig. 3.1, following harmonic mapping the SPHARM approach redefines the shapes in terms of a spherical harmonic function basis. Then, the SPHARM approach aligns the shapes either based on the orientation of the first-order ellipsoidal basis function or using a combination of template registration and an approach that rotates the surfaces in the space of the spherical harmonic coefficients. Lastly, the SPHARM approach utilizes PCA to decompose the sets of coefficients of the spherical harmonic functions to similarly obtain shape modal vectors (in the space of the spherical harmonic basis), and then pattern recognition techniques are applied. Note that PCA and POD can be considered conceptually identical, but are differentiated here such that POD is applied to decompose the continuous descriptions and PCA is applied to decompose the discrete descriptions. In the following, each step of the analysis methods, including the surface representation, parameterization, registration, and statistical decomposition, are elaborated upon.

3.3.1 Image Acquisition and Surface Extraction

The present work utilized a clinically obtained set of ECG-gated multislice cardiac CT images corresponding to 13 separate patients from a study on regional RV structural and functional adaptation to PH as previously reported in [80]. The 3D surface descriptions of the RV shapes were obtained for each of the 9 unique phases captured from the cardiac cycle for each of the 13 patients by manually segmenting the RVES from each image in the CT stacks, interpolating the slices, and then smoothing the interpolated surfaces using a standard recursive and discrete Gaussian filter within the commercial medical image processing software Simpleware¹. Thus, each of the 3D surfaces could be considered as a continuous, linearly

¹www.simpleware.com

interpolated, mesh-based representation, and the collection of 117 (13 patients with 9 cardiac phases per patient) continuous, 3D, non-overlapping, closed, genus-0 RVES are labeled as $\{\Omega_k\}_{k=1}^{117}$. Manual segmentation was used to ensure that the most anatomically accurate representations of the ventricle shape were segmented within the constraints of the CT image quality. Similarly, the endocardial surface was chosen specifically due to the relatively high imaging contrast between the wall tissue and blood. The segmentation was overseen and verified by a trained cardiologist (M. A. Simon), who has over ten years of experience in advanced heart failure, PH, and in particular, experience in the imaging of the RV.

3.3.2 Surface Parameterization

Both approaches initially utilized a harmonic topological mapping method, so that the RVES were quantitatively comparable over a common domain for further analysis. A harmonic mapping (i.e., change in coordinates) is simply a parameterization that satisfies Laplace’s equation for each new parameter [11]. As such, choosing the new parameters to be the spherical coordinates, ϕ (longitude) and θ (latitude), the spherical coordinates for each point on the k^{th} RVES (i.e., location of the RVES coordinates on the unit sphere) can be determined from the solution of

$$\nabla^2\theta(\vec{x}) = 0 \text{ and } \nabla^2\phi(\vec{x}) = 0, \forall \vec{x} \in \Omega_k. \quad (3.1)$$

Provided with sufficient boundary conditions for θ and ϕ , which will be discussed in more detail in the following, Eqn. 3.1 can be numerically solved, and then each RVES can be described over the common domain as

$$\vec{x} = \vec{x}(\theta, \phi) \text{ in } \theta \in [0, \pi], \phi \in [0, 2\pi], \forall \vec{x} \in \Omega_k. \quad (3.2)$$

3.3.2.1 DM-POD Approach: For the DM-POD approach, each surface mesh was parameterized solely using a two step variation of harmonic topological mapping. Specifically, the DM-POD approach creates an initial mapping by solving Eqn. 3.1 with boundary conditions for θ and ϕ corresponding to anatomical features. Accurately determining sufficient anatomical references may be a challenge in certain applications, and yet, by choosing the boundary conditions to relate to specific consistently identifiable anatomical features, this

approach is able to maintain anatomical consistency in the parameterization across populations. The RVES data used here provided more than sufficient anatomical references that could be consistently identified. For the analysis presented the boundary conditions utilized included the apex, where $\theta = 0$, the intersection of the pulmonary valve with the anterior border between the free wall and septum, where $\theta = \pi$, and the entire anterior border between the free wall and septum, where ϕ has a non-unique value of 0 and 2π . A secondary parameterization is then applied due to the fact that using only the initial harmonic mapping may lead to the surface information being excessively concentrated in the mapped domain with a majority of the surface having initial ϕ and/or θ values within a relatively small range, which may cause numerical difficulties and degrade the subsequent analysis. This second step relies on the observation that the harmonic parameterization of a sphere defines the relationship between uniformly distributed spherical surface coordinates over the unit sphere domain (the same domain as the mapped domain) and the distortion caused by the mapping, and therefore the inverse of this mapping, which is what is utilized, will “undo” some amount of the distortion caused by the harmonic mapping process. See [96] for additional details about the two-step mapping approach used for the DM-POD workflow.

3.3.2.2 SPHARM Approach: In contrast to the DM-POD approach, the SPHARM approach considers the surfaces in a discrete format in terms of the mesh vertices and connectivity, and a spherical parameterization algorithm known as the control of area and length distortions (CALD) is applied to perform the mapping [77]. The CALD algorithm consists of an initial harmonic parameterization followed by local and global smoothing methods. For initial parameterization, the CALD approach does not use anatomical landmarks for the harmonic mapping boundary conditions, as was the case in DM-POD. Rather, CALD identifies two poles ($\theta = 0$ and $\theta = \pi$) to be the two vertices whose projections onto the principal Cartesian axis are furthest apart, then defines a dateline ($\theta = 0$ or $\theta = 2\pi$) as the path with the steepest latitude ascent, and applies these boundary conditions to solve Eqn. 3.1. Then, in order to improve the area distortion (i.e., the inconsistent ratio between the area of the elements within the original surface mesh and the initial parametrized mesh), the latitude obtained from the initial mapping is re-parameterized twice using a rotation

operator, and the best (i.e., the parameterized mesh with minimal overall area distortion) of these three parameterization results (including the initial) is chosen for future usage. To further compensate for the area distortion the CALD approach uses an optimization algorithm that combines local and global smoothing methods to iteratively relocate vertices of the parameterization based on minimizing the area distortion of the surface mesh elements with controlled length distortion, while also trying to equalize the mesh distribution in terms of area over the spherical coordinates. After parameterization, the SPHARM approach expands each of the mapped surfaces into a combination of spherical harmonic functions, such that the k^{th} RVES can be described as

$$\vec{x}_k(\theta, \phi) \cong \sum_{j=0}^{J_{max}} \vec{c}_{kj} Y_j(\theta, \phi), \quad (3.3)$$

where $Y_j(\theta, \phi)$ is the j^{th} spherical harmonic basis function, \vec{c}_{kj} is the corresponding 3D coefficient vector for the k^{th} RVES, and J_{max} is the number of spherical harmonic functions included in the description. Therefore, each RVES can be defined uniquely by the set of corresponding spherical harmonic function coefficients.

3.3.3 Surface Alignment

Overall, surface alignment is applied to remove the effects of size, orientation, and/or position, so that the subsequent analyses of the RVES set consider shape alone. Two alignment methods were considered here for each shape analysis workflow. The DM-POD workflow included one approach that converts the shape sets into relative shape change (i.e., pseudo-displacement) functions of the RVES for each patient, and another approach that is a more standard rigid registration approach derived from the iterative closest point algorithm. Alternatively, the SPHARM workflow tested an alignment approach based on the first-order ellipsoidal component of the spherical harmonic function expansion, as well as an approach that minimizes the distance between the shapes in the set with respect to the set of spherical harmonic function coefficients from the expansions.

3.3.3.1 Pseudo-Displacement: As shown in [95], an approach to convert RVES shape sets into pseudo-displacement functions has been used to circumvent the additional computational cost and nonuniqueness of traditional registration methods. The primary assumption with this approach is that given a consistently identifiable phase (i.e., end diastole) to use as reference, the normalized change in shape of an individual’s RVES over a cardiac cycle is fundamentally consistently comparable across a population of individuals, provided that any displacement not directly relating to beating of the heart is negligible throughout the image acquisition process. As such, the parameterized RVES can be converted into pseudo-displacement shape change functions simply by subtracting one chosen phase’s RVES from each other phase’s RVES over the cardiac cycle for each individual separately as

$$\vec{d}_k^i(\theta, \phi) = \vec{x}_k^i(\theta, \phi) - \vec{x}_r^i(\theta, \phi), \quad \text{and } k \neq r, \quad (3.4)$$

where \vec{d}_k^i is the pseudo-displacement function for the i^{th} patient at the k^{th} timeframe in the cardiac cycle and r is the chosen referential phase index for the corresponding patient. Then, each pseudo-displacement function can be normalized (i.e., scaled) with respect to the maximum change in the cardiac cycle for the corresponding individual as

$$\vec{p}_k^i(\theta, \phi) = \vec{d}_k^i(\theta, \phi) / \max_j \|\vec{d}_j^i(\theta, \phi)\|_{L_2}, \quad (3.5)$$

with $\|\cdot\|_{L_2}$ defined as the standard L_2 -norm. The end diastole phase was chosen as the referential phase for all analysis herein that used the pseudo-displacement method for alignment.

3.3.3.2 Iterative Closest Point: The iterative closest point (ICP) rigid registration algorithm [27] was also considered to complete the correspondence for the RVES set within the DM-POD workflow to more directly analyze shape (rather than change in shape). For the ICP algorithm a template surface is chosen from the set, and then each other surface in the set is iteratively rotated and translated until the distance between each surface and the pre-selected template surface is minimized. For the present study, the RVES for an arbitrary non-hypertensive patient at end diastole was chosen as the template shape. Furthermore, only a single final rotation operator and translation vector were determined for each patient using the ICP algorithm in order to align the end diastole RVES of each patient to the

template RVES, and then this rotation operator and translation vector were applied to each other phase for each respective patient. Therefore, the kinematic information over the cardiac cycle for each patient was also preserved with this ICP registration approach. In addition, prior to registration each RVES was normalized, similarly applying a single scaling operator for each patient with respect to the internal cavity volume of the respective end diastole RVES compared to the template surface. Thus, the registered RVES for the i^{th} patient at the k^{th} timeframe in the cardiac cycle can be shown as

$$\vec{p}_k^i(\theta, \phi) = R_{ED}^i \times (S_{ED}^i \times \vec{x}_k^i(\theta, \phi)) + \vec{T}_{ED}^i, \quad (3.6)$$

where R_{ED}^i , S_{ED}^i , and \vec{T}_{ED}^i are the rotation operator, scaling operator, and translation vector corresponding to the patient at ED phase, respectively.

3.3.3.3 First-Order Ellipsoid: The first approach used to address the alignment need in the SPHARM workflow was an approach that relies primarily on the first-order ellipsoidal component of the SPHARM expansion [86]. For this approach, each RVES is scaled (i.e., normalized) individually with respect to the internal cavity volume (note, this differs from the scaling in the DM-POD workflow, which uses a single scaling value for each patient rather than a separate scaling value for each shape). Next, the 0^{th} -degree spherical harmonic function term is removed from the expansion to center the shapes in the set. The parameterization is oriented by first aligning the poles ($\theta = 0$ and $\theta = \pi$) with the positive and negative ends of the longest major axis of the ellipsoidal (1^{st} -degree) spherical harmonic functions and aligning the intersection of the dateline ($\phi = 0$) and the equator ($\theta = \pi/2$) with the positive end of the shortest axis of the ellipsoid. Lastly, the RVES are oriented in object space by determining the rotations necessary to make the three main axes of the ellipsoidal spherical harmonic functions coincide with the Cartesian coordinate axes with the shortest axis of the ellipsoidal functions along the x-axis and the longest axis of the ellipsoidal functions along the z-axis. The object space rotations are then applied to all spherical harmonic function coefficients in combination with the previous operations as

$$\vec{c}_k^f = R_k^{object} \times R_k^{parameter} \times (S_k^{FOE} \times \vec{c}_k), \quad (3.7)$$

where \vec{c}_k is the initial (following surface parameterization) spherical harmonic coefficient vector for the k^{th} patient, S_k^{FOE} , $R_k^{parameter}$, and R_k^{object} are the scaling operator, rotation operator in parameter space, and rotation operator in object space corresponding to the k^{th} patient, respectively, and \vec{c}_k^f is the final spherical harmonic coefficient vector for this aligned individual.

3.3.3.4 Registration of SPHARM Parameterization: The final approach considered to complete the correspondence with the SPHARM workflow was an approach that combines an ICP-type algorithm with a method that aligns the shapes in the space of the spherical harmonic function parameterization (in some cases referred to as the SHREC algorithm in the literature) [77]. The first step is similar to the ICP algorithm shown in Section 3.3.3.2, which initially aligns (i.e., rotates, translates, and scales) each shape to a pre-selected template by minimizing the distance between a selected group of landmarks prior to expansion into spherical harmonic functions. Therefore, the initially aligned k^{th} RVES (including all patients at all phases) can be shown as

$$\vec{x}_k^* = R_k^* \times (S_k^* \times \vec{x}_k) + \vec{T}_k^*, \quad (3.8)$$

where R_k^* , S_k^* , and T_k^* are the rotation operator, scaling operator, and translation vector, respectively. Then, each of the aligned shapes (i.e., \vec{x}_k^*) is parameterized and expanded to obtain the spherical harmonic function coefficients, \vec{c}_k . The final step rotates the spherical harmonic function coefficients using three rotation parameters, α , β , and γ , to minimize the difference between the spherical harmonic coefficient vector of each shape and the template shape to produce the final set of aligned spherical harmonic function coefficients, \vec{c}_k^f , as

$$\min_{\alpha, \beta, \gamma} \sqrt{\|\vec{c}_k^f(\alpha, \beta, \gamma) - \vec{c}_i\|^2}, \quad (3.9)$$

where

$$c_k^f(\alpha, \beta, \gamma) = R^f(\alpha, \beta, \gamma) \times \vec{c}_k, \quad (3.10)$$

R^f is the rotation operator, and \vec{c}_i is the spherical harmonic function coefficient vector of the selected template.

3.3.4 Statistical Decomposition

As stated previously, the decomposition approaches of POD and PCA are conceptually equivalent, but are differentiated herein such that POD was applied to decompose (i.e., obtain shape modes from) the continuous function RVES descriptions for the DM-POD workflow, while PCA was applied to decompose the coefficients of the spherical harmonic functions for the SPHARM workflow. Therefore, the POD approach determines the optimal set of modes (i.e., modal shapes) $\{\vec{v}_i(\theta, \phi)\}_{i=1}^n$ in an average sense to approximate the set of mapped and aligned RVES as

$$\vec{p}_k(\theta, \phi) \approx \sum_{i=1}^n a_{ki} \vec{v}_i(\theta, \phi) + \vec{b}(\theta, \phi), \quad (3.11)$$

where $\vec{p}_k(\theta, \phi)$ is the k^{th} shape or shape change function, $\vec{b}(\theta, \phi)$ is the translation function, a_{ki} are modal coefficients, and n is the total number of modes. For the present work the translation function was taken as $\vec{0}$ when analyzing the pseudo-displacement and taken as the mean shape when analyzing the shapes with the ICP alignment. Similarly, the PCA approach determines the optimal set of i.e., principle components $\{\vec{r}_i\}_{i=1}^n$ to approximate the set of spherical harmonic function coefficients for each mapped and aligned RVES as

$$\vec{c}_k \approx \sum_{i=1}^n d_{ki} \vec{r}_i + \vec{z}, \quad (3.12)$$

where \vec{c}_k is the k^{th} RVES spherical harmonic function coefficient vector, \vec{z} is mean vector, and d_{ki} are modal coefficients. Therefore, the corresponding modal shapes $\{\vec{w}_i(\theta, \phi)\}_{i=1}^n$ can be obtained from the principal components of the spherical harmonic function coefficients as

$$\vec{w}_i(\theta, \phi) = \vec{r}_i \cdot \vec{Y}(\theta, \phi), \quad (3.13)$$

where $\vec{Y}(\theta, \phi)$ is the collection of spherical harmonic functions. See [95] for more details regarding the formulation and implementation of POD directly applied to shape analysis, and see [78] for more details regarding the formulation and implementation of PCA for shape analysis.

3.4 RESULTS AND DISCUSSION

3.4.1 Human Cardiac Image Dataset and Clinical Classification

The statistical shape analysis methods presented were applied to the discussed set of clinically obtained ECG-gated multislice cardiac computed tomography (CT) images for 13 individuals from a study on regional RV structural and functional adaptation to PH as previously reported in [80]. All patients were scanned within 2 days of invasive hemodynamic measurements on either a GE Lightspeed 16-slice scanner or a GE VCT 64-slice scanner². Scan parameters were as follows: kV 120; mA approximately 400 without ECG-dose modulation; rotation time $350msec$; pitch dependent on heart rate; $1.25mm$ slice thickness (for 16 detector scanner); kV 120, mA approximately 500 with ECG-dose modulation adjusted to peak at 65-80% R-R interval; rotation time $350msec$; pitch dependent on heart rate; $0.625mm$ slice thickness (for 64 detector scanner). As stated in Section 3.3.1, 3D closed RVES were manually extracted for each of the 13 patients at each of the 9 unique phases spaced uniformly in one complete cardiac cycle.

The 13 patients were initially clinically classified based on resting mean pulmonary arterial pressure (PAP) and right atrial pressure (RAP), with six patients grouped as “non-hypertensive” based on $PAP \leq 25mm\ HG$ (labeled as N1-6), six patients grouped as “hypertensive with decompensated RV function” based on $PAP > 25mm\ HG$ and $RAP > 10mm\ HG$ (labeled as D1-6), and one patient grouped as “hypertensive with compensated RV function” based on $PAP > 25mm\ HG$ and $RAP < 10mm\ HG$ (labeled as C1). Fig. 3.2 shows the distributions of PAP and RAP for the 13 patients within the dataset. In all cases, patients with $RAP > 10mm\ HG$ also had a cardiac index $< 2.0L/min/m^2$. An important note is that all patients within the study (even those classified as “non-hypertensive”) are symptomatic, and therefore, not an average healthy individual. To provide an additional clinical metric relating to RV function, Fig. 3.3 shows the volume ejection fraction in comparison to what would be considered a “normal” range (as estimated in [32]) for each of the 13 patients.

²(General Electric Healthcare; Milwaukee, WI, USA)

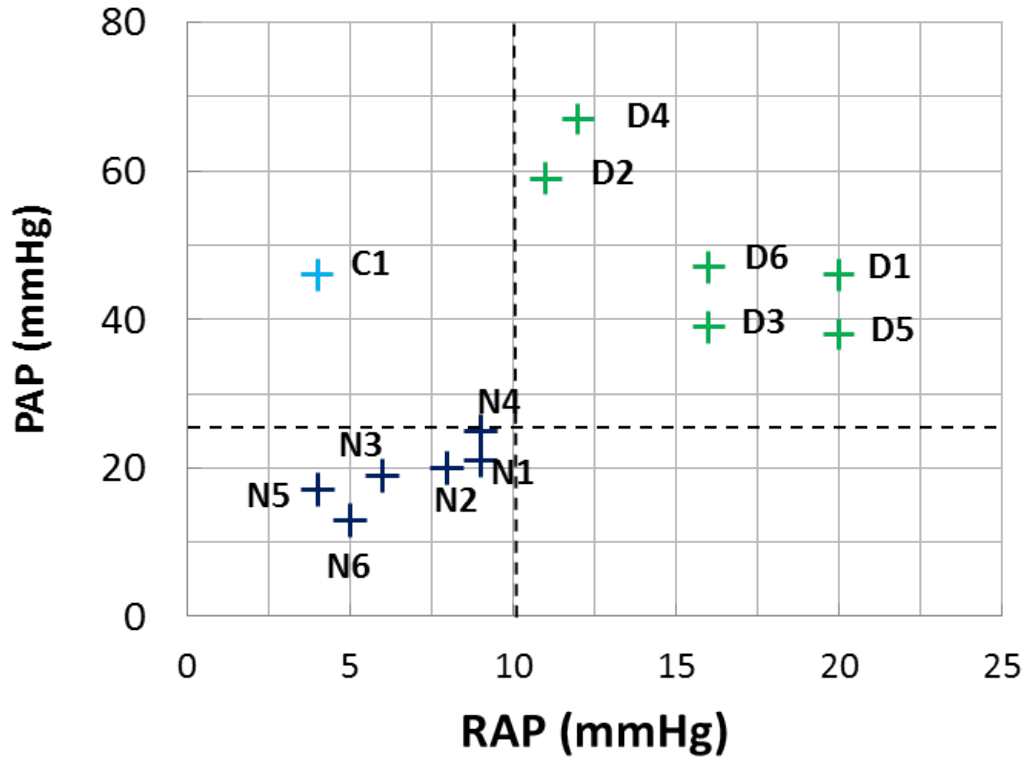


Figure 3.2: Hemodynamic distribution of the six non-hypertensive (marked as N1 - N6 with black cross), six hypertensive with decompensated right ventricle (RV) function (marked as D1 - D6 with green cross), and one hypertensive with compensated RV function (marked as C1 with blue cross) patients considered for this study in terms of the mean pulmonary arterial pressure (PAP) and right atrial pressure (RAP).

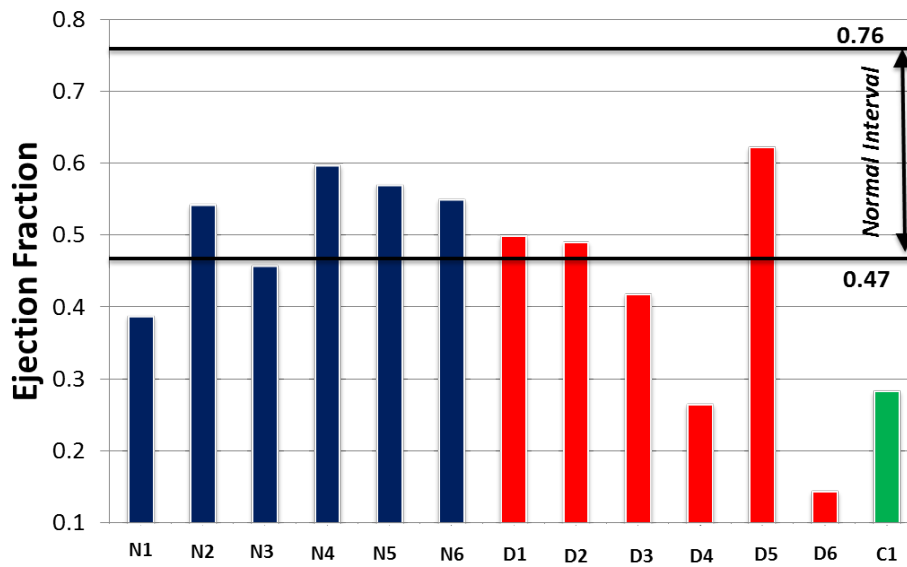


Figure 3.3: Ejection fraction of the six non-hypertensive (N1 - N6), six hypertensive with decompensated right ventricle (RV) function (D1 - D6), and one hypertensive with compensated RV function (C1) patients considered for this study.

3.4.2 Mapping and Alignment

Fig. 3.4 shows the initial orientation (i.e., the orientation of the RVES after segmentation, but prior to any alignment) of a representative set of six segmented and smoothed RVES shapes at the ED phase, as well as the results of the mapping to spherical coordinates and orientations of each RVES following the various parameterization and alignment methods of each workflow (note that the pseudo-displacement alignment results are not shown since this approach is the only method not routed in traditional registration, and therefore not directly comparable in this manner to the other strategies). Note that the mapping results are displayed through the color contours, such that the colors correspond to values of the mapping variables (i.e., the spherical coordinates θ and ϕ) as shown in Fig. 3.4. In addition, for the SPHARM workflow two additional trials were performed (labeled with “Updated”), in which the orientations of the RVES were first manually adjusted according to the anatomical references (i.e., the RVES were manually rotated to place the pulmonary valve, apex, septum, and free wall in a similar posture throughout the population) and then the two SPHARM alignment methods in combination with the parameterization algorithm were applied again.

Overall, the alignment results for the ICP algorithm within the DM-POD framework appeared to orient all of the RVES such that the various anatomical regions that can be identified (e.g., the pulmonary outflow track, the tricuspid valve, the apex, the free wall, and the septum) were in consistently similar relative positions. The FOE and SHREC algorithms from the SPHARM workflow oriented the majority of the RVES with a similar amount of anatomical consistency in comparison to the ICP algorithm in the DM-POD workflow. However, some of the registration results for the FOE and SHREC algorithms were far less anatomically consistent compared to the ICP algorithm. For example, after applying the FOE algorithm the free wall for patient *N3* was facing outward rather than to the right, as was the rest of the population, and the pulmonary valve for patient *D5* was pointing outward rather than toward the top. Furthermore, after applying the SHREC algorithm the orientations of nearly all of the anatomical features for patient *N3* were in significantly different positions compared to the rest of the population, but generally the SHREC algorithm appeared to produce orientations that were anatomically similar more

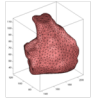
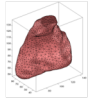
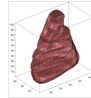
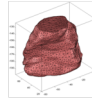
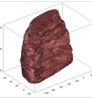
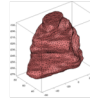
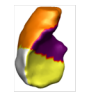
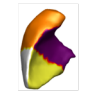

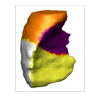
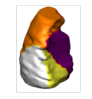
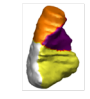

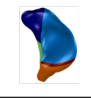

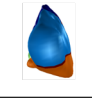
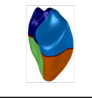

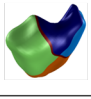






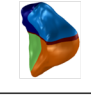








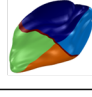
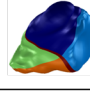
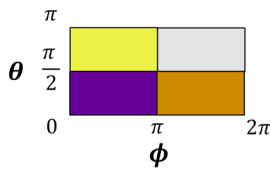
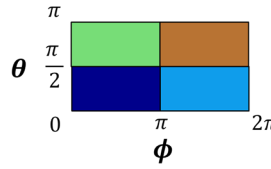
Patient #	N3	N5	D1	D5	D6	C1
Initial Orientation						
DM-POD ICP						
SPHARM FOE						
SPHARM SHREC						
Updated SPHARM FOE						
Updated SPHARM SHREC						
Mapping Results Legend						
DM-POD			SPHARM			
						

Figure 3.4: Initial orientation of a representative set of six segmented and smoothed right ventricle endocardial surface (RVES) shapes at the end diastole (ED) phase of the cardiac cycle, including two non-hypertensive patients (N3 & N5), three hypertensive with decompensated right ventricle (RV) function patients (D1, D5, & D6), and one hypertensive with compensated RV function patient (C1), as well as the results of the mapping to spherical coordinates (color contours) and orientations of each RVES following the two step harmonic mapping and the iterative closest point (ICP) alignment of the DM-POD workflow, and the harmonic mapping followed by the control of area and length distortions (CALD) algorithm and the first order ellipsoid (FOE) or the SHREC alignment of the SPHARM workflow. Additionally, for the SPHARM workflow the two updated alignment trials are shown (labeled with “Updated”), where the orientation of the RVES were manually adjusted according to the anatomical references and then the two SPHARM alignment algorithms in combination with the parameterization algorithm were applied again.

consistently throughout the population than the FOE algorithm. This lack of anatomical consistency for the FOE and SHREC algorithms is not necessarily unexpected though, since the objective driving the registration process for those algorithms is based more on shape features (i.e., the spherical harmonic expansion) than anatomical features, particularly the FOE algorithm, in contrast to the entirely anatomical reference-based ICP algorithm used in the DM-POD workflow. One additional reason for the inconsistency in the orientation of the anatomical features in the results from the FOE and SHREC algorithms is that both algorithms depend significantly upon the initial orientation of the surfaces. Thus, if the surfaces are initially substantially different in the anatomical orientation they are more likely to remain different in the anatomical orientation following FOE or SHREC alignment. As such, the “Updated” FOE and SHREC results, in which the initial RVES orientation was manually set to be more anatomically consistent across the population, show some increase in the anatomical consistency across the population for the final oriented shapes. For the Updated SHREC results all of the RVES could be considered to have similar relative positioning of the anatomical features, yet, for the FOE results there were still some RVES that had substantially different orientation in terms of the anatomical references (e.g., *D5*). In general, the results for the spherical coordinate mapping (i.e., color contours) followed a similar pattern to the results for the RVES orientation, particularly for the SPHARM workflow techniques, which have a direct connection between the mapping and alignment results in the processing steps. The DM-POD workflow produced mappings that assigned values for the spherical coordinate to the various anatomical regions that were relatively similar across the population, while the SPHARM workflow had some amount of anatomical consistency, but showed substantially more variation in the spherical coordinate values for the various anatomical regions for some members of the population.

To further understand the nature of the shape descriptions, Fig. 3.5 shows the expansion of the representative set of RVES onto sets of spherical harmonic functions of varying basis order, as used in the SPHARM workflow, in comparison to the complete (i.e., non-expanded) description, as utilized in the DM-POD workflow. The first degree expansion is an ellipsoid, and this is the component that is primarily used for the FOE alignment. As such, the relatively large variation in the shape of this ellipsoid component can be understood as the

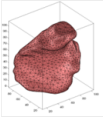
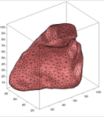
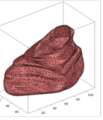
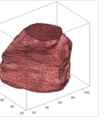
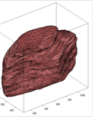
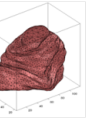
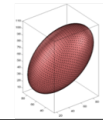
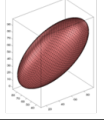
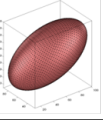
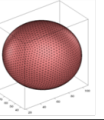
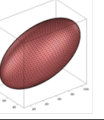
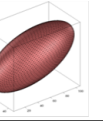
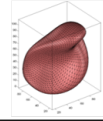
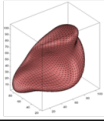
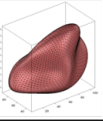
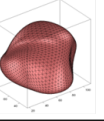
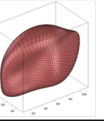
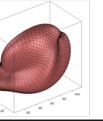
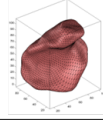
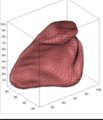
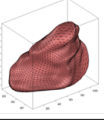
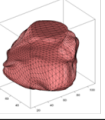
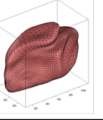
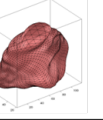
Patient #	N3	N5	D1	D5	D6	C1
Manually Rotated DM-POD						
<u>SPHARM</u>						
Degree 1						
Degree 5						
Degree 15						

Figure 3.5: A representative set of six segmented and smoothed right ventricle endocardial surface (RVES) shapes at the end diastole (ED) phase of the cardiac cycle, including two non-hypertensive patients (N3 & N5), three hypertensive with decompensated right ventricle (RV) function patients (D1, D5, & D6), and one hypertensive with compensated RV function patient (C1), manually rotated to be anatomically consistent, and the expansion of each RVES onto a collection of spherical harmonic functions after parameterization (as used within the SPHARM workflow), for spherical harmonic function bases of degree 1 (4 basis functions), degree 5 (36 basis functions), and degree 15 (256 basis functions) (with orientation maintained consistently).

core reason why the FOE alignment method produced substantial variations in the relative orientation of the anatomical features of the RVES (shown in Fig. 3.4). Regarding the representation, as would be expected, as the number of spherical harmonic basis functions included in the representation increases, the number of details of the RVES preserved by the representation also increases. What is more interesting is that a relatively large number of spherical harmonic functions are required to clearly represent the RVES. At degree 5, which equates to a total of 36 basis functions, the outline of the RVES begins to emerge, but details of some structures such as the pulmonary valve region and the papillary muscles along the free wall and septum are missing. Even at degree 15, which equates to a total of 256 basis functions, the majority of the details of the original RVES are recovered, but some fine-scale details can still be seen as missing in comparison to the original surfaces. While this expansion onto the spherical harmonic function basis may result in what could be considered as a loss of information, the expansion may alternately be viewed as a filtering process to remove features that could be contaminated by noise.





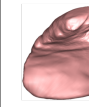
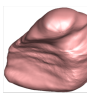
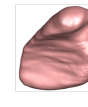

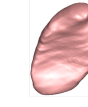
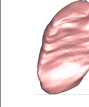
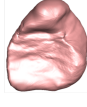
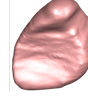


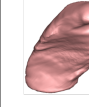
3.4.3 Statistical Decomposition

POD (for the DM-POD workflow) and PCA (for the SPHARM workflow) were applied to decompose the respective sets of parameterized and aligned RVES. However, note that while both the ICP and pseudo-displacement results were decomposed with POD for the DM-POD workflow, for brevity, the PCA decomposition in the SPHARM workflow was considered only for the parameterization and alignment results of the Updated SHREC algorithm, since the Updated SHREC results were the most similar to the ICP results for the DM-POD workflow with regards to the anatomical orientations. Additionally, four different approaches for using the available information within the cardiac cycle (i.e., phases) were considered: (1) analyzing the RVES at the single ED phase for each patient, (2) analyzing the RVES at the single ES phase, (3) analyzing the RVES at both the ED and ES phases, and (4) analyzing the RVES at all nine available phases for each patient. As would be expected, the pseudo-displacement method was only applied to approaches (3) and (4), in which the pseudo-displacement functions were calculated with the RVES as ED as the reference phase.

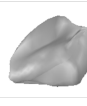





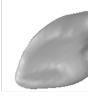








As an example of the appearance of the modal shapes that can be obtained from the decomposition methods Fig. 3.6 shows representations of the 3D modal shapes obtained by applying POD to the ICP results for the DM-POD workflow and applying PCA to the SHREC results for the SPHARM workflow to analyze only the ED phase of all 13 patients. More specifically, Fig. 3.6 shows the mean shape (i.e., the average shape of the RVES at ED over the 13 patients) in comparison to the mean shape combined with the specified modal shape multiplied by ± 1 or 2 standard deviations of the corresponding modal coefficient value across the set of 13 patients. Note that the modes produced by both workflows are ranked by their relative contribution to the representation of the set of 13 patients, such that mode 1 has the largest contribution to the shape over the set of patients, followed by mode 2, and so on. As can be seen, there were distinct differences between the modal shapes produced by each approach within each framework. For example, mode 3 obtained from the DM-POD workflow in Fig. 3.6 shows a concentrated shape variation directly below the outflow tract, while mode 3 obtained from the SPHARM workflow has no such specific regional variation, and there is actually no other mode within the set produced by the SPHARM workflow that could be considered similar in appearance to mode 3 from the DM-POD workflow. However, there is not necessarily any method to assess which modal shape set is preferred, particularly since the physiological relevance of the modes is limited in that each is strictly one statistical representation of the shape sets and subject to the mathematical constraints of the decomposition, such as orthogonality.

Since there is limited physical interpretation of these statistically generated modal shapes, it is often more useful to analyze how the various modes contribute to the representation of the shape datasets to understand the relative compactness of the modal representations, the information content within each mode, and how much variation there is in this shape information across the datasets. To understand these modal contributions Fig. 3.7 shows the cumulative modal energy for both the POD and PCA results for each of the four groupings of the cardiac phase data. For the i^{th} mode the cumulative modal energy was calculated as

$$C_i = \frac{\sum_{j=1}^i \lambda_j}{\sum_{k=1}^m \lambda_k}, \quad (3.14)$$

	$-2\sigma_i$	$-\sigma_i$	Mean	$+\sigma_i$	$+2\sigma_i$
Mode1					
Mode2					
Mode3					

(a)

	$-2\sigma_i$	$-\sigma_i$	Mean	$+\sigma_i$	$+2\sigma_i$
Mode1					
Mode2					
Mode3					

(b)

Figure 3.6: The mean shape and plus or minus one and two standard deviations ($\pm\sigma_i$ and $\pm 2\sigma_i$) of each of the first three modal coefficient values multiplied with the corresponding mode shape and added to the mean shape for analysis of the dataset of 13 patient’s right ventricle endocardial surface shapes at the end diastole phase in the cardiac cycle with (a) the DM-POD workflow with ICP alignment and (b) the SPHARM workflow with the “Updated” SHREC alignment.

where λ_k is the eigenvalue obtained through the POD/PCA process corresponding to the k^{th} mode and m is the total number of modes obtained by the decomposition. For all trials, the cumulative energy curve for the modes obtained from the DM-POD approach can be seen to be considerably steeper than the energy curve for modes obtained from the SPHARM approach, both when analyzing the shape (ICP results) and the change in shape. Thus, it can be inferred that with an equivalent number of modes the DM-POD results preserve more information within the population (i.e., are a more compact representation) than the SPHARM results. In other words, in order to retain the same amount of information the SPHARM approach needs to utilize more modes than the DM-POD approach. However, there was minimal variation in the energy distribution for different groupings of the cardiac phase information or comparing the pseudo-displacement results to the ICP results in the DM-POD workflow. Therefore, the results would indicate that the specific workflow had substantially more influence on the compactness of the modal representations than the particular cardiac phase grouping or the representation as shape change rather than shape.

3.4.4 Clustering

The last set of tests was intended to analyze the applicability and differences of the statistical shape analysis methods towards the ultimate goal of identifying and classifying shape-based patterns within patient sets. Therefore, the final set of tests considered the variations in the modal shape components across the patient set for the various analysis methods and how these modal components could potentially be used to separate the patient set into various groupings (i.e., clusters).

First, a basic K-means clustering algorithm [26] was applied to group the 13 patients within the set based on the modal coefficients extracted for each patient through the DM-POD workflow with the ICP (shape) and pseudo-displacement (shape change) strategies and the SPHARM workflow with the Updated SHREC (shape) technique for all four groupings of the cardiac phases considered (as were also considered in Section 3.4.3). The number of modes used to represent each patient (m) were selected such that at least 99% of the cumulative energy was captured for the set respectively for each approach (based on the eigenvalue

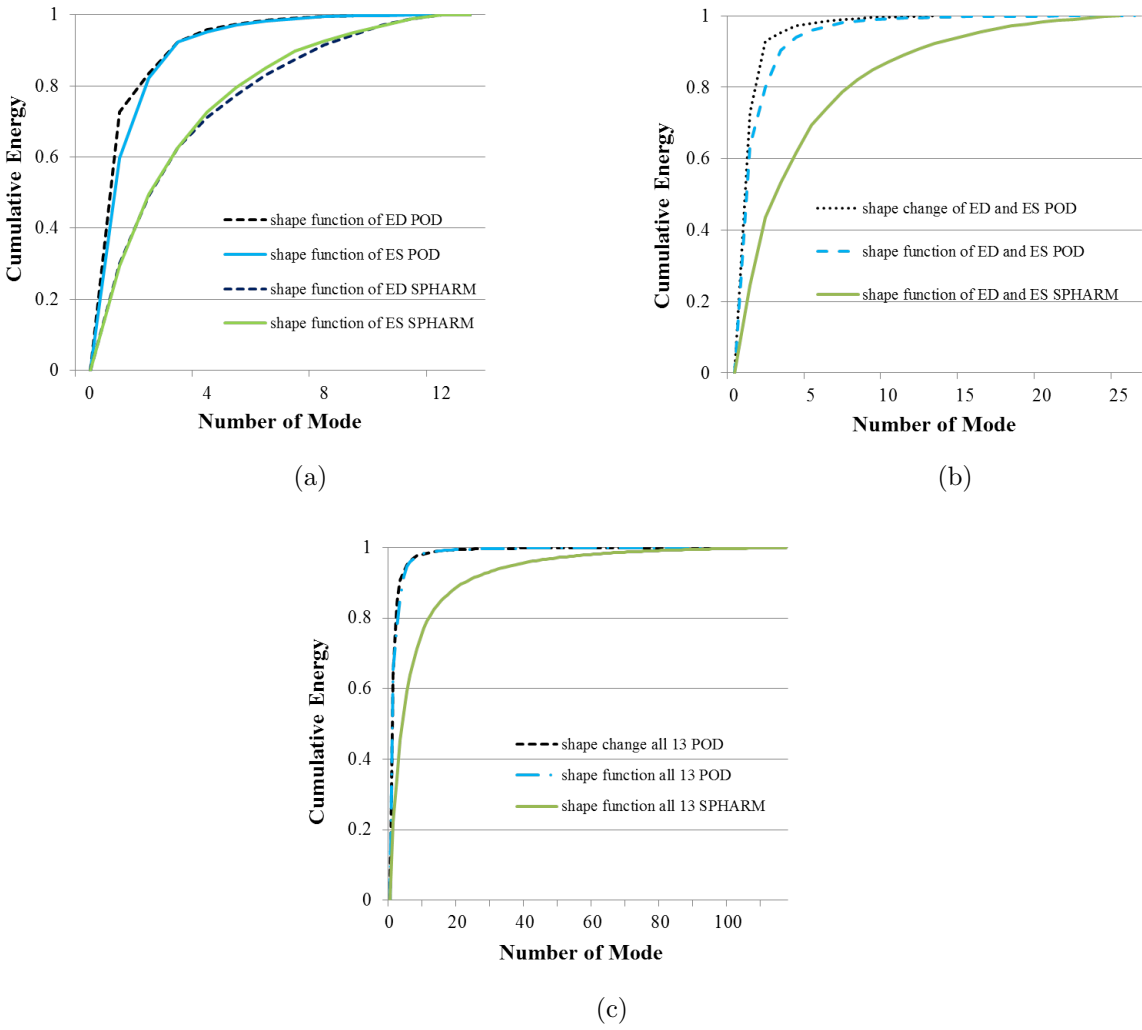


Figure 3.7: The cumulative modal energy for the POD and ICA modes obtained for the 13-patient dataset from analysis of (a) the end diastole (ED) and end systole (ES) phases in the cardiac cycle alone with the DM-POD workflow with ICP alignment and the SPHARM workflow with the “Updated” SHREC alignment, (b) the ED and ES phases combined with the DM-POD workflow with the pseudo-displacement (PD) alignment (subtracting the ED phase from the ES phase), the DM-POD workflow with ICP alignment, and the SPHARM workflow with the “Updated” SHREC alignment, and (c) all available phases with the DM-POD workflow with the PD alignment (subtracting the ED phase from all other phases), the DM-POD workflow with ICP alignment, and the SPHARM workflow with the “Updated” SHREC alignment.

analysis discussed previously), and each patient was then described for the clustering process by a vector of the individual relative modal energy percentages (as was used in [95]), with the components of this vector calculated as

$$M_i = \frac{\sum_{k=1}^n a_{ki}^2}{\sum_{j=1}^N \sum_{p=1}^n a_{pj}^2} \times 100\%, \quad \text{for } i = 1, 2, \dots, m, \quad (3.15)$$

where a_{ki} is the modal coefficient for the given patient corresponding to the i^{th} mode included in the vector and the k^{th} cardiac phase, N is the total number of modes obtained from the decomposition process of the set of 13 individuals, and n is the number of phases in the cardiac cycle used for the particular analysis case. To assess how the modal representations would group the patient set, not only with respect to each other, but also in comparison to the most basic clinical metrics that are used to classify RV function, the number of groupings was arbitrarily set to two and the groupings were compared with the clinical classification of “hypertensive” and “non-hypertensive” defined in Section 3.4.1. As such, Fig. 3.8 shows the percentage of the patients that were grouped by the K-means clustering with a majority of patients in the same classification (hypertensive or non-hypertensive) for each of the analysis approaches considered. There was a substantial variation in the rate at which the various workflows and analysis methods grouped the patients in agreement with the hypertensive/non-hypertensive classification, and thus, substantial variation in the way in which the methods grouped the patients in general. The DM-POD workflow analysis of all cardiac phases with the ICP alignment showed the highest rate of agreement with the clinical classification and the DM-POD workflow analysis of the ED and ES phases with the pseudo-displacement alignment produced the lowest rate of agreement, yet on average the results of the DM-POD workflow grouped the patients more consistently in agreement with the clinical classification than the SPHARM workflow. The results could be further interpreted to indicate that the shape of the ED phase and one more more of the intermediate phases in the cardiac cycle is more strongly correlated with the state of hypertension, while the shape of the ES phase is related to other aspects of RV function.

To explore the nature of the potential clustering capabilities of the statistical shape analysis methods further hierarchical clustering tests were performed on the two analysis

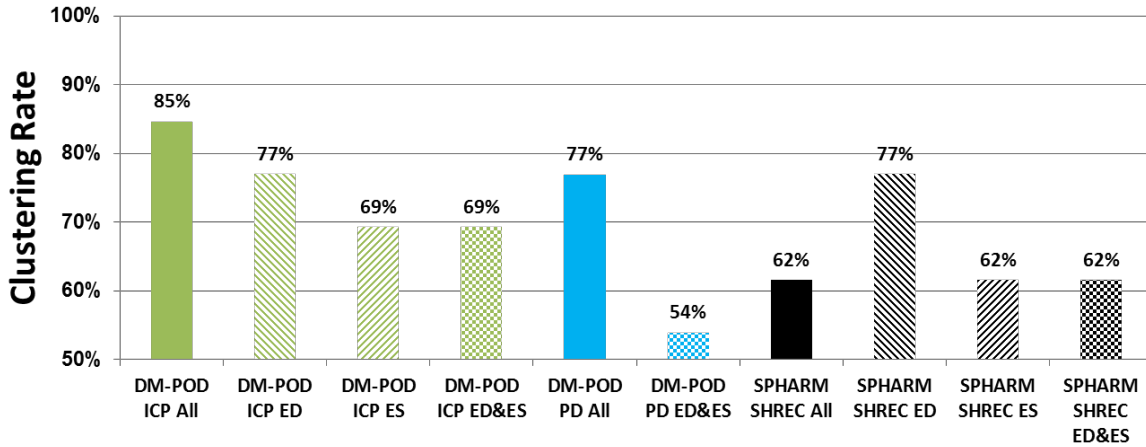
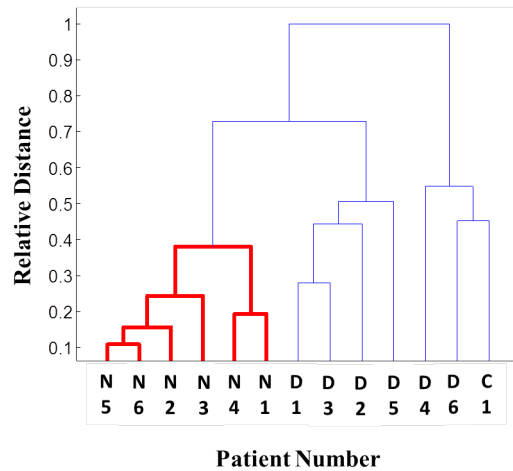
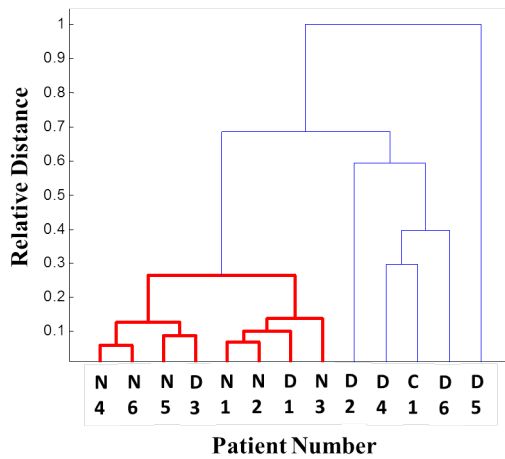


Figure 3.8: Percentage (i.e., Clustering Rate) of patients from the 13-patient dataset that were grouped by K-means clustering (assuming two classes) with the majority of patients in the same classification (hypertensive or non-hypertensive) based on the feature vector of the individual relative modal energy percentages from the DM-POD workflow analysis with ICP alignment of all available phases in the cardiac cycle, the end diastole (ED) phase alone, the end systole (ES) phase alone, and the ED and ES phases combined, the DM-POD workflow analysis with the pseudo-displacement (PD) alignment (subtracting the ED phase from all other phases) of all available phases and the ED and ES phases combined, and SPHARM workflow analysis with the “Updated” SHREC alignment of all available phases, the ED phase alone, the ES phase alone, and the ED and ES phases combined.

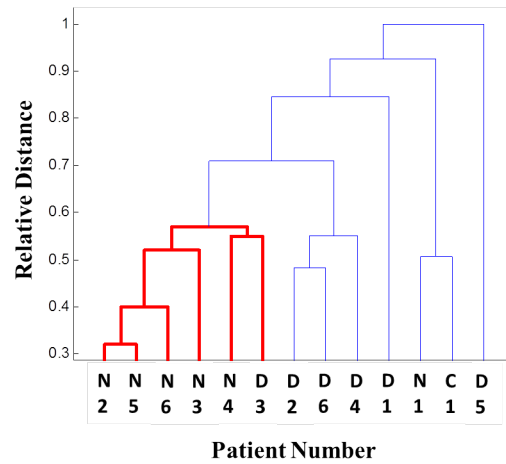
techniques (one from each workflow) that had the strongest agreement with the hypertension classification in the K-means clustering results: the DM-POD workflow analysis of all cardiac phases with the ICP algorithm and the SPHARM workflow analysis of the ED phase with the Updated SHREC algorithm. To also provide an alternate comparison of standard clinically measurable RV function an additional feature vector was created for each patient consisting of the pulmonary arterial pressure, the right atrial pressure, and the ejection fraction, with all values normalized with respect to the largest respective value in the patient set. Fig. 3.9 shows the clustering results after applying hierarchical clustering [26] to the DM-POD and SPHARM relative modal energy feature vectors, as described above, as well as the clinical pressure-volume feature vector, with the vertical lines in the figure indicating the relative distance in the feature space between the patient groups connected by the horizontal lines. As would be expected, the clinical pressure-volume features clustered all non-hypertensive patients in one group with a relatively large distance from this group to the hypertensive patient group. However, it is interesting to observe that the patient with compensated RV function was clustered considerably closer in the clinical feature space to two of the patients with decompensated RV function than those three are to the rest of the hypertensive patients with decompensated RV function and all of the hypertensive patients were clustered relatively far from each other in comparison to the non-hypertensive patients, further highlighting the wide spectrum of patient hemodynamic states and the complexity of the affects of PH on RV function. The results from the DM-POD workflow led to clustering all of the non-hypertensive patients within one relatively compact group, but also included two of the decompensated hypertensive patients in the same grouping, while having a diverse spectrum, in a similar way as the clinical features, for the remaining decompensated and compensated hypertensive patients. Alternatively, the results for the SPHARM workflow are significantly more mixed in terms of the states of hypertensive, with one relatively compact group comprised of three of the non-hypertensive individuals, four of the decompensated hypertensive individuals, and the one compensated hypertensive individual, and a second grouping that was significantly more wide spread and included three non-hypertensive individuals and two decompensated hypertensive individuals. However, it is generally impossible to say whether one approach or another is a “better” indicator of



(a)



(b)



(c)

Figure 3.9: Hierarchical clustering results (relative distance between feature vectors in the set) of the 13-patient dataset, including the 6 non-hypertensive individuals (N1 - N6), the 6 hypertensive with decompensated right ventricle (RV) function individuals (D1 - D6), and the 1 hypertensive with compensated RV function individual (C1), for the (a) clinical normalized pressure-volume feature vector, (b) individual relative modal energy percentage feature vector from the results of the DM-POD workflow with ICP alignment analysis of all available cardiac phases, and (c) individual relative modal energy percentage feature vector from the results of the SPHARM workflow with the “Updated” SHREC alignment analysis of only the end diastole cardiac phase.

RV function, relating to PH or otherwise in this preliminary clustering analysis, but rather the results are an indication that these analysis approaches relate differently to the state of the RV (with pressure being one aspect of the state of the RV), and that there is value in exploring the various strategies in the future to identify the workflow components and the cardiac phase information that could potentially provide the necessary information to classify functional changes throughout the course of a disease such as PH.

3.5 CONCLUSIONS

Two different statistical shape analysis workflows to assess human RV function were discussed and analyzed, including an approach that directly applies POD to harmonically mapped surfaces, and an approach that also harmonically maps the surfaces, but then projects the surfaces onto spherical harmonic functions prior to further analysis. Each step of both workflows, including the surface representation, parameterization, registration, and statistical decomposition, were elaborated upon, and the techniques were tested with a collection of human RVES. The DM-POD workflow appeared to provide surface mappings and alignments that were more anatomically consistent than the SPHARM workflow with respect to observable regions of the RV, such as the septum, free wall, pulmonary and tricuspid valves, and the apex. Additionally, the two workflows were shown to extract shape-related features that are distinctly different from one another, while the pattern analysis (shown in terms of clustering) of the patient set is closely related to both the various aspects of the workflows and the specific cardiac phase information utilized for the analysis. On average, the DM-POD workflow clustered the patient set in closer agreement with the standard clinical hemodynamic metrics in comparison to the SPHARM workflow, while the ED and other intermediate phases of the cardiac cycle produced shape features that were relatively correlated with the state of hypertension, whereas the shape of the ES phase is related to other aspects of RV function. Overall, both the DM-POD and SPHARM workflows were shown to produce features that relate distinctly to the state of the RV, and the observations herein provide a foundation for future work to determine the specific statistical shape

analysis techniques and cardiac phase components to provide the necessary information to effectively classify functional changes in the human RV.

4.0 AN IMPLEMENTATION OF INDEPENDENT COMPONENT ANALYSIS FOR 3D STATISTICAL SHAPE ANALYSIS

4.1 ABSTRACT

An implementation of the independent component analysis (ICA) technique for three-dimensional (3D) statistical shape analysis is presented. The ICA algorithm is developed based on an existing ICA algorithm, FastICA, and is generally applicable to analyze multi-dimensional and continuous functions. The capabilities of the ICA approach to uncover inherent shape features are first demonstrated through analysis of sets of artificially generated surfaces, and the nature of these features is compared to a more traditional proper orthogonal decomposition (POD) technique. For the surfaces generated, the ICA approach is shown to consistently extract surface features that closely resembled the original basis surfaces used to generate the artificial dataset, while the POD approach produces features that clearly mix the original basis. The details of an implementation of the ICA approach within a statistical shape analysis framework are then presented. Results are shown for the ICA decomposition of a collection of clinically obtained human right ventricle endocardial surfaces (RVES) segmented from cardiac computed tomography imaging, and these results are again compared with an analogous statistical shape analysis framework utilizing POD in lieu of ICA. The ICA approach is shown to produce shape features for the RVES that capture more localized variations in the shape across the set compared to the POD approach, and overall, the ICA approach produces features that represent the RVES variation throughout the set in a considerably different manner than the more traditional POD approach, providing a potentially useful alternate to statistically analyze such a set of shapes.

4.2 INTRODUCTION

Statistical shape analysis has been shown to provide a powerful means to efficiently represent a large variety of shapes for various applications, and more importantly, has been shown to be capable of providing shape-based features that can then be used to build effective metrics for classification purposes [50, 82, 83, 41, 51, 64]. In general, the key components of statistical shape analysis frameworks for classification purposes involve building a correspondence between the shapes in the given set, statistically decomposing the shape set into fundamental shape components, and then building features from the shape components that are suitable to cluster the shape set into various groupings and/or build a classifier associated with the application of interest. There have been a wide variety of techniques developed and employed within statistical shape analysis frameworks depending on the specific features, restrictions, and/or objectives of the particular applications. Furthermore, the statistical shape analysis work to-date has been largely focused on developing the mathematical representation of the shapes in a given set along with the preprocessing methods necessary to build a correspondence between these shapes, including aspects of topological mapping, shape alignment/registration, and parameterization, while much less consideration has been given to the method of statistically decomposing the shape set once this correspondence is set. The vast majority of statistical shape analysis work thus far has used some form of principal component analysis (PCA) (interchangeably referred to as proper orthogonal decomposition (POD) or by other names depending upon the specific formulation and/or application) to decompose the shape sets into fundamental components (i.e., modes or basis functions). PCA can be viewed as providing the orthogonal basis of the specific order that is optimal in the average sense for representing the given dataset. PCA has been shown to be useful in several of the examples referenced above for leading to useful shape features, and yet, PCA provides only one perspective to view the components of the shape set of interest and is subject to the constraints of its formulation (e.g., orthogonality and average L_2 optimality), which may or may not be optimally suitable for the given application.

An alternative statistical decomposition technique known as independent component analysis (ICA) was established in [52] that utilizes a considerably different approach com-

pared with PCA. Generally, ICA seeks to uncover the inherent patterns in a given signal dataset by identifying the fundamental components that can represent the dataset in a linear combination and are maximally statistically independent from one another, and in further contrast to PCA, has no requirement on the orthogonality of these modes [90, 48, 66, 16]. The derivation of ICA has been approached with several different concepts and tools, such as information maximization [9], maximum likelihood estimation [68], and utilization of artificial neural networks [18]. Furthermore, ICA has been applied to extract independent features in a diverse range of research fields, including image processing [8, 29], electroencephalogram (EEG) signal analysis [38, 31], and audio signal processing [59], among others. ICA has shown promising capabilities in terms of extracting substantially distinct features and utilizing these features for further classification purposes compared with PCA, thus leading to ICA being considered an alternative to PCA that may be preferable in some instances depending upon the application. ICA and PCA have been directly compared in several works, including applications in face recognition [42, 25] and EEG signal processing [38, 31], with ICA being preferred in some instances and PCA in others.

ICA has seen minimal application in the area of statistical shape analysis to-date, with the current contributions including [91, 87], which both sought to identify patterns related to the shape variation of cardiac structures (e.g., left and right ventricles) with two-dimensional cross-sectional analysis. Moreover, there has yet to be work considering three-dimensional (3D) statistical shape analysis with ICA. A likely contributor to the lack of work integrating ICA into 3D statistical shape analysis is the lack of the necessary ICA formulation to generally accommodate multi-dimensional and/or continuously distributed shapes (i.e., signals), with the applications thus far only considering uniformly distributed (i.e., sampled) discretized signals.

This work presents a formulation of ICA that is generally applicable for analyzing multi-dimensional continuous signals, that is appropriate for 3D statistical shape analysis. The formulation presented is focused on one particular implementation of ICA known as FastICA [46, 49], but the extensions presented could potentially be applied to other existing ICA methods as well. Sets of artificially generated shapes were analyzed to verify the ICA algorithm and the results are presented and compared with a standard PCA (i.e., POD)

algorithm. The ICA approach was then implemented within a statistical shape analysis framework (as previously reported in [94]). The shape analysis framework with ICA was applied to analyze a clinically-obtained set of 3D right ventricle endocardial surfaces, and the results are again presented in comparison to the shape analysis approach with POD as the statistical decomposition strategy to show the substantial differences in the two techniques and their outcomes as related to statistical shape analysis. Section 4.3 presents the details of the ICA algorithm developed. Section 4.4 shows the analysis of artificially generated shapes with both ICA and POD, and outlines the statistical shape analysis framework incorporating ICA along with the results of analyzing the clinically-obtained set of right ventricle endocardial surfaces with both ICA and POD, which is followed by the concluding remarks in Section 4.5.

4.3 ICA METHODS

The following formulation assumes that a given collection of n shapes to be analyzed have already been parameterized and a correspondence has been built such that $\vec{u}_i(\vec{x})$ defines the three-dimensional (3D) cartesian coordinates of the surface of the i^{th} shape in terms of the coordinates \vec{x} in the common domain of the parameterization Ω , such that $\vec{x} \in \Omega$. The fundamental assumption of ICA is that each shape function is a linear combination of m hidden (latent) statistically independent basis functions (i.e., independent components) as

$$\vec{u}_i(\vec{x}) = \sum_{j=1}^m a_{ij} \vec{s}_j(\vec{x}), \quad \text{for } i = 1, 2, \dots, n, \quad (4.1)$$

where $\{\vec{s}_j(\vec{x})\}_{j=1}^m$ is the set of m independent components and a_{ij} is the modal coefficient corresponding to the i^{th} shape and j^{th} independent component. Assuming each shape is arranged as a column vector, the entire collection of the vector-valued functions can be defined as

$$\begin{bmatrix} \vec{u}_1^T(\vec{x}) \\ \vdots \\ \vec{u}_n^T(\vec{x}) \end{bmatrix} = \begin{bmatrix} a_{11} & \cdots & a_{1m} \\ \vdots & \ddots & \vdots \\ a_{n1} & \cdots & a_{nm} \end{bmatrix} \begin{bmatrix} \vec{s}_1^T(\vec{x}) \\ \vdots \\ \vec{s}_m^T(\vec{x}) \end{bmatrix}, \quad (4.2)$$

or

$$[U] = [A][S]. \quad (4.3)$$

Therefore, to determine an estimate of the set of independent components, $[S]$, it is only necessary to estimate the left pseudoinverse of the mixing matrix, $[W] \approx [A]^{-1}$, leading to

$$[\tilde{S}] = [W][U], \quad (4.4)$$

where $[\tilde{S}]$ is used to denote the set of estimated independent components.

4.3.1 ICA Algorithm

The first challenge of any ICA algorithm is to find an effective way of quantitatively measuring statistical independence. Non-Gaussianity is commonly considered as an equivalent means to measure the independence under the Central Limit Theorem [16, 48]. In brief, the Central Limit Theorem states that the distribution of the summation of any independent random variables tends towards a Gaussian distribution as the number of random variables being summed goes to infinity. For example, the sum of two independent random variables will be more “Gaussian” than the individual random variables. Therefore, if the estimated independent components (Eqn. 4.4) are obtained under the condition of maximizing the non-Gaussianity of each component, this would theoretically lead to maximizing the separation of the independent components. There have been several methods proposed for quantitatively measuring non-Gaussianity based on various principles, including information maximization [9] and maximum likelihood estimation [68], among others. Once the measure of non-Gaussianity is defined, an optimization-based approach is typically utilized to obtain the independent components, with several algorithms having been developed for this purpose, such as the FastICA [46], JADE [13], and Infomax [54] algorithms. The FastICA algorithm is one of the most widely implemented approaches, and is therefore the approach implemented herein for 3D shape analysis and the details of this algorithm are provided in the following (additional details of the FastICA algorithm can be found in [48] and the references therein).

4.3.1.1 Centering and Whitening: The first step in the FastICA algorithm is to preprocess the dataset through centering and whitening. In the centering step the mean (i.e., expected value) is removed from the dataset, $[U]$. Defining the three components of the i^{th} shape as $\vec{u}_i(\vec{x}) = [p_i(\vec{x}), q_i(\vec{x}), r_i(\vec{x})]^T$, the expected value of each 3D shape function can be defined as

$$E[\vec{u}_i(\vec{x})] = \frac{1}{3A} \int_{\Omega} (p_i(\vec{x}) + q_i(\vec{x}) + r_i(\vec{x})) d\vec{x}, \quad (4.5)$$

where A is the area of the domain of the parameterization (i.e., $A = \int_{\Omega} d\vec{x}$). Thus, each centered 3D shape function can be calculated as

$$\vec{u}_i^c(\vec{x}) = \vec{u}_i(\vec{x}) - [E[\vec{u}_i(\vec{x})], E[\vec{u}_i(\vec{x})], E[\vec{u}_i(\vec{x})]]^T. \quad (4.6)$$

The objective of the whitening step is to linearly transform the centered dataset, $[U^c]$, so that each shape is uncorrelated with all other shapes in the transformed dataset and the variance is equal to one. To perform the whitening a standard whitening transformation algorithm, shown in [26], was implemented as follows. First, the components of the covariance matrix are defined as

$$\Sigma_{ij} = \frac{1}{A} \int_{\Omega} \vec{u}_i^c(\vec{x}) \cdot \vec{u}_j^c(\vec{x}) d\vec{x}. \quad (4.7)$$

Eigendecomposition is then applied to the covariance matrix to obtain the corresponding set of eigenvalues and eigenvectors, defining $[\lambda]$ as the diagonal matrix of eigenvalues and $[C]$ as the matrix of eigenvectors arranged columnwise. Finally, the set of whitened, centered shape functions can be calculated as

$$[\tilde{U}] = [\lambda]^{-\frac{1}{2}} [C]^T [U^c]. \quad (4.8)$$

Commonly to reduce noise and dimensionality, which may also prevent overlearning in ICA, only a subset of the whitened shape functions that correspond to the highest energy components (i.e., those corresponding to the eigenvalues with the highest relative magnitude) are retained for the following steps in the analysis [48]. One approach is to ensure that the

subset (of size k) of shape functions retained has a cumulative energy percentage that exceeds a chosen threshold, as in

$$\frac{\sum_{i=1}^k \lambda_i}{\sum_{j=1}^n \lambda_j} > \text{threshold}. \quad (4.9)$$

4.3.1.2 Maximization of Non-Gaussianity: To then determine the independent components for the centered and whitened functions the FastICA algorithm seeks solutions to the following optimization problem to maximize the non-Gaussianity of the components

$$\max_{\vec{w}_i} J(\vec{w}_i), \quad \text{for } i = 1, 2, \dots, m, \quad (4.10)$$

where

$$J(\vec{w}_i) = \left(E \left[G([\tilde{U}]^T \vec{w}_i) \right] - E[G(\vec{v})] \right)^2. \quad (4.11)$$

As such, $J(\vec{w}_i)$ is defined as the measure of non-Gaussianity for the i^{th} independent component as generated by \vec{w}_i , which are the approximations of the rows of the pseudoinverse of the mixing matrix ($[W]$ in Eqn. 4.4). \vec{v} is a three-dimensional column vector (to match the dimension of the shape functions) of Gaussian random variables with zero mean and unit variance for each component and $G()$ is a nonspecific non-quadratic function that contributes to the measure of non-Gaussianity. Since the second term in Eqn. 4.11 is independent of \vec{w}_i , the maxima of $J(\vec{w}_i)$ will correspond to either the maxima or minima of the first term in Eqn. 4.11, as in

$$\max_{\vec{w}_i} J(\vec{w}_i) = \max_{\vec{w}_i} \text{ or } \min_{\vec{w}_i} E \left[G([\tilde{U}]^T \vec{w}_i) \right]. \quad (4.12)$$

Then, constraining the magnitude of \vec{w}_i to be unity and applying the necessary condition for extrema of a function, a solution to the optimization problem can be obtained from

$$\frac{\partial}{\partial \vec{w}_i} \left(E \left[G([\tilde{U}]^T \vec{w}_i) \right] \pm \lambda (\|\vec{w}_i\|^2 - 1) \right) = \vec{0}, \quad (4.13)$$

where λ is a Lagrange multiplier and $\|\cdot\|$ is the standard l_2 -norm. Through further manipulation (see Appendix A for details) Eqn. 4.13 can be converted into

$$\frac{1}{3A} \int_{\Omega} [\tilde{U}] g([\tilde{U}]^T \vec{w}_i) d\vec{x} - \beta \vec{w}_i = \vec{0}, \quad (4.14)$$

where

$$\beta = \frac{1}{3A} \int_{\Omega} \vec{w}_i^T [\tilde{U}] g([\tilde{U}]^T \vec{w}_i) d\vec{x}, \quad (4.15)$$

and $g(x) = dG(x)/dx$. Examples of $g(x)$ that have been used in the literature [47] include

$$g(x) = x^3, \quad (4.16)$$

$$g(x) = \tanh(x), \quad (4.17)$$

or

$$g(x) = x \exp\left(-\frac{x^2}{2}\right). \quad (4.18)$$

Finally, Eqn. 4.14 can be solved approximately using Newton's method by providing an initial guess for the unknown vector \vec{w}_i (often randomly generated) and then iteratively updating the solution vector as

$$\vec{w}_i^+ = \vec{w}_i^- - [Q(\vec{w}_i^-)]^{-1} \vec{b}(\vec{w}_i^-), \quad (4.19)$$

where

$$\vec{b}(\vec{w}_i^-) = \frac{1}{3A} \int_{\Omega} [\tilde{U}] g([\tilde{U}]^T \vec{w}_i^-) d\vec{x} - \beta \vec{w}_i^-, \quad (4.20)$$

\vec{w}_i^- is the previous iteration's estimate for the solution vector and \vec{w}_i^+ is the updated estimate, and the Jacobian matrix, $[Q(\vec{w}_i^-)]$, is defined in detail in Appendix B. Substituting the approximation for the Jacobian shown in Appendix B, the update equation can be implemented in a simplified form as

$$\vec{w}_i^+ = \frac{\vec{z}}{\|\vec{z}\|} \quad (4.21)$$

with

$$\vec{z} = E \left[g'([\tilde{U}]^T \vec{w}_i^-) \right] \vec{w}_i^- - \frac{1}{A} \int_{\Omega} [\tilde{U}] g([\tilde{U}]^T \vec{w}_i^-) d\vec{x}, \quad (4.22)$$

where $g'(x) = dg(x)/dx$. Various standard measures of convergence can be implemented, and for the present work, iteration was ended when the update of the vector \vec{w}_i reached a prescribed tolerance, ϵ , as in

$$\|\vec{w}_i^+ - \vec{w}_i^-\| < \epsilon. \quad (4.23)$$

Thus, this iterative procedure can be applied to approximate several different vectors $\{\vec{w}_i\}_{i=1}^m$ to estimate the independent components as

$$\vec{s}_i(\vec{x}) = [\tilde{U}]^T \vec{w}_i. \quad (4.24)$$

In addition, to ensure that unique vectors \vec{w}_i are obtained for all m independent components (i.e., $\vec{w}_i \neq \vec{w}_j$ for $i \neq j$), a Gram-Schmidt technique [56] can be applied to further update the estimates at each Newton iteration as

$$\vec{w}_i^{++} = \vec{w}_i^+ - \sum_{j=1}^{i-1} (\vec{w}_i^{+T} \vec{w}_j) \vec{w}_j, \quad \text{for } i = 2, \dots, m. \quad (4.25)$$

Lastly, there are several approaches that have been employed to determine the number of independent components to generate, with the approach used herein being to simply generate an equivalent number of components to the size of the data subset retained after whitening [47, 66].

4.4 RESULTS AND DISCUSSION

Two sets of example analyses are presented to display the capabilities of the proposed approach for applying ICA to shape analysis. The first example set shows the analysis of collections of shapes that were artificially created through randomly generated combinations of pre-defined basis functions. This first set was intended to assess, and specifically verify the capabilities of the ICA algorithm to recover inherent features, which was highlighted by comparing the ICA results with those produced by an alternate statistical decomposition approach, POD [96]. For the second example set, the ICA algorithm was incorporated (as is outlined in Section 4.3) into a statistical shape analysis framework and applied to analyze a clinically-obtained set of human right ventricle endocardial surface (RVES) shapes. The results of the statistical shape analysis with ICA were again compared with results from the analogous framework with POD used as the method of decomposition. The primary objective of this RVES analysis was to display the nature of the results that could potentially be obtained from 3D statistical shape analysis with ICA in a clinical context, and in particular,

to assess the potential differences between this approach with ICA and the more common PCA/POD approach.

4.4.1 Decomposition of Artificially Generated Surfaces

Two sets of randomly generated surfaces were created for the verification testing process, in both cases, by defining each of the three components of the artificial shapes as a linear combination of three preselected periodic basis functions over a rectangular domain with randomly generated amplitude coefficients. The rectangular domain was chosen to match the domain of the topological mapping used in the following clinical example, such that: $x \in [0, 2\pi]$ and $y \in [0, \pi]$. All of the amplitude coefficients were randomly generated using a uniform distribution between 0 and 1. The first set of basis functions were selected to only vary in the x -coordinate of the domain, and were arbitrarily defined as two sinusoidal functions and a sawtooth function as (shown in Figs. 4.1a-c)

$$f_1(x, y) = \sin(8x), \quad (4.26)$$

$$f_2(x, y) = \sin\left(\frac{80}{7}x\right), \quad (4.27)$$

and

$$f_3(x, y) = \begin{cases} x - 0.9, & \text{for } x \in [0, 1.8] \\ x - 2.7, & \text{for } x \in (1.8, 3.6] \\ x - 4.5, & \text{for } x \in (3.6, 5.4] \\ x - 6.3, & \text{for } x \in (5.4, 2\pi] \end{cases} \quad (4.28)$$

Alternatively, the second set of basis functions were selected to be more complex than the first, with variation in both dimensions of the domain, and defined as two sinusoidal functions along with a periodic square function as (shown in Figs. 4.2a-c)

$$f_1(x, y) = \sin(8x) \cos(4y), \quad (4.29)$$

$$f_2(x, y) = \sin\left(\frac{80}{7}y\right) \cos\left(\frac{35}{6}x\right), \quad (4.30)$$

and

$$f_3(x, y) = a \cdot b, \text{ with } \begin{cases} a = 1, \text{ for } x \in [k - 1, k) \\ a = -1, \text{ for } x \in [k, k + 1) \\ b = 1, \text{ for } y \in [k - 1, k) \\ b = -1, \text{ for } y \in [k, k + 1) \\ \text{and } k = 1, 3, 5, 7 \end{cases} . \quad (4.31)$$

Datasets of three different sizes were generated randomly and tested using both basis function sets: $n = 3$, $n = 6$, and $n = 12$. In addition, for applying ICA, each of the three different g functions shown above (Eqns. 4.16-4.18) were applied in turn to obtain independent components. In all cases, the first three highest energy POD modes were retained for comparisons, while for ICA the first three data samples contained over 99% of the total energy (as defined in Eqn. 4.9) after whitening in all trials, and therefore, these three samples were used to generate three independent components for comparisons.

Figs. 4.1 and 4.2 show the three basis functions and representative examples of the first component of three randomly generated surfaces, the corresponding modes obtained by applying POD to the dataset, and the corresponding independent components obtained by applying ICA to the dataset for the two basis function sets, respectively, for the case of dataset size $n = 3$ and ICA function $g = x^3$. Overall, the modes obtained from POD can be observed to be considerably different than the independent components obtained from ICA for the cases shown, and which was indicative of the remaining (unshown) cases. Of particular significance is that other than exhibiting orthogonality, in all cases there was little that could be observed from the POD modes that would be considered significant, particularly relating to the the POD mode shapes in comparison to the basis used to generate the datasets. Although the core observation remains the same, these POD mode shapes also changed somewhat with each different dataset size tested, and in all cases the POD modes could be intuitively assessed as nothing more than mixtures of the surfaces used to generate the datasets. Alternatively, the ICA component results were consistent in appearance with every test case, including the different dataset sizes and g functions used for the implementation. Moreover, the ICA components were clearly representative of the corresponding original basis, with each of the three components having an obvious match in the set of the three

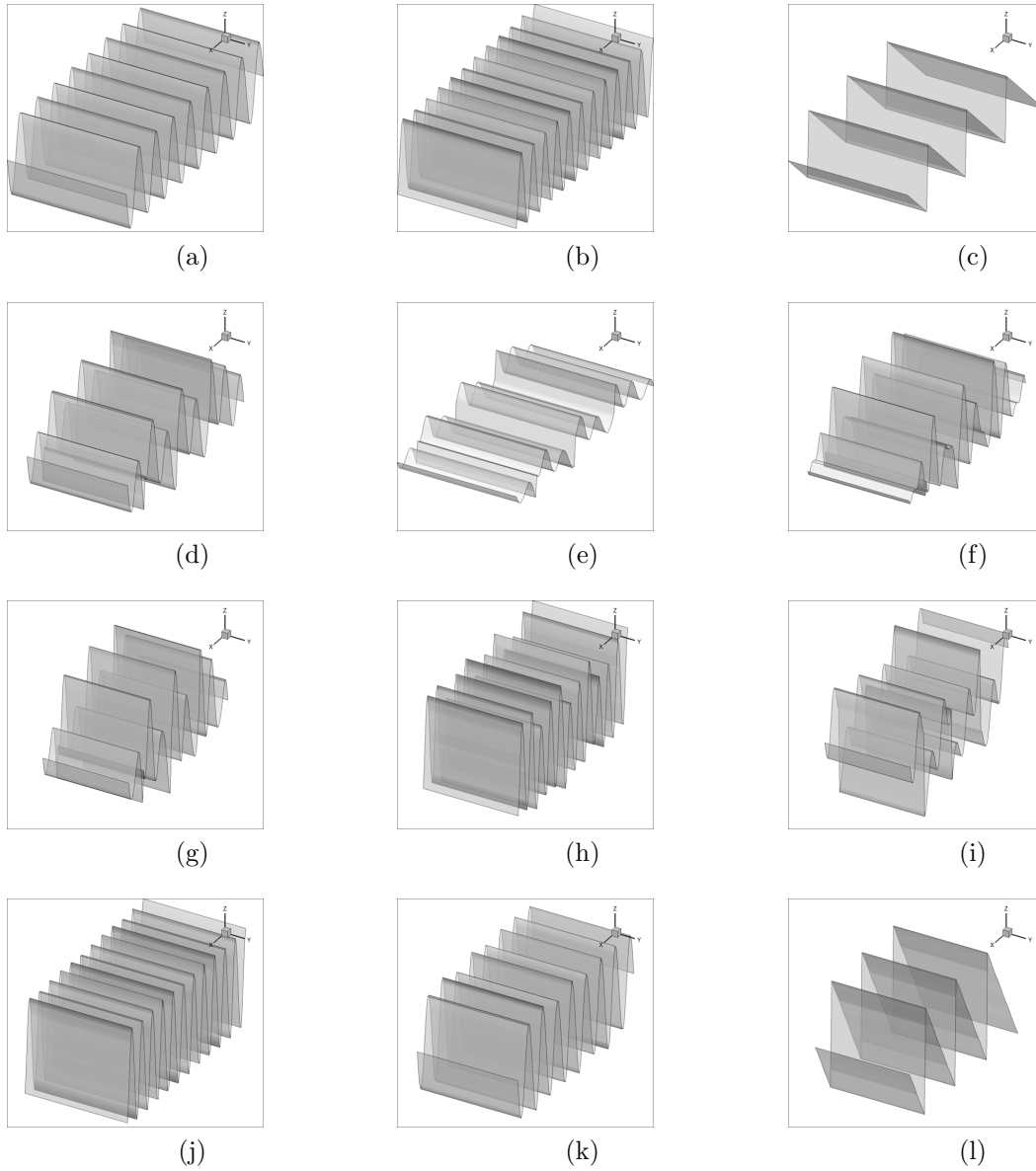


Figure 4.1: (a) - (c) The three basis functions selected to artificially generate shapes, (d) - (f) three representative examples of one component of the artificially generated shapes, (g) - (i) the first component of the three modes produced by applying proper orthogonal decomposition, and (j) - (l) the first component of the three modes produced by independent component analysis for the first example of artificially generated shapes with dataset size $n = 3$ and ICA function $g = x^3$.

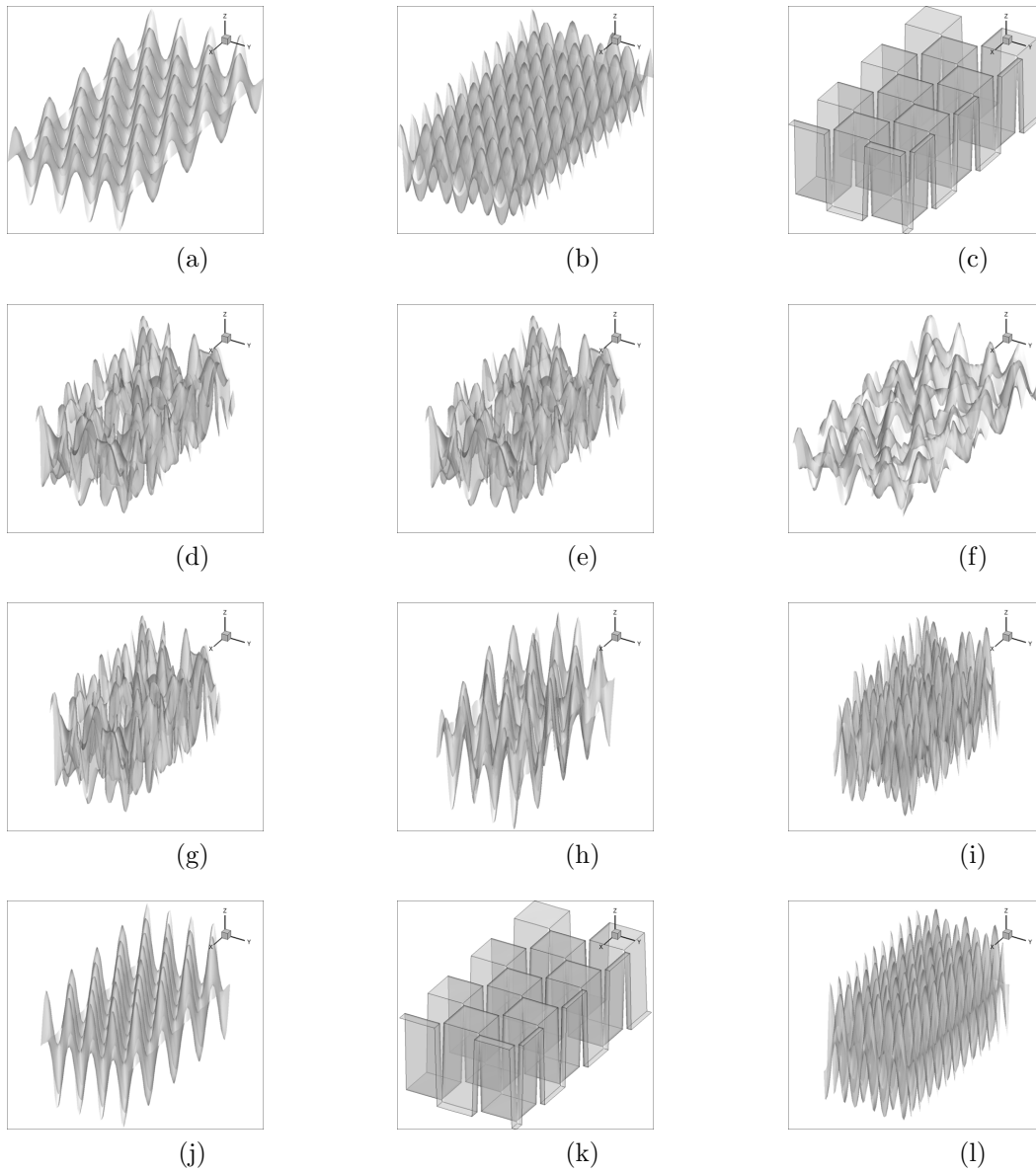


Figure 4.2: (a) - (c) The three basis functions selected to artificially generate shapes, (d) - (f) three representative examples of one component of the artificially generated shapes, (g) - (i) the first component of the three modes produced by applying proper orthogonal decomposition, and (j) - (l) the first component of the three modes produced by independent component analysis for the second example of artificially generated shapes with dataset size $n = 3$ and ICA function $g = x^3$.

basis functions used to generate the data, extracting both the relative differences in period of the sinusoidal basis functions and the relative differences in structure of the sawtooth and square function for each set of trials. While it is not possible to say how this outcome relates to pattern recognition capabilities in general, it is still significant that ICA was able to extract features from the datasets that were substantially closer to the inherent (built-in) features in the datasets in comparison to the POD approach for these specific examples (i.e., for datasets with inherent features that are not necessarily orthogonal to one another and/or related to the maximum variance in the data), without any additional information about the nature of the dataset and only a change in the fundamental assumption/constraints of the decomposition algorithm.

4.4.2 Decomposition of Human Right Ventricle Endocardial Surfaces

The human right ventricle (RV) is a well-suited application for statistical shape analysis, as it is well known to show significant shape changes due to pathology, such as pulmonary hypertension [81, 80, 79]. Moreover, the human RV has already been studied in several recent works using 3D statistical shape analysis frameworks that rely on PCA/POD for decomposition [94, 104, 60]. The following outlines one such 3D statistical shape analysis framework that was utilized herein, including the method by which ICA was incorporated to replace POD, which is then followed by analysis of a clinical dataset of human RVES.

4.4.2.1 Statistical Shape Analysis Framework: The five key steps to the statistical shape analysis approach applied herein are illustrated schematically in Fig. 4.3 and include the following:

- (a) - Segment the image stacks to obtain 3D closed surfaces describing each patient’s RVES throughout a complete cardiac cycle.
- (b) - Smooth the 3D closed surfaces and convert the surfaces into 3D meshes suitable for numerical analysis.
- (c) - Topologically map each RVES to a unified (i.e., comparable) reference state using harmonic mapping.

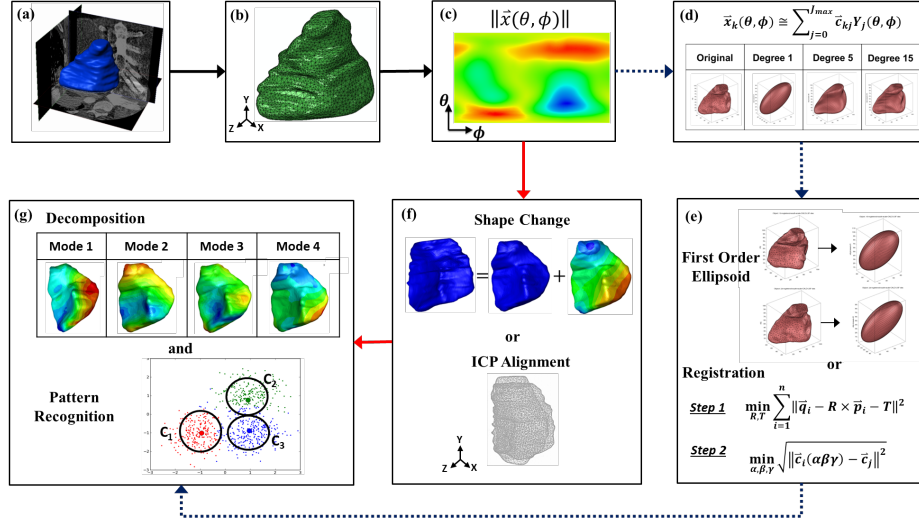


Figure 4.3: Schematic of the statistical shape analysis framework, including (a) segmentation of the image stacks, (b) smoothing and mesh generation, (c) topological mapping, (d) registration, and (e) statistical decomposition.

- (d) - Register the set of RVES shapes to remove any unwanted effects of relative size, orientation, and/or position within the set.
- (e) - Apply statistical decomposition (either POD or ICA) to the set of registered RVES to extract and rank a set of shape features (i.e., modes/components and corresponding amplitude coefficients for each patient).

Manual segmentation of the RVES was used for the present work to ensure that the most anatomically accurate representations of the ventricle shape were segmented within the constraints of the image quality. Similarly, the endocardial surface was chosen specifically due to the relatively high imaging contrast between the wall tissue and blood. The segmentation was overseen and verified by a trained cardiologist (M. A. Simon), who has over ten years of experience in advanced heart failure, PH, and in particular, experience in the imaging of the RV. The boundary of the RVES was identified in each slice in the image stacks, the slices were interpolated, and then smoothed using a standard recursive and discrete Gaussian filter within the commercial medical image processing software Simple-

ware¹ to produce each 3D, closed, non-overlapping, continuous, linearly interpolated, mesh-based representation of RVES shape. A two-step harmonic topological mapping approach was applied to map each RVES to the surface of a unit sphere so that the entire set of RVES shapes could be quantitatively described over a common domain with 3D vectors as $\{\vec{u}_k(x, y)\}_{k=1}^n$, for $x \in [0, 2\pi]$, $y \in [0, \pi]$. See [97] for additional details of the topological mapping technique and its implementation for the set of RVES. Lastly (prior to decomposition), the set of RVES were registered using an iterative closest point (ICP) rigid registration algorithm [27]. For the registration process a scaling, rotation, and translation operator were determined for each patient individually, and then those operators were applied to the RVES at each timeframe in the cardiac cycle for the corresponding patient. The scaling operator was determined so that each patient’s RVES at end diastole had the same internal cavity volume. Then the ICP algorithm was applied to determine the rotation and translation operators so that the distance between each patient’s RVES at end diastole was minimized with respect to one another.

4.4.2.2 Clinical Cardiac Dataset: The analysis described above was applied to a clinically obtained set of ECG-gated multislice cardiac CT images corresponding to 13 separate patients in varying states of hypertension from a study on regional RV structural and functional adaptation to PH as previously reported in [80]. All patients were scanned within 2 days of invasive hemodynamic measurements on either a GE Lightspeed 16-slice scanner or a GE VCT 64-slice scanner². Scan parameters were as follows: *kV* 120; *mA* approximately 400 without ECG-dose modulation; rotation time 350*msec*; pitch dependent on heart rate; 1.25*mm* slice thickness (for 16 detector scanner); *kV* 120, *mA* approximately 500 with ECG-dose modulation adjusted to peak at 65-80% R-R interval; rotation time 350*msec*; pitch dependent on heart rate; 0.625*mm* slice thickness (for 64 detector scanner). 3D RVES shapes were obtained as described above at 9 unique timeframes (approximately evenly spaced) throughout a single cardiac cycle for each of the 13 patients to produce 117 unique shapes for statistical shape analysis (i.e., $n = 117$).

¹www.simpleware.com

²(General Electric Healthcare; Milwaukee, WI, USA)

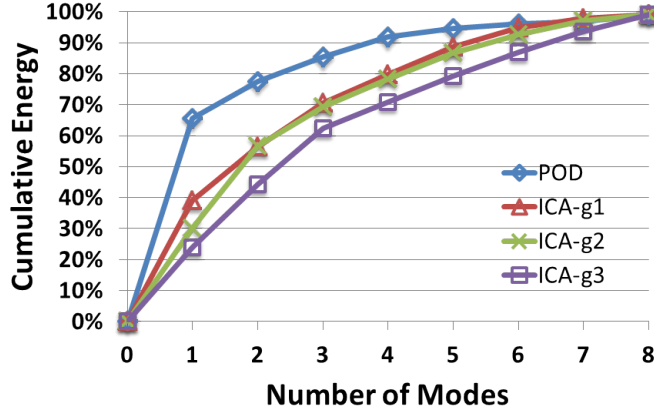


Figure 4.4: The cumulative mode/component energy for the results of the right ventricle endocardial surface analyses with proper orthogonal decomposition (POD) and independent component analysis (ICA), where $g1$ refers to $g(x) = x^3$, $g2$ refers to $g(x) = \tanh(x)$, and $g3$ refers to $g(x) = x \exp(-\frac{x^2}{2})$ as applies to the ICA algorithm presented.

4.4.2.3 Right Ventricle Endocardial Surface Decomposition Results: Both the POD and ICA approaches were implemented to decompose the collection of 117 RVES shapes within the statistical shape analysis workflow described. For the ICA approach, again all three different g functions shown in Eqns. 4.16-4.18 were applied in turn to obtain independent components. Furthermore, for all three cases of ICA only the minimum number of shapes that contained over 99% of the total energy (as described in Eqn. 4.9) were retained after whitening for generating the equivalent number of independent components.

To assess the relative significance of the individual modes/components produced by the decompositions with respect to reconstructing the RVES shapes, Fig. 4.4 shows the cumulative mode/component energy for the results of POD and the three ICA analyses with the modes ranked from highest to lowest individual contribution to the cumulative reconstruction energy. For this case, the energy of the j^{th} mode/component for reconstruction was defined as

$$Energy_j = \frac{\sum_{i=1}^n a_{ij}^2}{\sum_{k=1}^n \sum_{l=1}^m a_{kl}^2}, \quad (4.32)$$

where a_{ij} is the j^{th} modal/component coefficient to reconstruct the i^{th} RVES shape. While there are some differences in this energy distribution across the independent components depending upon the g function used in the analysis, overall, the POD modes had a significantly higher concentration of energy in the first several modes in comparison to the ICA components, which more evenly distributed the component energy over the set. Specifically, the first four POD modes exceeded 90% of the cumulative energy, whereas ICA required six components to exceed 90% cumulative energy for the first two g functions and seven components for the third g function. An interpretation of the energy distributions could be that fewer POD modes would be required to accurately reconstruct the shapes in the set in comparison to the ICA components, or in other words the POD modes provide a relatively more compact statistical model.

In order to further explore the nature of the RVES shape decompositions, Fig. 4.5 shows graphical representations of the first five modes/components obtained by the POD algorithm and the ICA algorithm with $g(x) = x^3$. Note that the component appearances and coefficient values had a similar level of variation between the ICA runs as shown for the energy distributions above, but the key conclusions in the comparison to the POD results remained consistent, and so for brevity only the one set of ICA results are shown. More specifically, Fig. 4.5 shows the mean shape computed from the dataset of 117 RVES along with plus or minus two standard deviations of each of the five modal/component coefficients multiplied with the corresponding mode/component shape and added to the mean shape (i.e., $\vec{\mu}(x, y) \pm \sigma_j \vec{s}_j(x, y)$), while the color contours represent the respective magnitude of the modal/component coefficients multiplied with the corresponding mode/component shape (i.e., $\|\sigma_j \vec{s}_j(x, y)\|$) normalized with respect to the maximum value (i.e., the magnitude of shape change introduced by each mode/component). While there is little obvious clinically-relevant anatomical significance that can be inferred from observation of either set of modes/components at this stage of research, there is certainly significant physical differences in the modes that were obtained by POD compared to the components produced by ICA. For instance, the first POD mode appears to exhibit a relatively broad change in shape somewhat concentrated in the area of the tricuspid valve, while there is no ICA component that is particularly similar to this behavior, and the first ICA component appears to exhibit

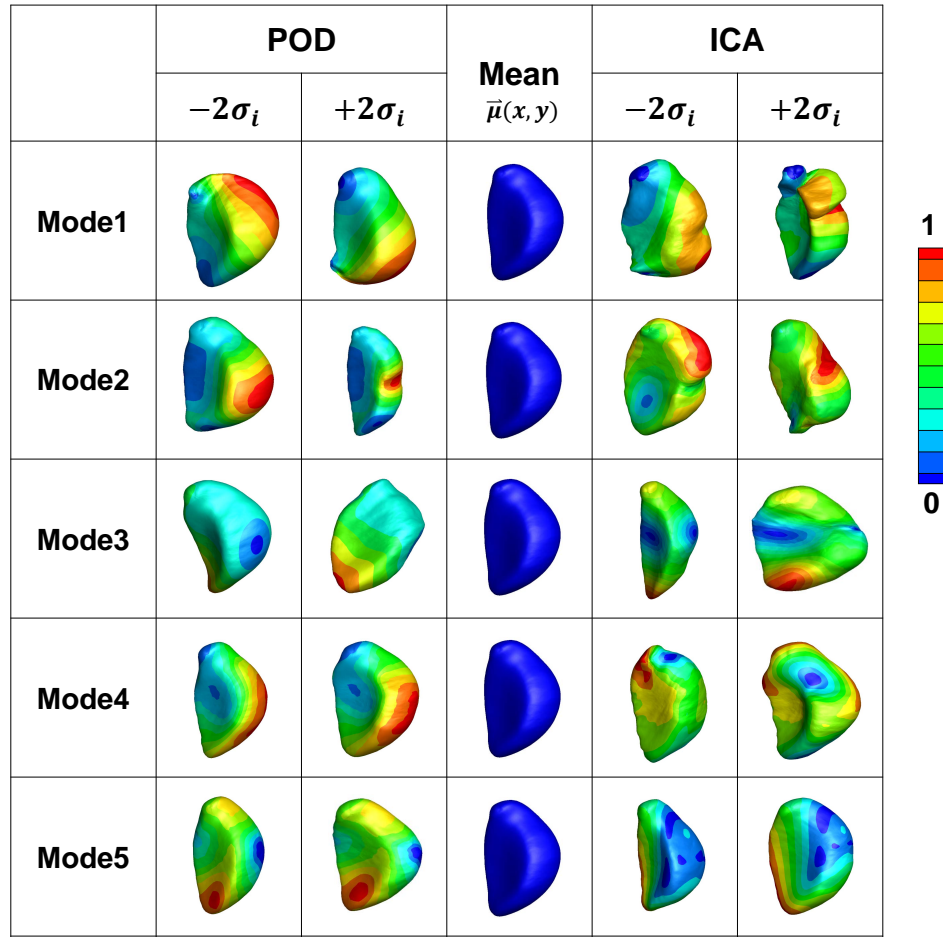


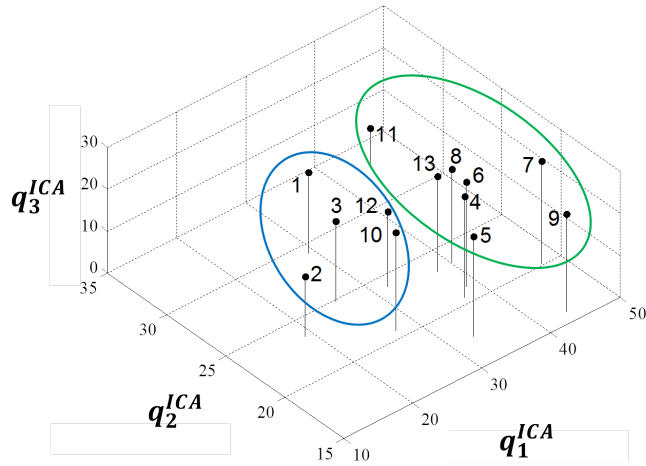
Figure 4.5: The mean shape for the right ventricle endocardial surface dataset and plus or minus two standard deviations of each of the first five modal/component coefficients multiplied with the corresponding mode/component shape and added to the mean shape ($+2\sigma$ and -2σ , respectively) for both the proper orthogonal decomposition (POD) and independent component analysis (ICA) results with $g(x) = x^3$ (the color contours represent the relative magnitude of the modal/component coefficients multiplied with the corresponding mode/component shape).

a substantially more concentrated shape variation between the tricuspid valve and the pulmonary valve. Overall, these highest-energy POD modes appear to capture shape variations that are more broadly and smoothly distributed over the RVES in comparison to the more concentrated (often with multiple areas of concentration) local shape variations captured by the ICA components. Again, note that for different g functions the appearance of the ICA components had some degree of variation. However, there were certain components that were clearly common amongst the runs with the three different g functions, and in practice, a multi run ICA approach (as shown in [66]) could be a logical next step for determining the “final” set of independent components for further analysis.

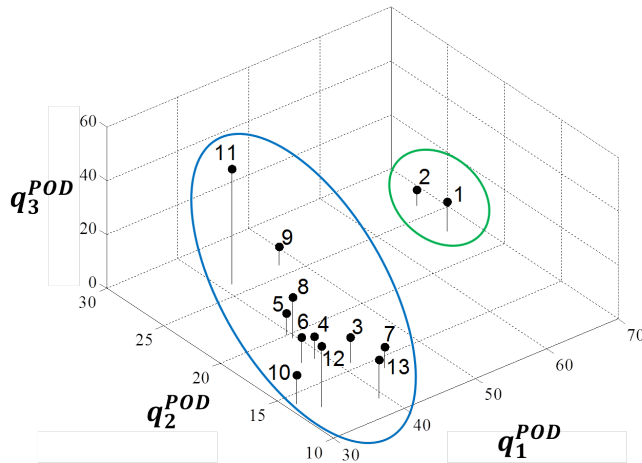
Lastly, analysis was performed to understand how the POD and ICA modes/components differently differentiate the patients in the dataset, as could be significant in a potential classification application. As such, two different methods were considered for defining features for the patients within the dataset based upon measures of the modal/coefficient energies (similar to those shown in [94]), and their respective distributions were examined. For brevity, results are again only shown for the ICA algorithm with $g(x) = x^3$ in comparison to POD. For the first test, the first three highest energy modes/components (i.e., those with the largest contribution to the RVES shapes over the entire patient set) were chosen and a feature vector (\vec{q}) was defined for each of the 13 patients separately such that the components were each of the three modes’ coefficients over the cardiac cycle for a given patient (i.e., all nine coefficients for the corresponding mode) squared and summed as

$$\vec{q} = \left[\left(\sum_{k=1}^9 a_{k1}^2 \right)^{\frac{1}{2}}, \left(\sum_{k=1}^9 a_{k2}^2 \right)^{\frac{1}{2}}, \left(\sum_{k=1}^9 a_{k3}^2 \right)^{\frac{1}{2}} \right]^T, \quad (4.33)$$

Fig. 4.6 shows the distribution of the components of this \vec{q} feature vector for the 13 patients considered herein using both the POD modes and ICA components, as well as the respective groupings that could be formed by applying K-means clustering to the feature vector to group the patient set into two groups (two groups having been arbitrarily chosen for the sake of illustration). There are clear differences between the representation of the patient set when using ICA in comparison to POD in terms of the overall distributions of the feature vectors, and more importantly, producing significantly different clustering outcomes for the



(a)



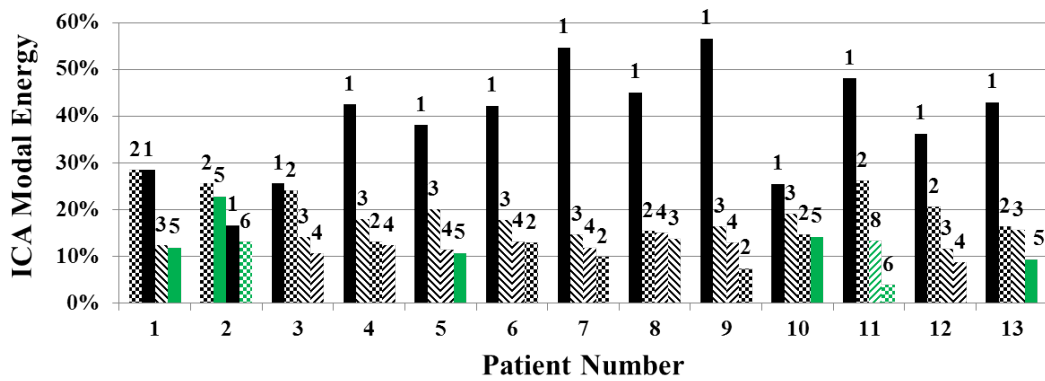
(b)

Figure 4.6: The distributions of the components of the modal/component energy feature vector (\vec{q}) defined in Eqn. 4.33 and the two groupings (circled) of the 13 patient set obtained from applying K-means clustering for the results of the right ventricle endocardial surface analyses with (a) independent component analysis (ICA) with $g(x) = x^3$ and (b) proper orthogonal decomposition (POD).

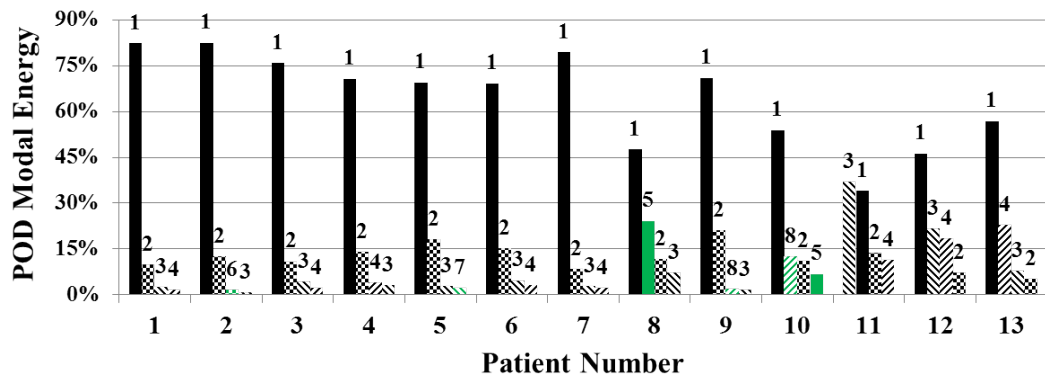
patients. Most obviously, the POD features clustered the data far more inequitably by number of patients (one grouping of 11 and the other of 2 patients) compared to the ICA features (one grouping of 8 and the other of 5 patients). In particular, the ICA features distributed patients 1 and 2 in the same group as patients 3, 10, and 12, while those two sets of patients are particularly far apart in the space of the POD features. Alternatively, for the second test, the modal/component energy for each mode was calculated separately for each individual patient as

$$\frac{\sum_{k=1}^9 a_{ki}^2}{\sum_{j=1}^m \sum_{k=1}^9 a_{kj}^2} \times 100\%, \text{ for } i = 1, 2, \dots, m, \quad (4.34)$$

Fig. 4.7 shows this relative individual modal energy for the first five highest energy modes over the cardiac cycle corresponding to each individual in the 13 patient set. Note that the mode numbering in the plot is still based on the energy of all patients combined, which is consistent with the numbering used in all of the previous results presented herein. As before, substantial differences can be observed in how these POD modal energies are distributed in comparison to the ICA component energies for the same patient set. While for both approaches the first (overall) mode/component was most significant for almost all of the 13 patients individually, the overall dominance of this first mode was substantially greater for the POD case in comparison with the ICA case, and as expected, the overall individual energy distributions were more dispersed over multiple modes for the ICA results. In addition, in terms of comparisons between patients in the set, the POD results display a significant relative similarity between patients 1 – 7 in terms of the relative individual energy distributions, whereas the ICA results would imply that patients 1 – 3 are significantly different from the rest of the patient set while patients 4 – 7 and 9 are more similar in terms of these shape-based features. In general, based on all of these preliminary results for the RVES analysis the two approaches to decompose the cardiac shape information can be seen to quite differently define the variations in function of the human RV, particularly for this set of patients that would be expected to have noticeable differences related to the varying hemodynamic states. This is a particularly nontrivial outcome when considering



(a)



(b)

Figure 4.7: Relative individual modal/component contribution (energy percentage) for the first five highest energy modes/components over the cardiac cycle for each of the 13 patients from the results of the right ventricle endocardial surface analyses with (a) independent component analysis (ICA) and (b) proper orthogonal decomposition (POD).

the need in many clinical applications to identify new features relating to pathology such as PH, that is well known to change RV function, but no clear feature has emerged leading to better understanding of these changes and/or to build clinically-applicable diagnostic tools for accurate prediction of patient outcomes. Moreover, while work has shown that statistical shape analysis with POD has potential to identify what are yet to be understood changes in RV function due to PH [94], the results herein provide evidence in the value of considering both POD and ICA for the decomposition process to provide substantially different metrics relating to the changes in heart function due to pathology, as research in this area moves forward and as more patient information becomes available.

4.5 CONCLUSIONS

An approach was presented to extend the FastICA algorithm for applications to multi-dimensional continuous functions, particularly relating to incorporation within statistical shape analysis frameworks. The capabilities of this ICA approach were shown through two sets of example analyses, a set of artificially generated shapes and a set of clinically obtained human RVES, and both analysis sets were compared to the same analysis procedure, but with the ICA portion replaced with the more traditional POD/PCA approach. The analysis of the artificially generated shape sets showed that for certain signal types (such as signals of the type considered herein), the ICA approach may be better suited for extracting inherent shape features in comparison with the POD approach. Similarly, when applied to analyze the set of human RVES, the ICA approach was shown to extract considerably different shape components than the POD approach, particularly in terms of the localizations. More significantly, the shape components produced by ICA were shown to provide features that can lead to substantially different representations of the RVES set in comparison to the analogous features produced by POD. By providing an alternate means to represent changes in the function of a biological structure throughout a clinical dataset, such as that considered here, the ICA approach is expected to provide a worthwhile alternate for consideration in applications of statistical shape analysis in medicine, among other potential applications.

5.0 CURRENT CAPABILITIES AND FUTURE DIRECTIONS

A statistical shape analysis framework has been developed and verified to perform quantitative analysis and statistical decomposition of sets of 3D genus-0 shapes. The analysis procedure consists in a two-step surface parameterisation technique, two alignment/registration algorithm (i.e., pseudo-displacement and iterative closest point), followed by two statistical decomposition methods – proper orthogonal decomposition (POD) or independent component analysis (ICA).

The framework is capable of recovering shape features for classifying shape clusters with the inherent patterns, and is proven to be particularly well suited for applications in medical image analysis. With the implementation on the human right ventricle, the framework is shown to be anatomically consistent, allows direct comparison across populations of individuals, and potentially provides new metrics to improve the diagnosis and understanding of a specific cardiovascular disease known as pulmonary hypertension (PH). Particularly in comparison to traditional clinical metrics, the newly obtained metrics are shown to be consistent and converging towards intrinsically physiological components for the heart, and may potentially produce a novel means for classifying the progressive change in RV function caused by PH.

In comparison with an existing statistical shape analysis method – the spherical harmonic method (SPHARM) for human right ventricular functional behavior assessment, the metrics derived from the developed framework produces more accurate hypertension classification results. Above all, the built framework provides a means to better understand RV function and functional changes in the RV due to PH with the long-term potential capability to produce clinical tools to assist in predicting patient outcomes and/or the effects of therapies. Moreover, the approach has near-universal applicability to analyze many other pathological

conditions as they are related to changes in the shape of biological structures that can be measured from various medical imaging modalities.

However, certain extensions need to be made in order for the framework to be clinically applicable in general. The computational framework can be upgraded to be completely automatic or semi-automatic by incorporating automation of segmentation and feature extraction, and therefore universally applicable to analyze a broader range of organ-level shapes by incorporating sophisticated methods for parameterization and registration. As such, the automated framework could be used to carry on shape and kinematics analysis of RV or other biological structures with much larger medical image datasets. Furthermore, the framework could be used to analyze the evolution of certain biological diseases with sufficient longitudinal medical imaging data. One possible implementation is to study the evolution of cancer, as well as to assess the treatment response in different cancers based on geometric features. Since one significant feature of cancer is that it grows quickly in a relatively short amount of time. The derived statistically significant features could potentially lead to novel criteria to quantitatively evaluate biological function and assess disease-related deterioration and treatment effects.

A more comprehensive biological structure model could be established to better simulate the *in vivo* physical activity. Instead of addressing the diagnostic challenges from individual perspective, the comprehensive model will interact with other available information from various up-to-date disciplines, which could include mechanical behaviors and material properties. One possible research direction is to couple all the available information together. Since the geometry of biological structures can be obtained from the developed method, it will be convenient to map the mechanical behavior and material property to the corresponding location. Compared with the existing method, the model would quite likely lead to a more accurate understanding of the biological functions. Another potential research direction is to use the derived geometric features as a validation method to evaluate the performance of other existing methods. The geometric method can be considered as a gold standard, since it is based solely on the *in vivo* information directly from medical imaging. With improved understanding, more accurate results could be obtained to better diagnose diseases and ultimately may lead to the development of novel and effective treatments.

APPENDIX A

INDEPENDENT COMPONENT ANALYSIS - DERIVATION OF NON-GAUSSIANITY MAXIMIZATION

Recall that the implementation of the necessary condition for extrema of a function to maximize the non-Gaussianity of the independent components (Eqn. 4.13 in Section 4.3.1.2) requires the calculation of the following gradient

$$\frac{\partial}{\partial \vec{w}_i} \left(E \left[\left(G(\vec{w}_i^T [\tilde{U}]) \right)^T \right] \pm \lambda (\|\vec{w}_i\|^2 - 1) \right) = \vec{0}. \quad (\text{A.1})$$

Differentiating, applying the definition of the expected value (Eqn. 4.5), and simplifying, the gradient can be rewritten as

$$\frac{1}{3A} \int_{\Omega} [\tilde{U}] g([\tilde{U}]^T \vec{w}_i) d\vec{x} \pm 2\lambda \vec{w}_i = \vec{0}, \quad (\text{A.2})$$

An arbitrary constant β can then be defined such that $-\beta = \pm 2\lambda$, and the gradient equation becomes

$$\frac{1}{3A} \int_{\Omega} [\tilde{U}] g([\tilde{U}]^T \vec{w}_i) d\vec{x} - \beta \vec{w}_i = \vec{0}, \quad (\text{A.3})$$

Lastly, β can be explicitly calculated by taking the dot product of the gradient equation with \vec{w}_i to produce

$$\frac{1}{3A} \int_{\Omega} \vec{w}_i^T [\tilde{U}] g([\tilde{U}]^T \vec{w}_i) d\vec{x} - \beta \vec{w}_i^T \vec{w}_i = 0, \quad (\text{A.4})$$

and noting that \vec{w}_i is constrained to be a unit vector, β can be calculated as

$$\beta = \frac{1}{3A} \int_{\Omega} \vec{w}_i^T [\tilde{U}] g([\tilde{U}]^T \vec{w}_i) d\vec{x}, \quad (\text{A.5})$$

APPENDIX B

INDEPENDENT COMPONENT ANALYSIS - CALCULATION OF JACOBIAN MATRIX

As is standard, the Jacobian matrix $([Q(\vec{w})])$ necessary for the Newton iterations outlined in Section 4.3.1.2 is defined as the gradient of the residual vector (Eqn. 4.20) with respect to the vector to be updated for the approximation (\vec{w}) as

$$[Q(\vec{w})] = \frac{\partial}{\partial \vec{w}} \left(\frac{1}{3A} \int_{\Omega} [\tilde{U}] g([\tilde{U}]^T \vec{w}) d\vec{x} - \beta \vec{w} \right). \quad (\text{B.1})$$

The definition of the Jacobian matrix can be expanded and shown in indicial form as

$$Q_{jk} = \frac{1}{3A} \int_{\Omega} \left[\sum_{l=1}^3 g' \left(\sum_{i=1}^n \tilde{U}_{il} w_i \right) \tilde{U}_{jl} \tilde{U}_{kl} \right] d\vec{x} - \beta \delta_{jk}, \quad (\text{B.2})$$

where $g'(x) = dg(x)/dx$ and δ_{jk} is the standard Kronecker delta. Then, by assuming that the g' terms are all reasonably approximated by the constant mean of the three components over the integral domain (and returning to the matrix-vector form), the Jacobian matrix can be approximated with the simplified form

$$[Q(\vec{w})] = E \left[g'([\tilde{U}]^T \vec{w}) \right] \left(\frac{1}{3A} \int_{\Omega} [\tilde{U}][\tilde{U}]^T d\vec{x} \right) - \beta [I], \quad (\text{B.3})$$

and since the data $([\tilde{U}])$ has already been whitened based on Eqn. 4.7, the Jacobian matrix can be simplified even further to

$$[Q(\vec{w})] = \left(\frac{1}{3} E \left[g'([\tilde{U}]^T \vec{w}) \right] - \beta \right) [I], \quad (\text{B.4})$$

where $[I]$ is the $n \times n$ identity matrix.

APPENDIX C

PROPER ORTHOGONAL DECOMPOSITION FOR VECTOR-VALUED FUNCTIONS

C.1 OBJECTIVE

Apply the proper orthogonal decomposition (POD) method to derive the fundamental shape features of a collection of three-dimensional closed surfaces. Each surface is represented by a three-dimensional displacement function:

$$\vec{u}(\vec{x}) = [u_1(x_1, x_2, x_3), u_2(x_1, x_2, x_3), u_3(x_1, x_2, x_3)]^T, \quad (\text{C.1})$$

which defines the deformation of the surface of a unit sphere into the given shape.

C.2 METHODS

The main intention of using POD for this work is to obtain the fundamental shape features by defining these features as those that form the optimal basis of shapes (i.e. closed surfaces) to represent a previously obtained collection (i.e. set of snapshots) of n surfaces $\{\vec{u}_k(\vec{x})\}_{k=1}^n \in V(S_1)$, where the vector spaces are defined as $V(S_1) = \{\vec{u}(\vec{x}) : u_i(\vec{x}) \in L_2 \text{ for } i = 1, 2, 3, \vec{x} \in S_1\}$ and $S_1 = \{\vec{x} \in \mathbf{R}^3 : \sqrt{x_1^2 + x_2^2 + x_3^2} = 1\}$ (i.e. the unit sphere domain), and L_2 is the standard definition for the Hilbert space. This optimal basis is defined as that which minimizes the average of the norm of the difference between each snapshot and the

best approximation of the basis to the snapshot, which leads to the following optimization problem:

$$\min_{\{\vec{v}_i(\theta, \phi)\}_{i=1}^m \in V(S_1)} \langle \|\vec{u}_k(\theta, \phi) - \vec{u}_k^*(\theta, \phi)\|_{L_2}^2 \rangle, \quad (\text{C.2})$$

where $\{\vec{\phi}_i(\vec{x})\}_{i=1}^m$ is the set of m basis functions (i.e., POD modes), $\vec{u}_k(\vec{x})$ is the k^{th} snapshot surface function, $\vec{u}_k^*(\vec{x})$ is the best approximation of the basis to the k^{th} snapshot, and the norm and averaging operators are defined respectively as: $\|\vec{u}(\vec{x})\| = (\vec{u}(\vec{x}), \vec{u}(\vec{x}))^{1/2}$, with $(\vec{u}(\vec{x}), \vec{v}(\vec{x})) = \int_{S_1} \vec{u}(\vec{x}) \cdot \vec{v}(\vec{x}) d\vec{x}$ and $\langle u_k \rangle = \frac{1}{n} \sum_{k=1}^n u_k$.

For an orthogonal basis the best approximation to a snapshot can be found by the projection of that snapshot onto the basis, which is defined as:

$$\vec{u}_k^*(\vec{x}) = \sum_{i=1}^m \frac{(\vec{\phi}_i(\vec{x}), \vec{u}_k(\vec{x}))}{\|\vec{\phi}_i(\vec{x})\|^2} \vec{\phi}_i(\vec{x}). \quad (\text{C.3})$$

The optimization problem can be manipulated with the following steps:

$$\begin{aligned} \langle \|\vec{u}_k(\theta, \phi) - \vec{u}_k^*(\theta, \phi)\|^2 \rangle &= \langle \|\vec{u}_k(\theta, \phi)\|^2 - 2(\vec{u}_k(\theta, \phi), \vec{u}_k^*(\theta, \phi)) + \|\vec{u}_k^*(\theta, \phi)\|^2 \rangle \\ &= \langle \|\vec{u}_k(\theta, \phi)\|^2 - 2 \sum_{i=1}^m \frac{(\vec{\phi}_i(\vec{x}), \vec{u}_k(\vec{x}))}{\|\vec{\phi}_i(\vec{x})\|^2} (\vec{\phi}_i(\vec{x}), \vec{u}_k(\vec{x})) + \sum_{i=1}^m \frac{(\vec{\phi}_i(\vec{x}), \vec{u}_k(\vec{x}))^2}{\|\vec{\phi}_i(\vec{x})\|^2} \rangle. \end{aligned} \quad (\text{C.4})$$

Therefore

$$\min_{\{\vec{v}_i(\theta, \phi)\}_{i=1}^m \in V(S_1)} \langle \|\vec{u}_k(\theta, \phi) - \vec{u}_k^*(\theta, \phi)\|^2 \rangle = \min_{\{\vec{v}_i(\theta, \phi)\}_{i=1}^m \in V(S_1)} \langle \|\vec{u}_k(\theta, \phi)\|^2 - \sum_{i=1}^m \frac{(\vec{\phi}_i(\vec{x}), \vec{u}_k(\vec{x}))^2}{\|\vec{\phi}_i(\vec{x})\|^2} \rangle. \quad (\text{C.5})$$

Then, minimizing for each i individually, neglecting the term $\|\vec{u}_k(\vec{x})\|^2$ as it is independent of the basis functions, and forcing the basis to be orthonormal using a Lagrange multiplier the minimization problem can be converted into the following maximization problem:

$$\max_{\{\vec{v}_i(\theta, \phi)\}_{i=1}^m \in V(S_1)} J(\vec{\phi}_i(\vec{x})), \quad (\text{C.6})$$

where

$$J(\vec{\phi}_i(\vec{x})) = \langle (\vec{u}_k(\vec{x}), \vec{\phi}_i(\vec{x}))^2 \rangle - \lambda(\|\vec{\phi}_i(\vec{x})\|^2 - 1). \quad (\text{C.7})$$

The necessary condition for extrema of a functional (Gateaux derivative) can also be applied as:

$$\lim_{\varepsilon \rightarrow 0} \frac{d}{d\varepsilon} J(\vec{\phi}_i(\vec{x}) + \varepsilon \vec{\Psi}(\vec{x})) = 0, \forall \vec{\Psi}(\vec{x}) \in V(S_1), \quad (\text{C.8})$$

and the equations processed further to convert the optimization problem into a continuous eigenvalue problem as:

$$J(\vec{\phi}_i(\vec{x}) + \varepsilon \vec{\Psi}(\vec{x})) = \frac{1}{n} \sum_{k=1}^n [(\vec{u}_k(\vec{x}), \vec{\phi}_i(\vec{x})) + \varepsilon (\vec{u}_k(\vec{x}), \vec{\Psi}(\vec{x}))]^2 - \dots \\ \dots \lambda (\|\vec{\phi}_i(\vec{x})\|^2 + 2\varepsilon (\vec{\phi}_i(\vec{x}), \vec{\Psi}(\vec{x})) + \varepsilon^2 \|\vec{\Psi}(\vec{x})\|^2) - \lambda. \quad (\text{C.9})$$

and

$$\left[\frac{d}{d\varepsilon} J(\vec{\phi}_i(\vec{x}) + \varepsilon \vec{\Psi}(\vec{x})) \right]_{\varepsilon=0} = \frac{1}{n} \sum_{k=1}^n [(\vec{u}_k(\vec{x}), \vec{\phi}_i(\vec{x})) (\vec{u}_k(\vec{x}), \vec{\Psi}(\vec{x}))] - \lambda (\vec{\phi}_i(\vec{x}), \vec{\Psi}(\vec{x})) \\ = \frac{1}{n} \sum_{k=1}^n \left[\int_{S_1} \vec{u}_k(\vec{x}) \cdot \vec{\phi}_i(\vec{x}) d\vec{x} \int_{S_1} \vec{u}_k(\vec{\xi}) \cdot \vec{\Psi}(\vec{\xi}) d\vec{\xi} - \lambda \int_{S_1} \vec{\phi}_i(\vec{\xi}) \cdot \vec{\Psi}(\vec{\xi}) d\vec{\xi} \right] \quad (\text{C.10})$$

Therefore,

$$\int_{S_1} \vec{\Psi}(\vec{\xi}) \cdot \left[\frac{1}{n} \sum_{k=1}^n \vec{u}_k(\vec{\xi}) \int_{S_1} \vec{u}_k(\vec{x}) \cdot \vec{\phi}_i(\vec{x}) d\vec{x} \right] d\vec{\xi} = 0 \quad \forall \vec{\Psi}(\vec{x}) \in V(S_1) \\ \frac{1}{n} \sum_{k=1}^n n \int_{S_1} \vec{u}_k(\vec{\xi}) (\vec{u}_k(\vec{x}) \cdot \vec{\phi}_i(\vec{x})) d\vec{x} = \lambda \vec{\phi}_i(\vec{\xi}) \quad (\text{C.11})$$

C.3 METHOD OF SNAPSHOTS

Applying the methods of snapshot to reduce the computational expense to obtain the POD modes the inner product is taken of the above eigenvalue problem with each snapshot field $\vec{u}_k(\vec{x})$ to produce the following discrete eigenvalue problem:

$$\frac{1}{n} \sum_{k=1}^n A_{ij} C_k = \lambda C_j, \quad (\text{C.12})$$

where

$$A_{ij} = \int_{S_1} \vec{u}_j(\vec{\xi}) \cdot \vec{u}_k(\vec{\xi}) d\vec{\xi} \quad \text{and} \quad C_k = \int_{S_1} \vec{u}_k(\vec{\xi}) \cdot \vec{\phi}_i(\vec{\xi}) d\vec{\xi}. \quad (\text{C.13})$$

Finally, the i^{th} solution to the discrete eigenvalue problem can be used to determine the i^{th} POD mode as follows:

$$\vec{\phi}_i(\vec{x}) = \frac{1}{\lambda^i n} \sum_{k=1}^n \vec{u}_k(\vec{x}) C_k^i. \quad (\text{C.14})$$

An important note is that the eigenvalue of each mode will correspond to the relative importance of the mode in representing the given ensemble of snapshots. As such, the modes with the highest eigenvalues can be thought of as those that are the most significant components of the ensemble.

BIBLIOGRAPHY

- [1] A. Ben Abdallah, F. Ghorbel, K. Chatti, H. Essabbah, and M.H. Bedoui. A new uniform parameterization and invariant 3d spherical harmonic shape descriptors for shape analysis of the hearts left ventricle a pilot study. *Pattern Recognition Letters*, 31(13):1981 – 1990, 2010.
- [2] Dean Adams, F James Rohlf, and Dennis Slice. Geometric morphometrics: Ten years of progress following the revolution. *Italian Journal of Zoology*, 71(1):5–16, 2004.
- [3] Alexander Andreopoulos and John K Tsotsos. Efficient and generalizable statistical models of shape and appearance for analysis of cardiac mri. *Medical Image Analysis*, 12(3):335–357, 2008.
- [4] C. Apitz, G. D. Webb, and A. N. Redington. Tetralogy of fallot. *THE LANCET*, 374(24-30):1462–1471, 2009.
- [5] W Aquino. An object-oriented framework for reduced-order models using proper orthogonal decomposition (pod). *Computer Methods in Applied Mechanics and Engineering*, 196(41-44):4375–4390, 2007.
- [6] W Aquino, J C Brigham, C J Earls, and N Sukumar. Generalized finite element method using proper orthogonal decomposition. *International Journal for Numerical Methods in Engineering*, 79(7):887–906, 2009.
- [7] Ravi Bansal, Lawrence H Staib, Dongrong Xu, Hongtu Zhu, and Bradley S Peterson. Statistical analyses of brain surfaces using gaussian random fields on 2-d manifolds. *IEEE Transactions on Medical Imaging*, 26(1):46–57, 2007.
- [8] Marian Stewart Bartlett, Javier R Movellan, and Terrence J Sejnowski. Face recognition by independent component analysis. *IEEE Transactions on Neural Networks*, 13(6):2023–2039, 2008.
- [9] A J Bell and T J Sejnowski. An information-maximisation approach to blind separation and blind deconvolution. *Neural Computation*, 7(6):1129–1159, 1995.
- [10] Johan G Bosch, Francisca Nijland, Steven C Mitchell, Boudewijn P F Lelieveldt, Otto Kamp, Johan H C Reiber, and Milan Sonka. Computer-aided diagnosis via model-based

- shape analysis: automated classification of wall motion abnormalities in echocardiograms. *Academic Radiology*, 12(3):358–367, 2005.
- [11] C Brechbuhler, G Gerig, and O Kobler. Parameterization of closed surfaces for 3d shape description. *Computer Vision and Image Understanding*, 61:154–170, 1995.
- [12] John C Brigham and Wilkins Aquino. Inverse viscoelastic material characterization using pod reduced-order modeling in acousticstructure interaction. *Computer Methods in Applied Mechanics and Engineering*, 198(9-12):893–903, 2009.
- [13] J F Cardoso. High-order contrasts for independent component analysis. *Neural Computation*, 11(1):157–192, 1999.
- [14] D Chetverikov, D Stepanov, and P Krsek. Robust euclidean alignment of 3d point sets: the trimmed iterative closest point algorithm. *Image and Vision Computing*, 23(3):299–309, 2005.
- [15] Kelly M Chin, Nick H S Kim, and Lewis J Rubin. The right ventricle in pulmonary hypertension. *Coronary Artery Disease*, 16(1):13–18, 2005.
- [16] S. Choi, A. Cichocki, H. M. Park, and S. Y. Lee. Blind source separation and independent component analysis: a review. *Neural Inf Process-Lett Rev*, 6:1–57, 2005.
- [17] C J Chuong, M S Sacks, G Templeton, F Schwiep, and R L Johnson. Regional deformation and contractile function in canine right ventricular free wall. *American Journal of Physiology*, 260(4 Pt 2):H1224–H1235, 1991.
- [18] A Cichocki and R Unbehauen. Robust neural networks with on-line learning for blind identification and blind separation of sources, 1996.
- [19] Jay N Cohn, Roberto Ferrari, and Norman Sharpe. Cardiac remodeling concepts and clinical implications: a consensus paper from an international forum on cardiac remodeling. *Journal of the American College of Cardiology*, 35(3):569–582, 2000.
- [20] T F Cootes and C J Taylor. Statistical models of appearance for computer vision. *World Wide Web Publication February*, 2004.
- [21] Sergi G Costafreda, Ivo D Dinov, Zhuowen Tu, Yonggang Shi, Cheng-Yi Liu, Iwona Kloszewska, Patrizia Mecocci, Hilkka Soininen, Magda Tsolaki, Bruno Vellas, and et al. Automated hippocampal shape analysis predicts the onset of dementia in mild cognitive impairment. *NeuroImage*, 56(1):212–219, 2011.
- [22] G E DAlonzo, R J Barst, S M Ayres, E H Bergofsky, B H Brundage, K M Detre, A P Fishman, R M Goldring, B M Groves, and J T Kernis. Survival in patients with primary pulmonary hypertension. results from a national prospective registry. *Annals of Internal Medicine*, 115(5):343–349, 1991.

- [23] Rhodri H Davies, Carole J Twining, Timothy F Cootes, and Chris J Taylor. Building 3-d statistical shape models by direct optimization. *IEEE Transactions on Medical Imaging*, 29(4):961–981, 2010.
- [24] Kunio Doi. Computer-aided diagnosis in medical imaging: historical review, current status and future potential. *Computerized medical imaging and graphics the official journal of the Computerized Medical Imaging Society*, 31(4-5):198–211, 2007.
- [25] Bruce A Draper, Kyungim Baek, Marian Stewart Bartlett, and J Ross Beveridge. Recognizing faces with pca and ica. *Computer Vision and Image Understanding*, 91(1-2):115–137, 2003.
- [26] Richard O. Duda, Peter E. Hart, and David G. Stork. *Pattern Classification*. Wiley, New York, 2. edition, 2001.
- [27] Rsj Estpar and Anders Brun. Robust generalized total least squares. *Medical Image Computing and Computer-Assisted Intervention - MICCAI 2004*, pages 234–241, 2004.
- [28] Luca Ferrarini, Hans Olofsen, Walter M Palm, Mark A Van Buchem, Johan H C Reiber, and Faiza Admiraal-Behloul. Games: growing and adaptive meshes for fully automatic shape modeling and analysis. *Medical Image Analysis*, 11(3):302–314, 2007.
- [29] Simone Fiori. Overview of independent component analysis technique with an application to synthetic aperture radar (sar) imagery processing. *Neural Networks*, 16(3-4):453–467, 2003.
- [30] Michael S Floater and Kai Hormann. Surface parameterization : a tutorial and survey. *Advances in multiresolution for geometric modelling*, 1(c):157–186, 2005.
- [31] F La Foresta, F C Morabito, B Azzerboni, and M Ipsale. Pca and ica for the extraction of eeg components in cerebral death assessment, 2005.
- [32] A F Frangi, W J Niessen, and M A Viergever. Three-dimensional modeling for functional analysis of cardiac images: a review. *IEEE Transactions on Medical Imaging*, 20(1):2–25, 2001.
- [33] Alejandro F Frangi, Daniel Rueckert, Julia A Schnabel, and Wiro J Niessen. Automatic construction of multiple-object three-dimensional statistical shape models: application to cardiac modeling. *IEEE Transactions on Medical Imaging*, 21(9):1151–1166, 2002.
- [34] G Gerig, M Styner, D Jones, D Weinberger, and J Lieberman. Shape analysis of brain ventricles using spharm. *Proceedings IEEE Workshop on Mathematical Methods in Biomedical Image Analysis MMBIA 2001*, pages 171–178, 2001.
- [35] G Gerig, M Styner, M E Shenton, and J A Lieberman. *Shape versus size: improved understanding of the morphology of brain structures*, volume 2208, pages 24–32. Springer, 2001.

- [36] C Goodall. Procrustes methods in the statistical analysis of shape. *Journal of the Royal Statistical Society Series B Methodological*, 53(2):285–339, 1991.
- [37] C Gotsman, X Gu, and A Sheffer. Fundamentals of spherical parameterization for 3d meshes. *ACM Transactions on Graphics*, 22(3):358, 2003.
- [38] M I Gursoy and A Subast. A comparison of pca, ica and lda in eeg signal classification using svm, 2008.
- [39] B Gutman, T E Chan, and P M Thompson. Hippocampal surface analysis using spherical harmonic function applied to surface conformal mapping. *18th International Conference on Pattern Recognition (2006)*, 00(c):964–967, 2006.
- [40] I Haber, D N Metaxas, and L Axel. Three-dimensional motion reconstruction and analysis of the right ventricle using tagged mri. *Medical Image Analysis*, 4(4):335–355, 2000.
- [41] Tobias Heimann and Hans-Peter Meinzer. Statistical shape models for 3d medical image segmentation: a review. *Medical Image Analysis*, 13(4):543–563, 2009.
- [42] C Heshner, A Srivastava, and G Erlebacher. A novel technique for face recognition using range imaging, 2003.
- [43] Heng Huang, Li Shen, Rong Zhang, Fillia Makedon, Bruce Hettleman, and Justin Pearlman. Surface alignment of 3d spherical harmonic models: application to cardiac mri analysis. *Medical Image Computing and Computer-Assisted Intervention*, 8(Pt 1):67–74, 2005.
- [44] Heng Huang, Li Shen, Rong Zhang, Fillia Makedon, Bruce Hettleman, and Justin Pearlman. Cardiac motion analysis to improve pacing site selection in crt. *Academic Radiology*, 13(9):1124–1134, 2006.
- [45] Alexandra Hyduk, Janet B Croft, Carma Ayala, Kan Zheng, Zhi-Jie Zheng, and George A Mensah. Pulmonary hypertension surveillance—united states, 1980-2002. *MMWR Surveillance summaries Morbidity and mortality weekly report Surveillance summaries CDC*, 54(5):1–28, 2005.
- [46] Aapo Hyv and Erkki Oja. A fast fixed-point algorithm for independent component analysis 1 introduction. *Most*, 9(7):1–10, 1997.
- [47] A. Hyvärinen, J. Karhunen, and E. Oja. *Independent Component Analysis*. Wiley, New York, 1. edition, 2001.
- [48] A. Hyvärinen and E. Oja. Independent component analysis: Algorithms and applications. *Neural Networks*, 13(4-5):411–430, 2000.
- [49] A Hyvrinen. Fast and robust fixed-point algorithms for independent component analysis. *IEEE Transactions on Neural Networks*, 10(3):626–634, 1999.

- [50] A K Jain and P W Duin. Statistical pattern recognition: a review. *IEEE Transactions on Pattern Analysis and Machine Intelligence*, 22(1):4–37, 2000.
- [51] Sarang Joshi, Stephen Pizer, P Thomas Fletcher, Paul Yushkevich, Andrew Thall, and J S Marron. Multiscale deformable model segmentation and statistical shape analysis using medial descriptions. *IEEE Transactions on Medical Imaging*, 21(5):538–550, 2002.
- [52] C Jutten and J Herault. Blind separation of sources, part i: An adaptive algorithm based on neuromimetic architecture. *Signal Processing*, 24(1):1–10, 1991.
- [53] Sun Hyung Kim, Jong-Min Lee, Hyun-Pil Kim, Dong Pyo Jang, Yong-Wook Shin, Tae Hyon Ha, Jae-Jin Kim, In Young Kim, Jun Soo Kwon, and Sun I Kim. Asymmetry analysis of deformable hippocampal model using the principal component in schizophrenia. *Human Brain Mapping*, 25(4):361–369, 2005.
- [54] T W Lee, M Girolami, and T J Sejnowski. Independent component analysis using an extended infomax algorithm for mixed subgaussian and supergaussian sources. *Neural Computation*, 11(2):417–441, 1999.
- [55] Olof Lindberg, Mark Walterfang, Jeffrey C L Looi, Nikolai Malykhin, Per stberg, Bram Zandbelt, Martin Styner, Beatriz Paniagua, Dennis Velakoulis, Eva rndahl, and et al. Hippocampal shape analysis in alzheimers disease and frontotemporal lobar degeneration subtypes. 29:1–11, 2012.
- [56] Fuyun Ling Fuyun Ling, D Manolakis, and J Proakis. A recursive modified gram-schmidt algorithm for least- squares estimation, 1986.
- [57] C Lorenz. Generation of point-based 3d statistical shape models for anatomical objects. *Computer Vision and Image Understanding*, 77(2):175–191, 2000.
- [58] C H Lorenz, E S Walker, V L Morgan, S S Klein, and T P Graham. Normal human right and left ventricular mass, systolic function, and gender differences by cine magnetic resonance imaging. *Journal of cardiovascular magnetic resonance official journal of the Society for Cardiovascular Magnetic Resonance*, 1(1):7–21, 1999.
- [59] S. Makino, T. W. Lee, and H. Sawada. *Blind Speech Separation*. Springer, New York, 1. edition, 2007.
- [60] T Mansi, I Voigt, B Leonardi, X Pennec, S Durrleman, M Sermesant, H Delingette, A M Taylor, Y Boudjemline, G Pongiglione, and et al. A statistical model for quantification and prediction of cardiac remodelling: Application to tetralogy of fallot. *IEEE Transactions on Medical Imaging*, 30(9):1605–1616, 2011.
- [61] Shashwath A Meda, Balaji Narayanan, Jingyu Liu, Nora I Perrone-Bizzozero, Michael C Stevens, Vince D Calhoun, David C Glahn, Li Shen, Shannon L Risacher, Andrew J Saykin, and et al. A large scale multivariate parallel ica method reveals novel

- imaging-genetic relationships for alzheimers disease in the adni cohort. *NeuroImage*, 60(3):1608–21, 2012.
- [62] Dominik Meier and Elizabeth Fisher. Parameter space warping: shape-based correspondence between morphologically different objects. *IEEE Transactions on Medical Imaging*, 21(1):31–47, 2002.
- [63] Michael I Miller. Computational anatomy: shape, growth, and atrophy comparison via diffeomorphisms. *NeuroImage*, 23 Suppl 1(Supplement 1):S19–S33, 2004.
- [64] B C Munsell, P Dalal, and Song Wang Song Wang. Evaluating shape correspondence for statistical shape analysis: a benchmark study. *IEEE Transactions on Pattern Analysis and Machine Intelligence*, 30(11):2023–2039, 2008.
- [65] Sherif F Nagueh, Christopher P Appleton, and Thierry C et al. Gillebert. Recommendations for the evaluation of left ventricular diastolic function by echocardiography. *Journal of the American Society of Echocardiography official publication of the American Society of Echocardiography*, 10(2):1–9, 2009.
- [66] Ganesh R. Naik and Dinesh K. Kumar. An overview of independent component analysis and its applications. *Informatica*, 35:63–81, 2011.
- [67] W G ODell, C C Moore, W C Hunter, E A Zerhouni, and E R McVeigh. Three-dimensional myocardial deformations: calculation with displacement field fitting to tagged mr images. *Radiology*, 195(3):829–835, 1995.
- [68] Dinh Tuan Pham Dinh Tuan Pham and P Garat. Blind separation of mixture of independent sources through a quasi-maximum likelihood approach, 1997.
- [69] S M Pizer, D S Fritsch, P A Yushkevich, V E Johnson, and E L Chaney. Segmentation, registration, and measurement of shape variation via image object shape. *IEEE Transactions on Medical Imaging*, 18(10):851–865, 1999.
- [70] B Planitz, A Maeder, and J Williams. The correspondence framework for 3d surface matching algorithms. *Computer Vision and Image Understanding*, 97(3):347–383, 2005.
- [71] Michael Quicken, C Brechbuhler, Johannes Hug, Hans Blattmann, and G Szekely. Parameterization of closed surfaces for parametric surface description. *Proceedings IEEE Conference on Computer Vision and Pattern Recognition CVPR 2000 Cat NoPR00662*, 1:354–360, 2000.
- [72] J N Reddy. *An Introduction to the Finite Element Method*. McGraw-Hill, 3. edition, 2005.
- [73] S Rich, D R Dantzker, S M Ayres, E H Bergofsky, B H Brundage, K M Detre, A P Fishman, R M Goldring, B M Groves, and S K Koerner. Primary pulmonary hyper-

- tension. a national prospective study. *Annals of Internal Medicine*, 107(2):216–223, 1987.
- [74] M S Sacks, C J Chuong, G H Templeton, and R Peshock. In vivo 3-d reconstruction and geometric characterization of the right ventricular free wall. *Annals of Biomedical Engineering*, 21(3):263–275, 1993.
- [75] Abhirup Sarkar, Roberto J Santiago, Ryan Smith, and Alireza Kassaei. Comparison of manual vs. automated multimodality (ct-mri) image registration for brain tumors. *Medical dosimetry official journal of the American Association of Medical Dosimetrists*, 30(1):20–24, 2005.
- [76] F Schwiep, S S Cassidy, M Ramanathan, and R L Johnson. Rapid in vivo determinations of instantaneous right ventricular pressure and volume in dogs. *American Journal of Physiology*, 254(4 Pt 2):H622–H630, 1988.
- [77] L Shen and F Makedon. Spherical mapping for processing of 3d closed surfaces. *Image and Vision Computing*, 24(7):743–761, 2006.
- [78] Li Shen, Hany Farid, and Mark A McPeck. Modeling three-dimensional morphological structures using spherical harmonics. *Evolution: International Journal of Organic Evolution*, 63(4):1003–1016, 2009.
- [79] Marc A. Simon. Assessment and treatment of right ventricular failure. *Nature Reviews Cardiology*, 2013.
- [80] Marc A Simon, Christopher Deible, Michael A Mathier, Joan Lacomis, Orly Goitein, Sanjeev G Shroff, and Michael R Pinsky. Phenotyping the right ventricle in patients with pulmonary hypertension. *Clinical and translational science*, 2(4):294–299, 2009.
- [81] Grald Simonneau, Ivan M Robbins, Maurice Beghetti, Richard N Channick, Marion Delcroix, Christopher P Denton, C Gregory Elliott, Sean P Gaine, Mark T Gladwin, Zhi-Cheng Jing, and et al. Updated clinical classification of pulmonary hypertension. *Journal of the American College of Cardiology*, 54(1 Suppl):S43–S54, 2009.
- [82] Anuj Srivastava, Shantanu H Joshi, Washington Mio, and Xiuwen Liu. Statistical shape analysis: clustering, learning, and testing. *IEEE Transactions on Pattern Analysis and Machine Intelligence*, 27(4):590–602, 2005.
- [83] Mikkel B Stegmann, David Delgado Gomez, Richard Petersens Plads, and Dk Kgs Lyngby. A brief introduction to statistical shape analysis. *Analysis*, I(March):1–15, 2002.
- [84] M Styner, G Gerig, J Lieberman, D Jones, and D Weinberger. Statistical shape analysis of neuroanatomical structures based on medial models. *Medical Image Analysis*, 7(3):207–220, 2003.

- [85] Martin Styner, Jeffrey A Lieberman, Dimitrios Pantazis, and Guido Gerig. Boundary and medial shape analysis of the hippocampus in schizophrenia. *Medical Image Analysis*, 8(3):197–203, 2004.
- [86] Martin Styner, Ipek Oguz, Shun Xu, Christian Brechbhlér, Dimitrios Pantazis, James J Levitt, Martha E Shenton, and Guido Gerig. Framework for the statistical shape analysis of brain structures using spharm-pdm. *The insight journal*, (1071):242–250, 2006.
- [87] Avan Suinesiaputra, Alejandro F Frangi, Theodorus A M Kaandorp, Hildo J Lamb, Jeroen J Bax, Johan H C Reiber, and Boudewijn P F Lelieveldt. Automated detection of regional wall motion abnormalities based on a statistical model applied to multislice short-axis cardiac mr images. *IEEE Transactions on Medical Imaging*, 28(4):595–607, 2009.
- [88] Dalin Tang, Chun Yang, Tal Geva, and Pedro J Del Nido. Patient-specific mri-based 3d fsi rv/lv/patch models for pulmonary valve replacement surgery and patch optimization. *Journal of Biomechanical Engineering*, 130(4):041010, 2008.
- [89] Paul M. Thompson, Kiralee M. Hayashi, Greig I. de Zubicaray, Andrew L. Janke, Stephen E. Rose, James Semple, Michael S. Hong, David H. Herman, David Gravano, David M. Doddrell, and Arthur W. Toga. Mapping hippocampal and ventricular change in alzheimer disease. *NeuroImage*, 22(4):1754 – 1766, 2004.
- [90] Yalcin Tuncer, Murat M Tanik, and David B Allison. An overview of statistical decomposition techniques applied to complex systems. *Computational statistics data analysis*, 52(5):2292–2310, 2008.
- [91] Mehmet Uzumcu, Alejandro F Frangi, Johan H C Reiber, and Boudewijn P F Lelieveldt. Independent component analysis in statistical shape models. *Proceedings of SPIE*, 5032(1):375–383, 2003.
- [92] Norbert F Voelkel, Robert A Quaife, Leslie A Leinwand, Robyn J Barst, Michael D McGoon, Daniel R Meldrum, Jocelyn Dupuis, Carlin S Long, Lewis J Rubin, Frank W Smart, and et al. Right ventricular function and failure: report of a national heart, lung, and blood institute working group on cellular and molecular mechanisms of right heart failure. *Circulation*, 114(17):1883–1891, 2006.
- [93] F Wiesmann, J Ruff, S Engelhardt, L Hein, C Dienesch, A Leupold, R Illinger, A Frydrychowicz, K H Hiller, E Rommel, and et al. Dobutamine-stress magnetic resonance microimaging in mice : acute changes of cardiac geometry and function in normal and failing murine hearts. *Circulation Research*, 88(6):563–569, 2001.
- [94] Jia Wu, Yingqian Wang, Marc Simon, and John Brigham. A new approach to kinematic feature extraction from the human right ventricle for classification of hypertension: a feasibility study. *Physics in Medicine and Biology*, 40(7):2005–2010, 2012.

- [95] Jia Wu, Yingqian Wang, Marc Simon, and John Brigham. A new approach to kinematic feature extraction from the human right ventricle for classification of hypertension: a feasibility study. *Physics in Medicine and Biology*, 40(7):2005–2010, 2012.
- [96] Jia Wu, Yingqian Wang, Marc Simon, Michael Sacks, and John C. Brigham. A new computational framework for anatomically consistent 3d statistic shape analysis with clinical imaging applications. *Computer Methods in Biomechanics and Biomedical Engineering: Imaging and Visualization*.
- [97] Jia Wu, Yingqian Wang, Marc A. Simon, Sacks Michael S., and John C. Brigham. A new computational framework for anatomically consistent 3d statistic shape analysis with clinical imaging applications. *Computer Methods in Biomechanics and Biomedical Engineering: Imaging and Visualization*, 1(1):13–37, 2013.
- [98] Chun Yang, Dalin Tang, Idith Haber, Tal Geva, and Pedro J Del Nido. In vivo mri-based 3d fsi rv/lv models for human right ventricle and patch design for potential computer-aided surgery optimization. *Computers structures*, 85(11-14):988–997, 2007.
- [99] Can Ye, Miguel Tavares Coimbra, and B V K Vijaya Kumar. Investigation of human identification using two-lead electrocardiogram (ecg) signals. *Fourth IEEE International Conference on Biometrics: Theory, Applications and Systems (BTAS)*, pages 1–8, 2010.
- [100] Peng Yu, P Ellen Grant, Yuan Qi, Xiao Han, Florent Sgonne, Rudolph Pienaar, Evelina Busa, Jenni Pacheco, Nikos Makris, Randy L Buckner, and et al. Cortical surface shape analysis based on spherical wavelets. *IEEE Transactions on Medical Imaging*, 26(4):582–597, 2007.
- [101] Paul A Yushkevich, Hui Zhang, and James C Gee. Continuous medial representation for anatomical structures. *IEEE Transactions on Medical Imaging*, 25(12):1547–1564, 2006.
- [102] D W Zaidel, M M Esiri, and P J Harrison. Size, shape, and orientation of neurons in the left and right hippocampus: investigation of normal asymmetries and alterations in schizophrenia. *The American Journal of Psychiatry*, 154(6):812–818, 1997.
- [103] R Zayer, C Rossl, and H P Seidel. Curvilinear spherical parameterization. *IEEE International Conference on Shape Modeling and Applications 2006 SMI06*, pages 11–11, 2006.
- [104] Honghai Zhang, Andreas Wahle, Ryan K Johnson, Thomas D Scholz, and Milan Sonka. 4-d cardiac mr image analysis: left and right ventricular morphology and function. *IEEE Transactions on Medical Imaging*, 29(2):350–364, 2010.